RESEARCH THESES/REPORTS

THESIS NO. 79-7T

TITLE: Experimental Techniques for Impulse Response Measurement of Optical Glass Fibers

AUTHOR(S) Rainer Paduch

Department of Electrical Engineering
McGill University
Montreal, CANADA

DATE: January 31, 1979

GRANT OR CONTRACT:

NO. OF PAGES: 106

SUPERVISOR: G.L. Yip

Experimental Techniques For Impulse Response Measurement Of Optical Glass Fibres

Submitted By: Rainer Paduch
7111583
January 31, 1979

Supervisor: Dr. G. L. Yip
Dep't of Elect. Eng.
McGill University

This project report is submitted to fulfill the partial requirements for the degree of Master of Engineering (M. Eng.) , Option B.

TABLE OF CONTENTS

Chapter 2: Semiconductor Laser Diodes

Chapter 3: Avalanche Photodetectors

Chapter 4: Ray Theory of Pulse Spreading

ABSTRACT

AM, FM, and PCM-FSK modulation techniques are discussed and an argument for the preference for the PCM technique is presented. The theory of the operation of semiconductor lasers and avalanche photodetectors is presented with the subsequent discussion leading to the use of these devices in fibre optics work and to some of the disadvantages and problems encountered.

The design of very high speed terminal electronics (for fibre optic communication systems) is given for both single heterojunction and double heterojunction semiconductor laser diodes. Impulse response measurements are subsequently performed on a plastic cladded step (PCS), a step index fibre and a graded index fibre. The observed pulse spreading is refined by digital techniques and is related to ray optics theory and compared with the fibre specifications published by the manufacturer.

Conclusions and recommendations for future work in this area is also given.

ACKNOWLEDGEMENTS

I am deeply indebted to Mr. Andrej Puc for his help and experience in the use of semiconductor lasers and his vast knowledge of experimental techniques in fibre optics work.

LIST OF SYMBOLS

$\eta f_M = nf_M$ = noise power

$\beta = b$ = FM modulation index

f_M = baseband bandwidth

d = width of the active layer of the semiconductor laser

T = temperature (^{o}K)

T' = optical transmission loss

1- Comparison of Modulation Techniques

The comparison of the different modulation techniques (AM, FM, and PCM) is a dubious undertaking; afterall, each technique is radically different in its implementation of the modulation and demodulation processes. The criterion used to measure the efficiency and quality of the various modulation processes must be developed independently for each process. The most common measure of the quality of the communication system is the output signal-to-noise ratio. This is an adequate measure, but one which is not normalized against the effects of system bandwidth and input signal-to-noise ratio. As will be seen, the different modulation techniques affect the output SNR to different extents and at different bandwidth 'costs'. A truer measure of the 'cost' of the various modulation techniques will be developed.

The first step in this derivation is to describe the output signal-to-noise ratios (SNR_o) of the AM, FM and PCM communication systems. In the following discussion, no mention will be made of the quality of the electronics employed in the transmission and detection of the signals. In other words, only the channel characteristics will be considered. It will be assumed that the various systems are operating at their respective optimum conditions. The derivations of output SNR are taken from Ref. 1.

The first system under consideration is the amplitude modulation system with square law demodulator:

$$S_o/N_o = \text{output signal-to-noise ratio}$$

$$= \frac{\overline{m^2(t)}}{1+\overline{m^2(t)}} \cdot \frac{(Si/f_M)}{1+\frac{3}{4}(nf_M/Si)(1+\overline{m^2(t)})} \qquad (1)$$

where $\overline{m^2(t)}$ = time average of the square of the modulating waveform,

S_i = input signal power,

nf_M = baseband noise power measured at the input,

S_i/nf_M = input signal-to-noise ratio,

The bandwidth of this system is just f_M, the baseband bandwidth. Now assuming a sinusoid modulating signal of maximum modulation depth (i.e. $m^2(t) = 1$), the maximum output signal-to-noise ratio (SNR_o) becomes:

$$(SNR_o)_{AM} = \frac{(S_i/nf_M)^2}{3/8 + (S_i/nf_M)3} \qquad (2)$$

The second system to be considered is the FM system. Surprisingly, the SNR_o is independent of the form of the signal:

$$(SNR_o)_{FM} = \frac{(3b^2/2)(S_i/nf_M)}{1 + 3.83(S_i/nf_M)\exp\left(\dfrac{-(S_i/nf_M)}{2(b+1)}\right)} \qquad (3)$$

where $b = \dfrac{\Delta f}{f_M} = \dfrac{\text{change in carrier frequency}}{\text{baseband bandwidth}}$

= modulation index

The modulation bandwidth is given by Carson's Rule as:

$$BW = 2(b + 1)f_M \qquad (4)$$

The third system under consideration is the pulse code modulation system via frequency shift keying (PCM-FSK). The characteristic of this system and that of a digital pulse amplitude modulated system are similar:

$$(SNR_o)_{PCM} = \frac{2^{2N}}{1 + 4P_e\, 2^{2N}} \qquad (5)$$

where N = number of bits used to quantize the signal,

P_e = probability of error in detecting a bit.

For the FSK system, the probability of error is statistically dependent upon the thermal-noise power spectral density and upon the signal energy of a bit. Hence:

$$(P_e)_{FSK} = \tfrac{1}{2}\mathrm{erfc}(0.3S_i/Nnf_M)^{\frac{1}{2}}, \qquad (6)$$

where erfc(x) is the complementary error function. Note that this system is also independent of the form of the modulating signal. The minimum bandwidth is determined by the number of quantization levels (i.e. number of bits) and by the Nyquist criterion for signal sampling:

$$BW = (2f_M)\ N \qquad (7)$$

Fig 1 depicts the characteristic SNR curves of the three systems under consideration. Note that the AM system is the poorest performer of the three. At low input SNR (ie. very noisy channels) , the output SNR is lower than the input SNR. This means that the demodulation process adds more noise to the signal, since at these SNR levels it is difficult to

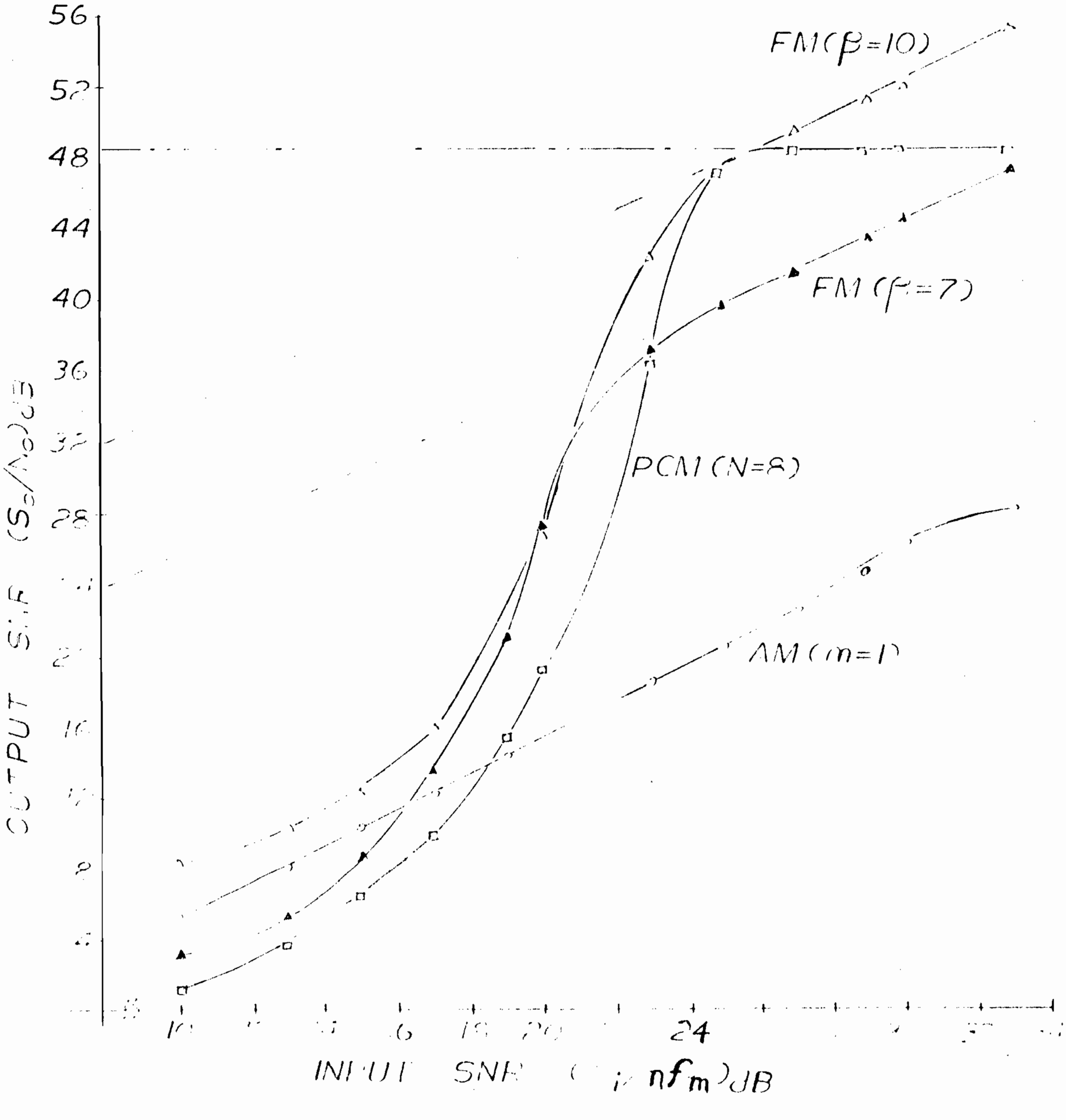

Fig. 1 SNR characteristics of the AM, FM and PCM-FSK communication systems.

distinguish between the noise and the signal. At higher input SNR, both the FM and the PCM systems exhibit a threshold effect. The threshold for the FM system at b=7 and b=10 is 19.5 and 20.8 respectively. The threshold for the PCM system occurs at about 23dB.

For the PCM system, notice that after threshold is acheived, the output SNR remains constant. This is to be expected since an analog signal has been quantized and hence the best reproduction is limited to the number of bits representing the quantization process. This can be seen from Equation 5. When the probability of error (P_e) is very small, then $SNR_o = 2^{2N}$ or $(SNR_o)_{dB} = 6N$. As can be seen, as the number of quantization levels increases (and hence the number of bits needed to represent them), then a more faithful representation of the signal results. This produces a better output SNR. Below threshold, the PCM signal is thermal noise limited.

In comparing the FM and PCM systems, it can be seen that an FM system with a modulation index, b, of 10 has characteristics similar to that of the PCM system. But is this really true? If one compares the bandwidths necessary to acheive this type of performance, one has from Equation 4 a bandwidth of $2(10 + 1)f_M = 22f_M$ for FM and from Equation 7, a bandwidth of $(2f_M)8 = 16f_M$ for an 8 bit PCM system, but note that the FM system has a better output characteristic in the input SNR range of 23 to 33 dB.

From the above discussion, it can be seen that merely using the output SNR as a measure of performance of a communication system is not sufficient. The important considerations are the improvement in signal-to-noise ratio from input to output (ie SNR_o/SNR_i) and the amount of bandwidth required to achieve this improvement. Hence, a better measure of system performance should be the following figure of merit, 'γ', which measures the 'cost of performance' in terms of signal improvement and bandwidth:

$$\frac{1}{\gamma} = \frac{SNR_i}{SNR_o} BW \tag{8}$$

Fig 2 shows the resulting performance costs of the various systems. Notice that for an input SNR of 25 dB, the PCM system is by far the superior system. For equal bandwidths, the PCM system is 11.3/1.7 = 6.7 times more economical than the FM system with $b = 7$. This improvement manifests itself in the better output SNR response. Note, however, that this advantage is only over a limited range of input SNR. The PCM system also has an advantage over the FM system with $b = 10$, but the 'advantage' range is less than for the previous case.

Although the PCM system has an advantage only over a limited range, what is important to note is that its best performance occurs at the lower limit of this range. Hence, at about 25 dB input SNR, the PCM system yields the best overall performance. This implies that repeater spacing should be such that the input SNR does not fall below 25 dB.

In the previous discussion, no mention has been made of the types of electronics involved nor of the types of channels employed. The modulation techniques that were considered are all possible to implement in fibre optic communication systems. It should be noted that AM and FM systems employ linear modulation of the carrier, whereas PCM in a digital system will only involve two levels of light intensity. Fig. 7 depicts the laser light output response curve. This curve, although diode-like in manner, is not absolutely linear. This non-linearity will introduce additional distortion into a linear modulation system. This distortion may be removed from the receiving end by a suitable gain-controlled amplifier or at the transmitter end through the use of an optical feedback system, but this adds to the complexity of the electronics.

The PCM system, fortunately, doesn't have to take into consideration any of the system non-linearities. Pulse modulation of the laser is easily accomplished—a TTL gate connected to the laser biasing circuitry is sufficient. Pulse code modulation via frequency shift keying of a carrier on the laser beam and pulse code modulation via amplitude modulation of the laser beam have similiar SNR characteristics. The latter technique, however, has simpler electronics at both the receiver and transmitter and, hence, is preferable.

The receiver electronics are simpler for PCM than for AM or FM, since the pulses can be directly detected and used. The linear modulation schemes, on the other hand, require demodulation of the signal from the carrier. Other advantages of the PCM technique include error correcting codes. This consequently reduces the probability of error and hence shifts the characteristic curve to the left in Fig. 1. This implies that the system can operate at lower input SNR values and repeater stations can be moved farther apart.

To summarize, the PCM system will provide the best performance per bandwidth than any of the other two systems at low input SNR (25dB). Due to the non-linear characteristic of the laser light output, linear modulation schemes would require correcting circuitry at the receiver. The PCM system requires only detection but no demodulation. Hence, the PCM system via direct modulation of the laser beam provides the best

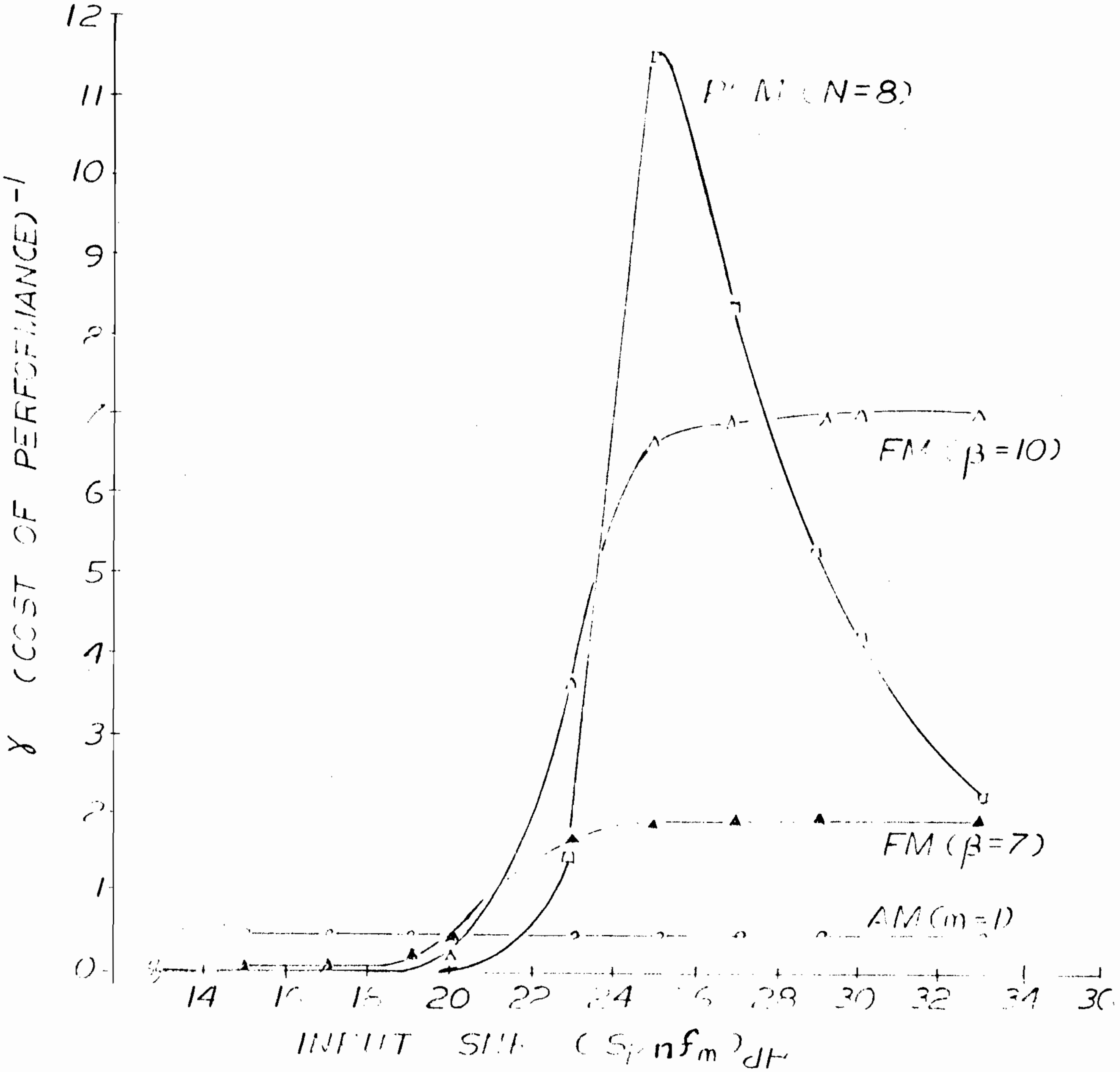

Fig 2. Inverse 'Cost of Performance' curves.

overall performance and is therefore the preferred modulation technique.

The next problem to consider is that of maximum information rate. The problem arises because of finite response times of the charge carriers in the laser and photodetector and also due to the differing group velocities of waves in the glass fibre. As will be shown, the glass fibre has the greatest effect upon the information rate and hence pulse spreading (or impulse response) characteristics are an important fibre parameter.

2- Semiconductor Lasers

(i) Theory of Laser Operation

To gain an understanding of the uses and limitations of the semiconductor laser diode, it is necessary to comprehend the basic principle of operation of this solid state device. Fig 3 shows the typical laser structure: a diode with highly doped 'p' and 'n' regions and the resulting active region formed at the junction. Faces A and B are polished or cleaved to provide high reflection surfaces which are paramount to laser operation. Faces C are roughened to reduce side reflections. A large current flowing into the diode causes massive electron-hole recombination with the resulting stimulated emission of light from the active region.

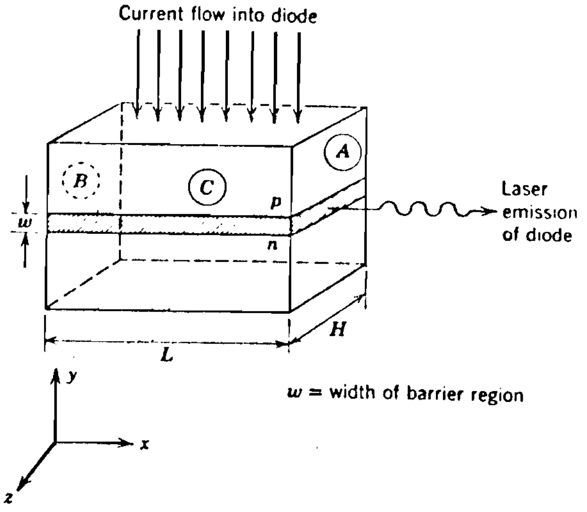

Figure 3 Diagram of laser diode showing direction of current flow and emitted in a typical structure. Faces C would be roughened to discourage side reflections faces (A and B) would be cleaved or polished. (REF 5)

The physical process leading to light emission is depicted in Fig 4. Here, the energy diagram of the heavily doped diode under forward bias shows that in the active region 'w', there are filled states in the conduction band directly above empty states in the valence band. As can be seen, a population inversion has been created. At this point, electron-hole recombination occurs spontaneously with the emission of photons of wavelength $\nu = E_g /h$; E_g is the bandgap energy of the particular material involved.

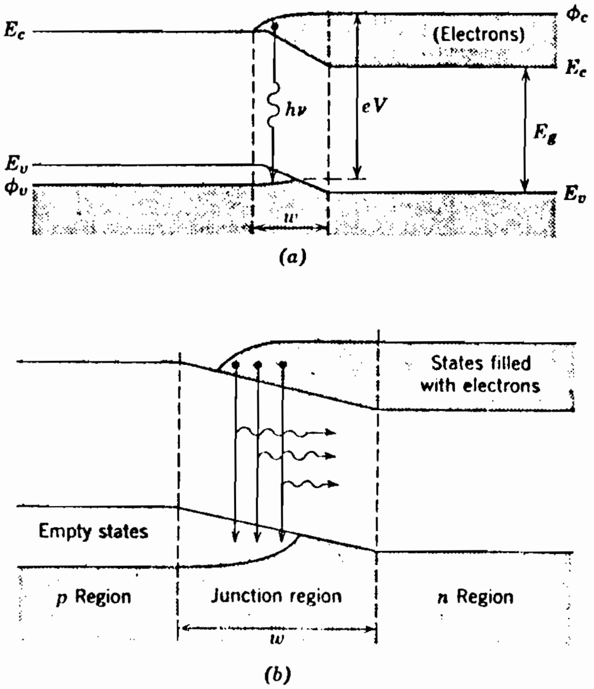

(a)

(b)

Figure 4 Band structure detail in junction region of heavily doped material suitable for laser diodes. (a) Forward biased p-n junction with recombination occurring in junction region; (b) detail of electron density in junction region. (REF 3)

The lifetime for spontaneous pair recombination is between 10^{-8} 10^{-9} seconds. A typical laser diode sample (Fig 4) is about 0.03 cm long, which implies that a photon takes approximately 10^{-12} seconds to traverse this sample. Hence, with highly reflecting surfaces, an emitted photon will bounce back and forth many times stimulating massive electron-hole recombination. As can be seen, a high, monochromatic photon flux is quickly built up. This is the stimulated emission of radiation condition typical of laser operation.

By using surfaces which are partially transmitting, some useful monochromatic light can be obtained from the laser diode. The amount of light outputted can be shown to be dependent upon the driving current. As depicted in Fig 6, the emission spectra below threshold is very wide, which is typical of LEDs (i.e. spontaneous emission). As the current level rises above threshold, laser action sets in.

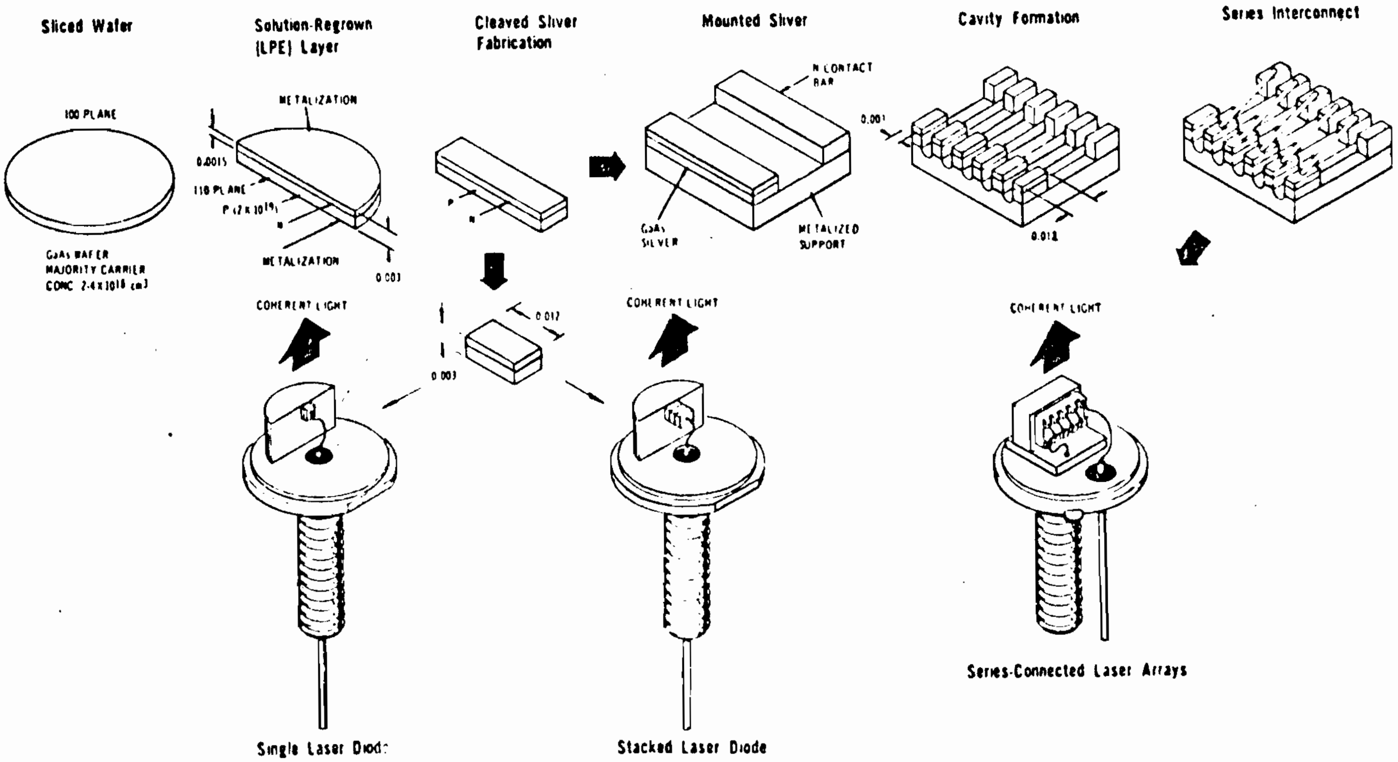

Fig. 5 Fabrication steps in the assembly of laser diodes. All dimensions are in inches (Courtesy RCA Solid State Division). (REF 5)

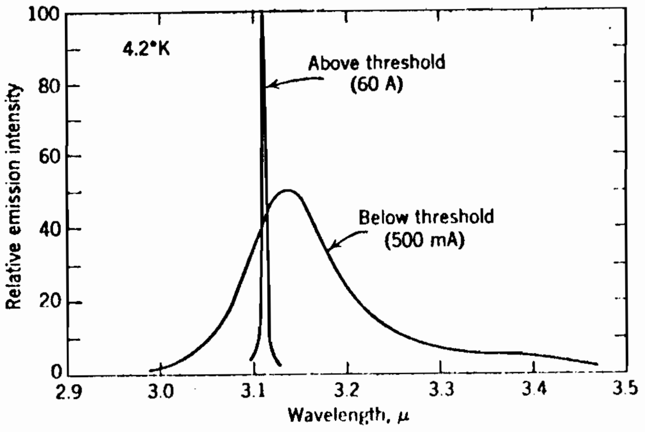

Figure 6 Emission spectra from an InAs diode with cleaved surfaces. The broad spontaneous spectrum line is not to the same intensity scale as the laser line above threshold. Notice that the peak of the emission shifts with current. The diode was at 4.2 K. After R. H. Rediker, *Phys. Today* (1965). REF 3)

(ii) Threshold Effect and the Evolution Of Junctions

As indicated in the discussion above, there exits a threshold effect for coherent light output. In other/words, a certain current level must be exceeded before laser action sets in. Fig 7 depicts this behaviour. Note that the light output versus input current has a typical diode-like characteristic.

From a purely heuristic derivation, one would expect the threshold to be dependent upon the losses encountered in the junction and loss through the cleaved ends. The expression for the threshold current density derived in the references clearly indicates the supposition:(REF 5)

$$J_{th} = 6.3x10^4 \ (\mu^2 d/\epsilon) \ E_g^2 \Delta E_g \ (\alpha_0 + \alpha_D + T'/L) \qquad (9)$$

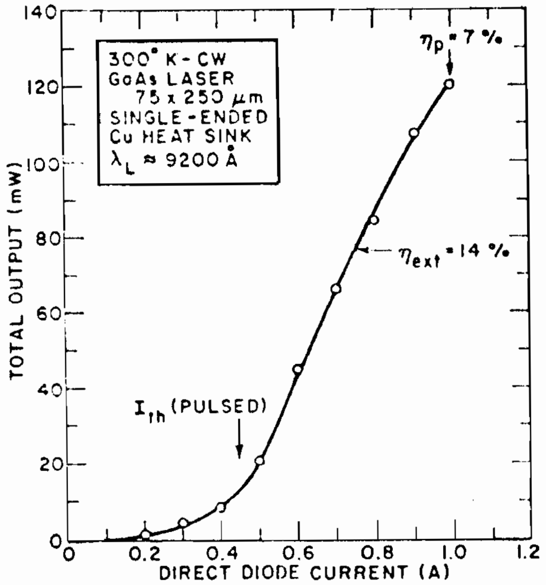

Fig. 7 CW power output as a function direct current for a GaAs laser at 300 K. The device is mounted on a Cu heat sink. The power conversion efficiency η_p 7 % and the differential quantum efficiency η_{ext} 14 % (Kressel and Hawrylo 1970b). (REF 5)

where d = width of the active region

α_0= absorbtion in the 'p' and 'n' regions on either side of the actual junction region

α_D= diffraction losses at the aperture of the emitting region

T'/L = transmission loss/unit length at face A or B (Fig 3)

E_g = bandgap energy of the particular semiconductor material

ΔE_g = $h\Delta\nu$, where $\Delta\nu$= spontantaneous linewidth caused by the uncertainty in the actual energy level of the valence and conduction.

Farther consideration of Equation 9 shows that the threshold current density is temperature dependent:

i.e. $J_{th} \propto T^3$ (Fig 8) (10)

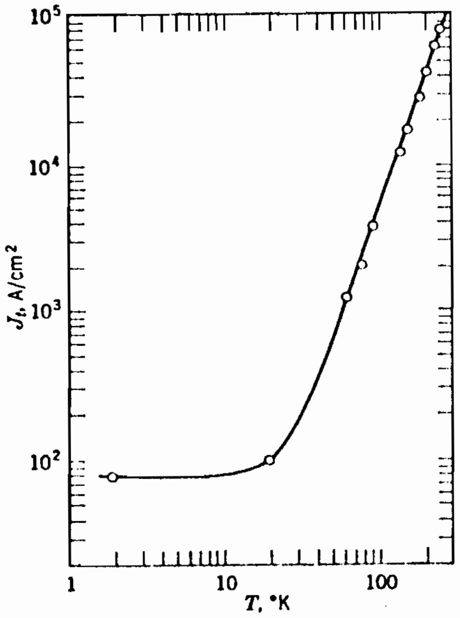

Figure 8 Threshold current for stimulated emission as a function of temperature for a gallium arsenide laser diode. After Burns et al., *Proc. IEEE* (1963). (REF 5)

This effect precluded room temperature operation of the device due to the extremely large currents that were required and the consequent catastrophic heating of the junction.

As can be seen from Equation 9, in order to build devices capable of operating at elevated temperature, a means must be found for reducing J_{th}. To a certain extent this can be accomplished by reducing the losses (i.e. finding better materials) or by reducing the bandgap energy. The recent major advances have been directed at reducing 'w', the width of the active region.

One of the early types of diode lasers was the Homojunction laser. Fig 9 depicts various structures with their accompanying energy and refractive index diagrams. For Homojunctions (Fig 9a), the hole concentration in the p^+ region is typically 1-3x10^{19}cm^{-3} and the electron concentration in the n-type region is 2-4x10^{18} cm^{-3}. The p region results from the diffusion across the p^+n junction and is typically 2 microns wide. Due to the doping variations, the refractive index is somewhat higher in the middle p-type region than in the surrounding p^+ and n regions.

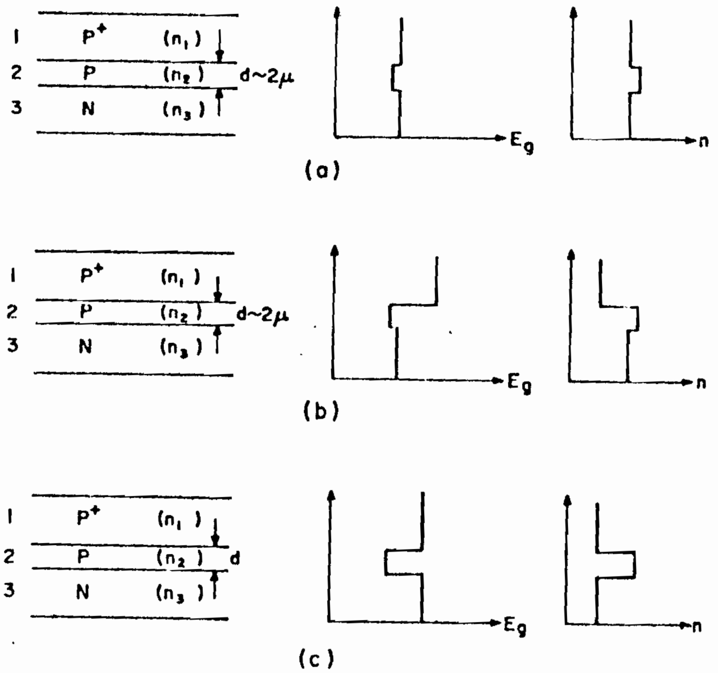

Fig. 9 Schematic diagrams showing the variation of the bandgap energy and of the refractive index at the lasing photon energy in the direction perpendicular to the junction plane in (a) epitaxial homojunction laser, (b) single heterojunction (SH-CC) and (c) double heterojunction (DH) laser. (REF 5)

A major innovation was the fabrication of the single heterojunction 'close-confined' (SH-CC) laser. Here the bandgap energy of the (AlGa)As p^+ region (Fig 9b) is higher than than of the n region. This results in superior efficiency at room temperature. The p^+p heterojunction improves optical confinement to the active region because of increased refractive index discontinuity. Also, since the thickness 'd' of the active region is sufficiently small compared to the diffusion length, the electron recombination volume is reduced. These two factors increase the gain of the laser. Another major advantage is that the absorbtion co-efficient 'α_0', is reduced since the spread of the optical field into the lossy p^+ region is essentially eliminated. These factors all result in a lower threshold current density, J_{th}.

With the success of the increased refractive index at the p^+p region interface, work began on improving the pn side. The result of this work was the double heterojunction (DH) laser (Fig 9c). The addition of a second (AlGa)As-GaAs heterojunction at the pn interface increases the refractive index discontinuity which enables the construction of a narrower active region without loss of optical confinement. The addition of this second heterojunction further reduces J_{th}.

Fig 10 gives the representative curves of the three different laser structures. From these curves, the various room temperature threshold currents can be calculated. Using a typical chip width of 76 microns (ie from Fig 5) one arrives at:

Homojunction: $I_{th} = 13.7$A
SH-CC: $I_{th} = 2.5$A
DH: $I_{th} = 1.3$A

Recent advances have further improved the active region interfaces, and consequently the newest RCA devices (C30130) have threshold currents of about 200 mA.

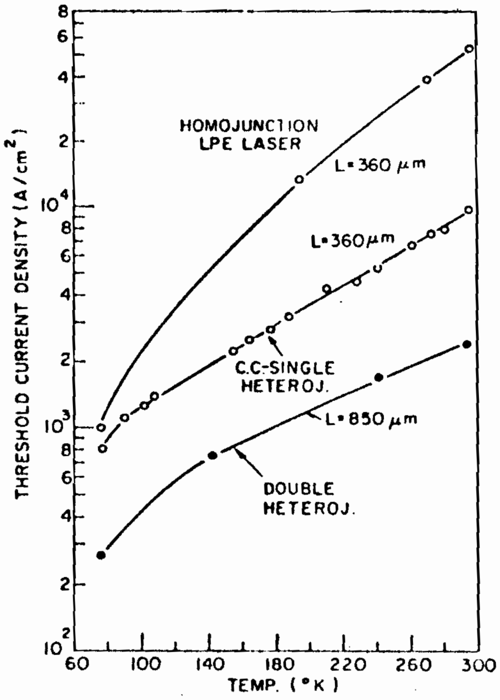

Fig. 10 Representative curves of J_{th} as a function of temperature for homojuction LPE, single-heterojunction and double heterojunction lasers. Properly designed SH-CC and DH lasers are capable of laser operation up to 400 K and sometimes higher depending on the fabrication process. However, the J_{th} of SH CC lasers near the 'cut-off' d value may be very temperature sensitive above 350 K.
(REF 5)

(iii) Power Output and Efficiency

Due to the high threshold current levels, the earlier devices were operated in pulsed mode at room temperature. In order to keep from overheating the laser diodes, duty cycles were less than 10^{-3}. At these repetition rates it was possible to acheive output powers of up to 100 watts from a single diode. By stacking chips, extremely high power light output was produced (Fig 5). Power conversion of up to 10% has been acheived at room temperature with the SH-CC laser in pulsed mode.

In order to acheive continuous (cw) operation, thermal heating must be reduced. Although good heatsinking is a major consideration, low threshold currents are paramount to acheiving reliable cw operation at room temperature. The innovation of the double heterojunction has made possible the production of laser diodes with cw light outputs of up to a few hundred milliwatts with very high duty cycles and repetition rates in excess of 100 MHz (Fig 7). Power conversion is in the order of 7% at room temperature. Improvements in materials and fabrication will undoubtedly provide devices with higher light output and better conversion efficiency.

Fig 11 shows the far field emission pattern of an SH-CC laser. The angular spread of this device is about 15° at its half-power point. The DH laser has an angular spread of about 40°. Improvements in construction have reduced this spread somewhat (about 30° for the new RCA C30130). It has been suggested that 'off-axis' modes and uncoupled emission from the various regions in the junction plane are the cause of this divergence.

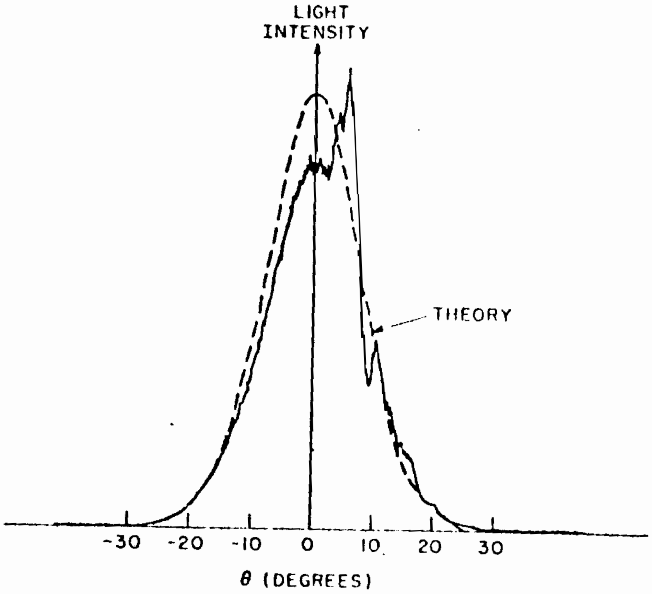

Fig. 11 Far-field emission pattern in the plane perpendicular to the junction of a SH-CC laser with $d = 2.5\ \mu m$ operating in the fundamental transverse mode (Byer and Butler 1970). (REF 5)

(iv) Gigabit/Sec Laser Operation

Danielsen (Ref 8) indicates that there are three basic problems encountered when operating a laser at high bit rates:

(i) a time delay between the applied current pulse and the resulting light pulse,

(ii) ringing transients, and

(iii) the charge-storage effect of preceding pulses on the light pulse form and magnitude.

Danielsen goes on to show that a DC-bias current near threshold reduces the delay. Also, the first spike of the ringings is suggested to be utilized as a light pulse. This is accomplished by switching off the current pulse immediately after the light pulse appears. The influence of the charge-storage effect can be overcome by making the electron and photon density start conditions the same for each pulse. From numerical solutions to the rate equations (Equations 11 & 12), it turns out that the exact current pulse form is not significant. Only the charge delivered by the current must fulfill some requirements:

$$dn/dt = J/(ew) - n/T_s - gS \qquad (11)$$

$$dS/dt = gS - S/T_p + bn/T_s \qquad (12)$$

where n,J,S are the electron, current and photon densities respectively,

w is the active layer thickness,

e is the electronic charge,

T_s, T_p are the electron and photon lifetimes,

g is the laser gain = $\alpha(n-N_0)$

N_o, α are constants,

b is the fraction of spontaneous light that goes into the lasing mode, which is proportional to the number of modes.

Numerical solutions are given in Fig 12 for square and raised cosine current pulses under differing starting conditions. As can be seen, for a large number of modes and a higher initial photon density, the output light pulse will be shorter and wider. The areas under the curves, however, are the same (ie both situations transmit the same amount of energy).

The conclusions drawn by Danielsen indicate that correctly timed and undertimed current pulses with pulse spacings down to 100 psec will give no or small intersymbol interference. Overtimed current pulses will give instability and strong intersymbol interference. It is advantageous to have the prebias a little above threshold since then dynamic behaviour is improved and the resultant spectrum is narrow. Consequently, Danielsen's theoritical model indicates that bit rates of 3-4 Gigabit/sec are possible.

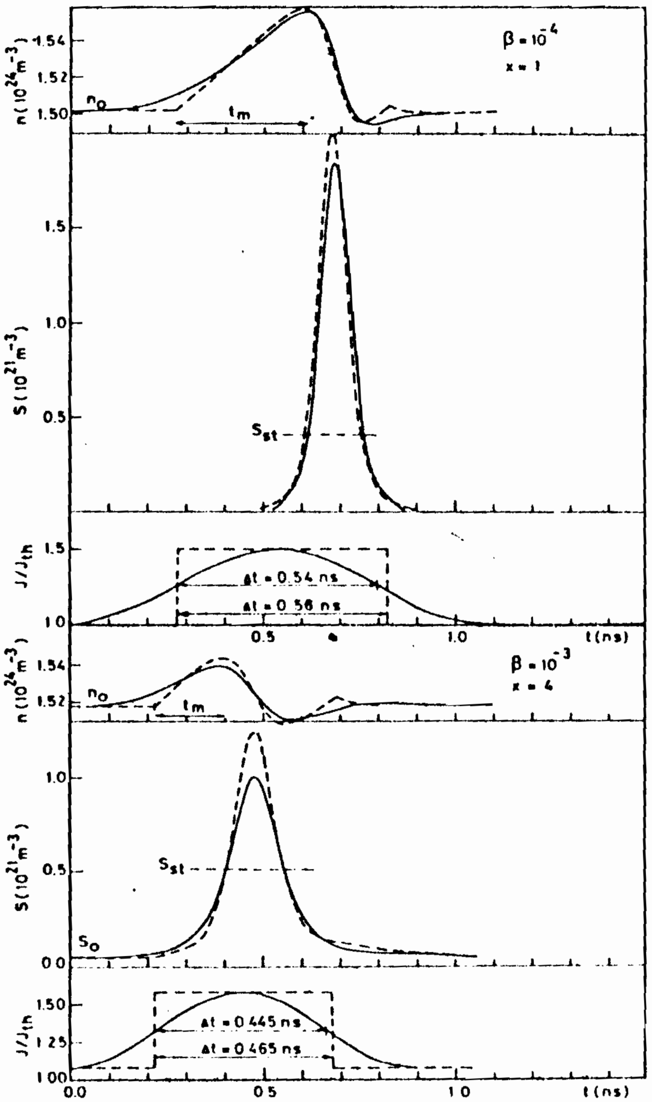

Fig. 12 Numerical results of electron and photon densities as a functio of time in a pulse, calculated for a raised cosine (—) and a squa (---) current pulse. The applied parameters were $\tau_p = 2.94/(1$ $2.67 \cdot 10^{-25}$ $n(t))$ ps, $\tau_s = 4.0$ ns, $\alpha = 1.125 \cdot 10^{-12}\ s^{-1} \cdot m^3$, N_0 $0.11 \cdot 10^{25}\ m^{-3}$, $d = 0.5\ \mu m$, $e = 1.6 \cdot 10^{19}$ As. (REF 8)

(v) Reliability

From the fabrication and testing of various semiconductor lasers, two basic modes of failure have been observed: catastrophic failure which is dependent only upon the optical light flux; and gradual degradation due to current density, duty cycle and details of the laser fabrication process.

Catastrophic failure may occur as a result of mechanical damage of tha facet at or near the region of optical emission (Fig 13). The failure point is a function of the optical flux density in the lasing region, pulse length and possibly laser length. The conclusion is that short pulses are preferred since then damage is less likely to occur. Two hypotheses have been put forward to explain the origin of the facet damage. The first maintains that damage occurs because of local melting due to direct absorbtion of the intense optical flux. The second hypothesis contends that failure is due to local fracture at the surface caused by large stresses from conversion of optical energy into acoustical energy via an opto-acoustic non-linear coupling process. The problem of catastrophic failure may be avoided by proper operating procedures and through the use of antireflective SiO films on the laser facet.

Gradual degradation occurs without any exterior evidence of mechanical damage. Permanent reductions in power conversion efficiency and increases in threshold current are observed as a particular device's operation time increases. This degradation occurs with and without stimulated emission and the degradation rate increases with increasing duty cycle. It has also been observed that the lighter the acceptor atoms, the faster the degradation rate will be. It is believed that non-radiating recombination centers are formed within a diffusion length of the p-n junction, which consequently reduces the number of emitted photons. Recent advances have made possible laser diodes with lifetimes in the order of about 10,000 hours. Although this is a vast improvement over earlier devices, much greater lifetimes must be achieved (100,000 hours) before these lasers can be incorporated into the high quality and reliable communications systems available today.

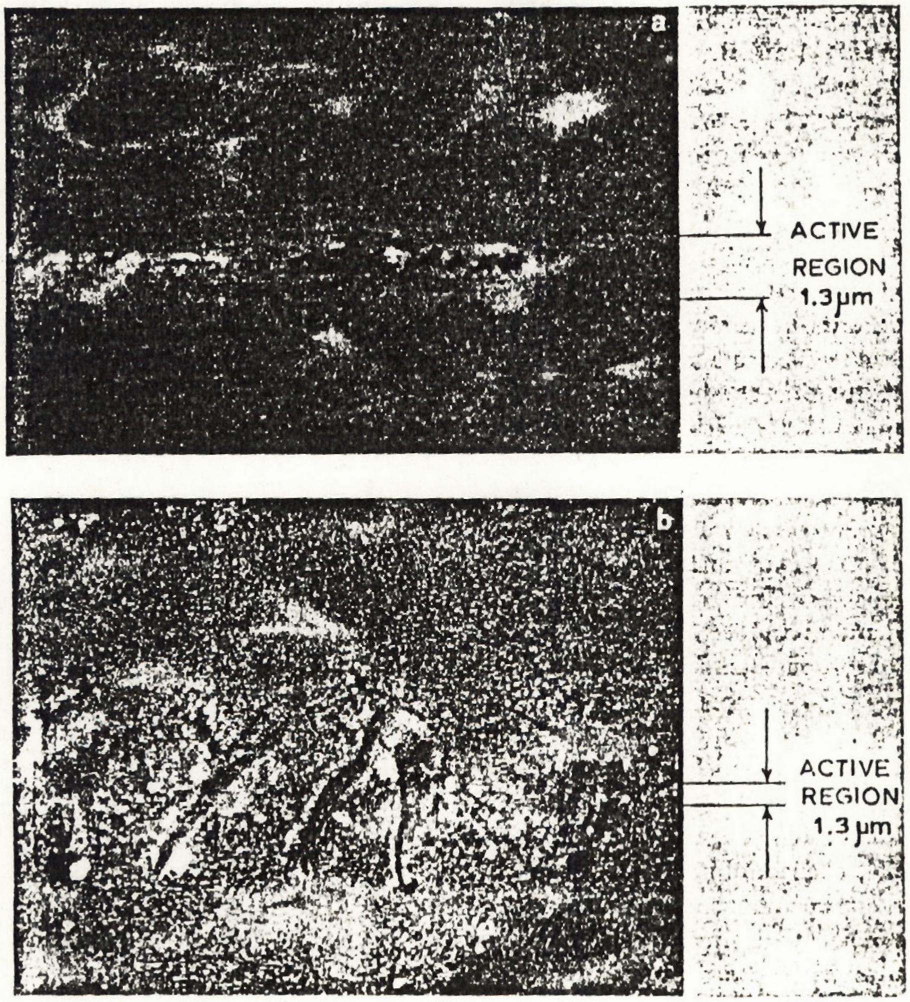

Fig. 13 Scanning electron micrographs of SH-CC laser facets catastrophically damaged at room temperature. The cleaved facet is a (110) plane and the junction lies in the (100) plane. In (a) the damaged region does not extend over the full width of the active (lasing) region; in (b) cracks and fissures are perpendicular to the junction and extend well beyond the active region. In both types of damage there is evidence of local melting in some regions. ([illegible])

3- Avalanche Photodiodes

(i) Theory of Operation

Solid-state photodiodes are the most convenient devices available for the detection of light. They are small, rugged, fast and have almost 100% quantum efficiency. In background limited applications (i.e. light-meters, card readers, light activated relays, etc.) simple p-n or p-i-n photodetectors are ideal since they offer the highest possible signal-to-noise ratio. The drawback of these devices is that they do not provide any internal gain and hence the signal must be amplified to provide a sufficiently large signal current.

In high speed optical communication, however, the limiting source of noise is either the dark current in the detector, the noise in the preamplifier or the quantum noise in the signal carrier. If dark current is the limiting factor, then different materials or cooling of the photodiode must be employed to reduce the dark current. If, however, amplifier noise is the limiting noise source, then an internal gain mechanism in the photodetector is necessary to increase the detector signal and noise above the amplifier noise. This type of requirement is met by avalanche photodiodes.

Under large reverse bias, electrons and holes have ionization rates dependent upon the applied voltage and type of material (Fig. 14). The principle of avalanche multiplication is depicted in Fig 14. The typical avalanche photodiode structure is of the p^+ -i-n^+ type (i= intrinsic layer). Any photon striking the 'p' layer produces an electron-hole pair. The electron migrates to the 'i' layer where, due to impact ionization in the high reverse field region, it produces an electron-hole pair which in turn can produce new pairs as the carriers move across the junction. In Fig 15a it is assumed that the ionization potential of holes is very small so that essentially only the electrons take part in th avalanche phenomenon. As can be seen, the primary injected electron will undergo multiple impact ionizations. Every new electron produced will also be able to produce new electron-hole pairs. At high fields, the elctron-hole pairs grow exponentially with distance until the primary electron reaches the 'n' layer. The short-circuit avalanche response current reaches its maximum within one electron transit time (T_n). The current then decays and approaches zero when the last hole has reached the 'p' layer ($T_n + T_p$). This so called unilateral gain is independent of the excitation frequency up to $f_{3dB} = 2.8/\pi(T_n + T_p)$. Low excess noise and fast response and decay can be expected for carrier multiplication with only one type of ionizing carrier.

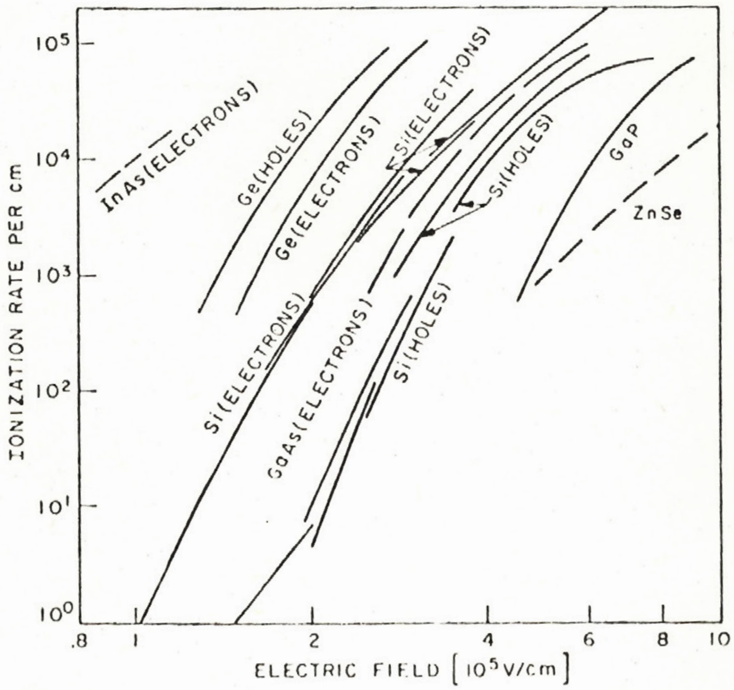

Fig. 14 Ionization (i.e. pair-generation) rates of electrons α and holes β as function of the electric field for various semiconductors. Silicon at 300 K with $\alpha > \beta$ after Miller (1957), Chynoweth (1958), Moll et al. (1963), Lee et al. (1964), Ogawa (1965), Ruegg (1967). Germanium at 300 K with $\beta \approx 2\alpha$ after Miller (1955) and Logan et al. (1965). GaAs at 300 K with $\alpha = \beta$ as assumed by Logan et al. (1962a, 1965), but probably $\alpha \gg \beta$ (Lindley et al. 1969). GaP at 300 K after Logan et al. (1962b, 1965) with the assumption of $\alpha = \beta$. InAs at 100 K with $\alpha \gg \beta$ after Mikhailova et al. (1967). InSb at 77 K shows $\alpha \gg \beta$ with $\alpha \approx 2 \times 10^{-3}$ cm^{-1} at 8×10^3 V/cm (Baertsch 1967). α for ZnSe at 300 K after Williams (1967). (REF [illegible])

In Fig 15b, it is assumed that the ionization rate of electrons and holes are of comparable magnitude. Hence, when the primary electron produces new electron-hole pairs, each secondary electron <u>and</u> hole is capable of generating new pairs. Any new hole near the origin of the primary electron will produce new electrons which must continually traverse the intrinsic layer. This feedback process results in an avalanche of carriers that persist for a long time after the primary electron has left the intrinsic layer. Therefore, in order to have fast response photodetectors capable of operating at high frequencies, it is preferable to have devices with only one carrier having a high ionization rate.

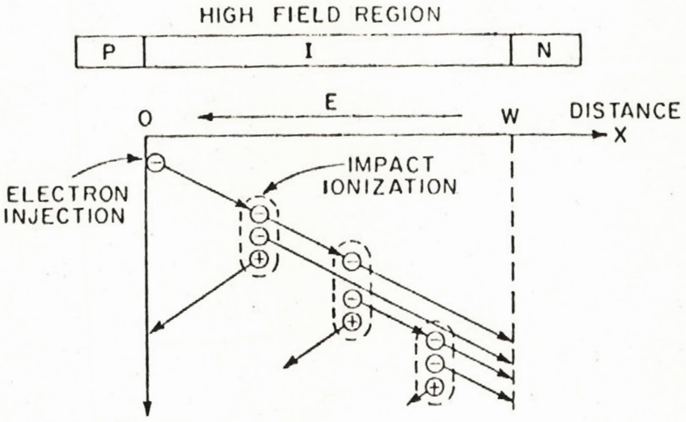

(a) IMPACT IONIZATION THROUGH ELECTRONS ONLY

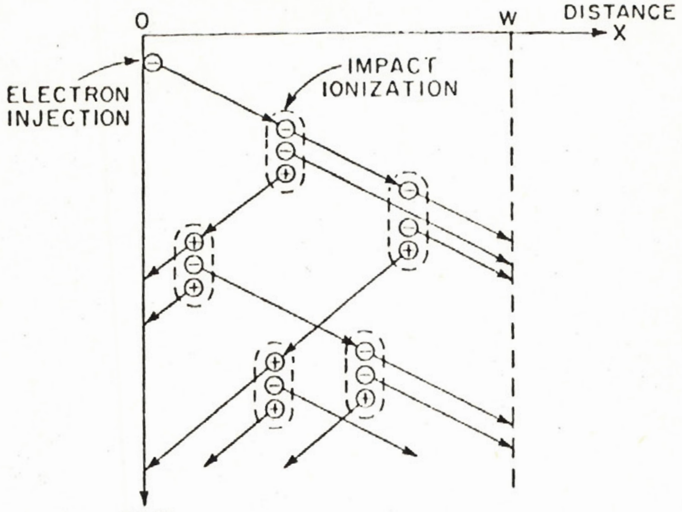

(b) IMPACT IONIZATION THROUGH ELECTRONS AND HOLES

Fig. 15 Schematic view of the avalanche carrier multiplication process in a p-i-n diode with uniform electric field for a) pair-generation by electrons only and b) pair-generation by electrons and holes.
(REF 7)

The voltage-current characteristic of the avalanche photodiode is shown in Fig 16. At low reverse bias voltages, no carrier multiplicatio takes place. Here, normal photodiode operation is observed. Increasing the reverse bias voltage causes carrier multiplication with the resulting increase of the output current. Maximum multiplication is observed when the photodiode is biased to the breakdown voltage 'V_B'. At higher voltages a self-sustained avalanche breakdown current makes the diode less sensitiv to photon-excited carriers. The current gain at V_B is limited by either (a) current-gain bandwidth product (i.e. carrier transit times), or (b) current-induced saturation effects, or (c) spatial inhomogeneities in the multiplication. These gain limitations, as well as the noise fluctuations of the current gain, all depend upon the semiconductor material, on the geometry of the junction and the initiation of electrons and/or holes.

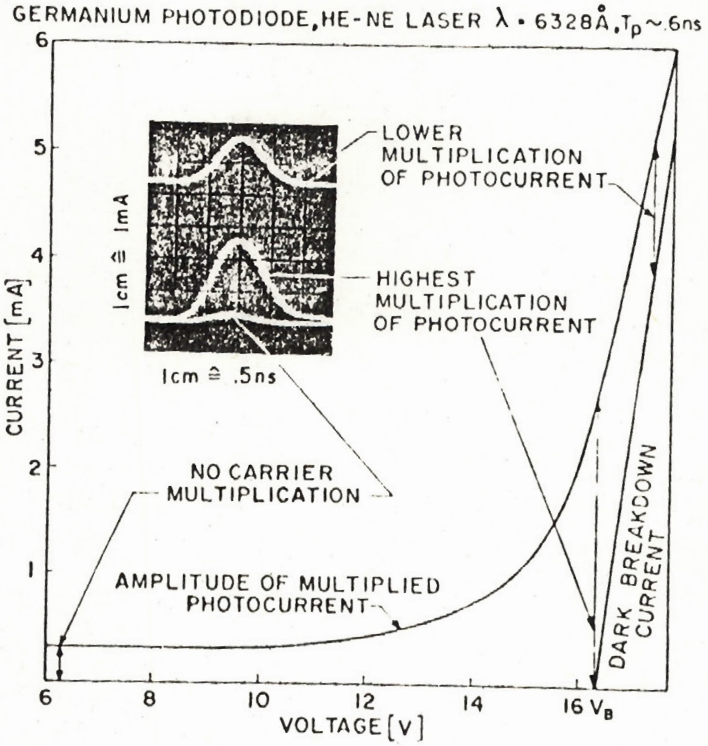

Fig. 16 Current-voltage characteristics and pulse response of germanium avalanche photodiode.
(REF 5)

(ii) Practical Avalanche Photodiode Structures

Fig 17 shows three commercially available silicon avalanche photodiode structures. In Fig 17a is depicted the "bevel-edge" diode with a p^+n junction in which the n-type resistivity is chosen so that V_B is between 1800 to 2600 volts yielding a device with a wide depletion layer. The beveled edges prevent breakdown at the junction periphery. The junction is deep; typically 50 to 75 microns. In silicon, holes do not multiply as readily as the electrons, hence, this device has the advantage of low multiplied dark current. Also shown in Fig 17a is the multiplication function "M" which is dependent upon where the carriers are generated. The only portion of the signal which gets multiplied effectively is that part absorbed in the p-layer. The electric field in this region, however, is small, hence it takes from 10 to 30 nsec for this charge to be collected. Consequently, in the fabrication of this

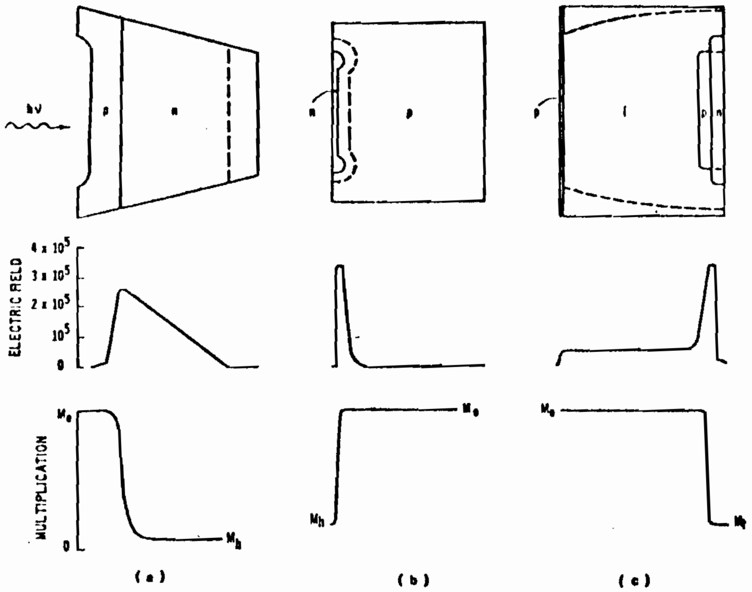

Fig. 17 Structures of three commercially available silicon avalanche photodiodes: (a) beveled edge diode, (b) guard ring structure, and (c) reach-through structure. (REF 12

device, one has to trade-off between fast response and low effective gain at long wavelengths ($\lambda > 0.9$ microns) and slow response and high gain at short wavelengths ($\lambda < 0.9$ microns).

The second device is commonly known as the "guard-ring" structure. This diode is fabricated with an n^+-layer on p substrate or a p^+-layer on n substrate with a variation using a Schottky barrier plus a guard ring instead of a diffused junction. For this device, the junction has a depth of 1 to 2 microns and a depletion layer depth of about 10 to 15 microns. This structure works well for wavelengths in the range of 0.6 to 0.8 microns. For longer wavelengths, much of the light penetrates through to the undepleted region with the result that photogenerated carriers are collected by diffusion and are multiplied. Since these carriers are collected slowly, they do not contribute to the high frequency response of the photodiode. These carriers do, however, contribute to the noise of the diode and consequently the performance of this structure may be quantum-noise limited in many high frequency applications involving penetrating radiation (for this structure it can be as short as 0.8 microns). The typical quantum efficiency of this device is about 30% at 0.9 microns and 1 to 2% at 1.06 micron. Quantum efficiency being defined as that fraction of the incident photon flux that generates electron-hole pairs that are collected by detector contacts.

The third structure (Fig 17c) is the "reach through" diode. This device provides the best combination of high speed, high gain and relatively low noise (This is the most advanced photodiode to date). These features are achieved by separating the depletion layer into two regions: a wide drift region in which the photons are absorbed and a narrow multiplying region in which the photogenerated carriers are multiplied. The avalanche region (right side of diode) is created by the sequential diffusion of p-type (boron) and n-type (phosphorous) materials. The depths of the layers are adjusted so that the depletion layer just "reaches through" to the intrinsic layer when the peak electric field at the junction is 5-10% less than V_B. Any additional increase in applied voltage causes the depletion layer to increase rapidly out to the p^+ contact, even though the field throughout the device increases slowly. The intrinsic layer of the diode can be up to 200 microns wide and can be depleted with the application of less than 100 volts above V_B. This device is only operated in the fully depleted mode so that all carriers are collected by drift alone. Due to their higher ionization rates, electrons are the predominant carriers in silicon and consequently optimum conditions are obtained when the incident radiation is absorbed in the intrinsic region. The fully depleted structure allows the photodiode to be used with radiation entering the p^+ contact. Electrons generated in the intrinsic region are swept to the high field region (right side) where multiplication occurs. The subsequent holes produced in the avalanche region traverse the intrinsic region to the p^+ contact. These carriers constitute the main portion of the multiplied signal. From Fig 17c, it can be seen that avalanche multiplication occurs in the high electric field region around the p-n junction (typically 2 microns wide). Even though the field in the intrinsic layer is relatively low, it is sufficient to produce carrier velocities approaching saturation. This gives rise to electron and hole transit times being dependent upon slice thickness and applied bias. Hence, it can be seen that good gain and high speeds are possible with this diode structure.

Quantum efficiency is an important consideration in the selection of a photodetector. For photodetectors that are not fully depleted, electron-hole pairs may be generated in the undepleted or base layer.

These carriers are collected by diffusion and are consequently responsibl for the tail or long fall times. This effect reduces the high speed pulse response of the detector. For the reach-through avalanche photodetector, the tail is absent since the intrinsic layer is completely depleted. Due to this structure, the quantum efficiency is essentially constant over the full bandwidth (Fig 18).

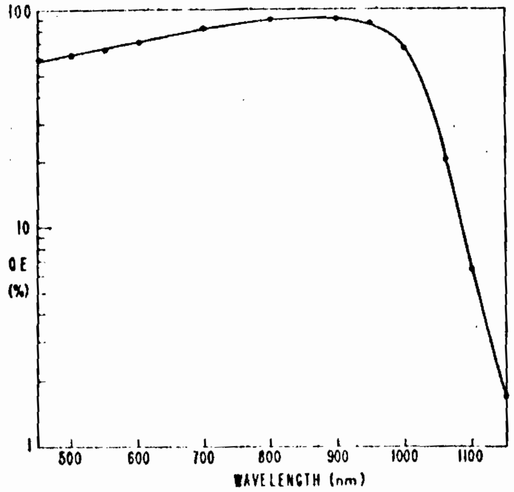

Fig. 18-Quantum efficiency of a typical reach-through avalanche diode (Type C30817) as a function of wavelength. (REF 12)

The transit time of the photogenerated and multiplied carriers across the depletion layer determine the response time of the reach-through avalanche photodiode. These carriers must first be collected in a time equal to or less than an electron transit time $t=w/v_e$ where 'w' is the width of the intrinsic layer and v_e is the average drift velocity in the intrinsic layer. After collection, electron multiplication occurs; the times ranging from 20 psec (high field region transit time) at low gain up to 0.4M psec at high gains (M is the avalanche gain). Hence, the multiplication can be considered to occur almost instantaneously. The holes resulting from the multiplication must then traverse the depletion (or intrinsic) layer back to the p^+ layer. The resultant pulse (for a square pulse input) will depend on where the light is absorbed, however the total pulse duration is less than or equal to the total of the electron and hole transit times (Fig 19).By making the diode thinnner, the response time can be improved (reduced to less than 1 nsec). There is however, a resulting reduction in quantum efficiency as well.

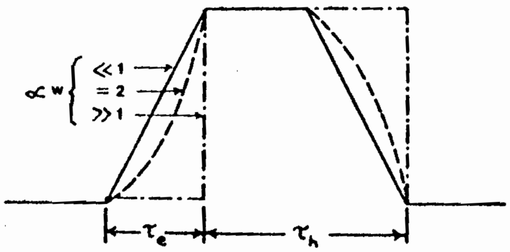

Fig. 19 -Impulse response of reach-through avalanche diodes in which $\tau_h \approx 2\tau_e$. $\alpha w \ll 1$ corresponds approximately to 1.06 μm, $\alpha w = 2$ to 0.9 μm, and $\alpha w \gg 1$ to visible light. (REF 10)

(iii) Noise Characteristics

As has been pointed out before, any photodetector will introduce noise into the signal during detection. Ref 9 derives a total noise equivalent power per unit bandwidth (NEP) as:

$$\mathrm{NEP} = \frac{1}{S}\left\{ 2e\, I_o \frac{m'^2}{m^2} + \frac{4kT}{m^2 R} \right\}^{\frac{1}{2}} = P_o / B^{\frac{1}{2}} \qquad (13)$$

where: S= sensitivity of the detector, which is defined as the photocurrent produced by unit radiation at a specified wavelength (quantum efficiency),

e= electronic charge,

I_o= total detector background current,

T= temperature (°K),

R= load resistor,

m= signal multiplication factor,

m'= noise multiplication factor,

P_o= total noise equivalent power.

From Equation 13 it can be seen that the second term under the square root (the thermal noise produced by the load resistor) has been reduced by the multiplication process. On the other hand, the noise multiplicatio factor, "m'", (which affects the background current) and the signal multiplication factor, "m", (which affects the signal) may increase the noise equivalent power if $m' \geq m$. Fortunately, m' and m are usually of similiar magnitude and hence this difference does not have major consequences.

The thermal noise term is inversely proportional to the load resistor "R". Hence, by using large values for this resistor, the thermal noise can be made negligible. The maximum value of the load resistor, however, is determined by the bandwidth requirement of the system. Therefore a trade-off between noise and bandwidth must be made.

For silicon avalanche photodiodes, the noise multiplication factor can be shown to be: $m' = m^x$, where 'x' depends upon the relative efficiency with which electrons and holes cause impact ionization. For this type of silicon device, $x = 1.15$. This excess noise multiplication is due to both electrons and holes taking part in the multiplication of a steady state signal (including a background illumination signal). With the application of a short, transient signal, only the electrons are collected by the junction. Hence, only these carriers take part in the multiplication process. As can be seen, steady state noise is amplified more than a transient signal. Shot noise amplification in this device is greater than signal amplification, hence, there is a limit to the useful multiplication that can be obtained.

Using some typical avalanche photodiode values discussed in Ref 9:

assume a bulk current of 5×10^{-11} Amp, multiplication factor m = 100 (therefore m' = $100^{1.15}$ = 200) and a sensitivity of 0.6 which results in a total noise equivalent power of:

$$NEP = \frac{1}{0.6}\left(2e\,\frac{200^2}{100^2}\,(5\times10^{-11} + 0.6P) + \frac{4kT}{100^2 R} \right)^{\frac{1}{2}} \qquad (14)$$

At room temperature, this reduces to :

$$NEP = \frac{10^{-13}}{0.6}\,(1.28 + 166/R)^{\frac{1}{2}} \qquad (15)$$

where P is the background noise power.

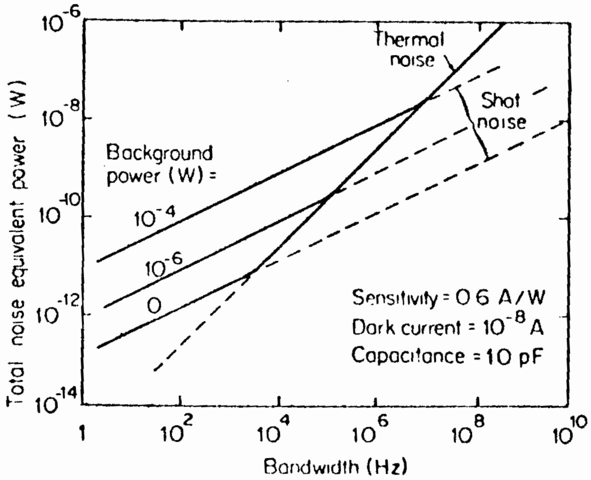

FIGURE 20 The noise performance of a silicon *p–i–n* photodiode (REF 9)

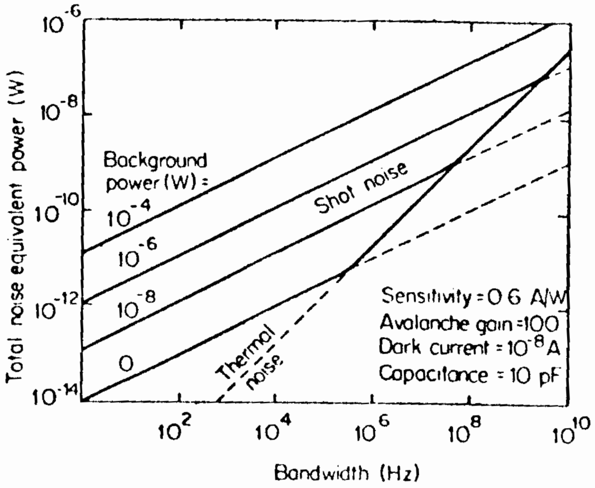

FIGURE 21 The noise performance of a silicon avalanche photodiode (REF 9)

Comparing Fig 20 (photodiode with no internal gain) with that of Fig 21 (avalanche photodiode with the above mentioned characteristics) shows that the multiplication process has reduced the effects of the resistor noise on NEP by a factor of 100, but has increased the effect of shot noise due to background radiation by a factor of two (from Equation

14). The conclusion to be drawn from this discussion is that the use of avalanche multiplication has advantages only in conditions requiring large bandwidths and having low background radiation. At large bandwidths, avalanche photodiodes are thermal noise limited and hence to ensure reliable operation, sufficient optical power must be made available.

(iv) Design Considerations

Fig 22 depicts the complete optical receiver for digital signals where the following circuit elements have been assumed:

$p(t)$=input photon intensity,

$i_s(t)$=avalanche photodiode current generator which represents the production of charges by optical and thermal generation and collision ionization in the diode high-field region,

C_d=diode junction capacitance,

R_b=bias resistor,

$i_b(t)$=bias resistor thermal noise current,

C_A & R_A=shunt capacitance and resistance at the input of an amplifier that is assumed to be a high-gain, infinite-impedance device,

$i_a(t)$ & $e_a(t)$=two noise sources referred to the input-- these noise sources are assumed to be white Gaussian in nature,

$H_{eq}(w)$, $V_{out}(t)$, etc.=equalization and decision circuitry for detecting pulse trains.

In this section, the only concern will be that of detecting and displaying received optical pulses. Hence, the nature of the equalization and decision circuitry will not be considered here. The following simplifications are also made:

$$R_T = (1/R_b + 1/R_A)^{-1} = \text{total detector parallel load resistance,} \tag{16}$$

$$C_T = C_d + C_A = \text{total detector parallel load capacitance.} \tag{17}$$

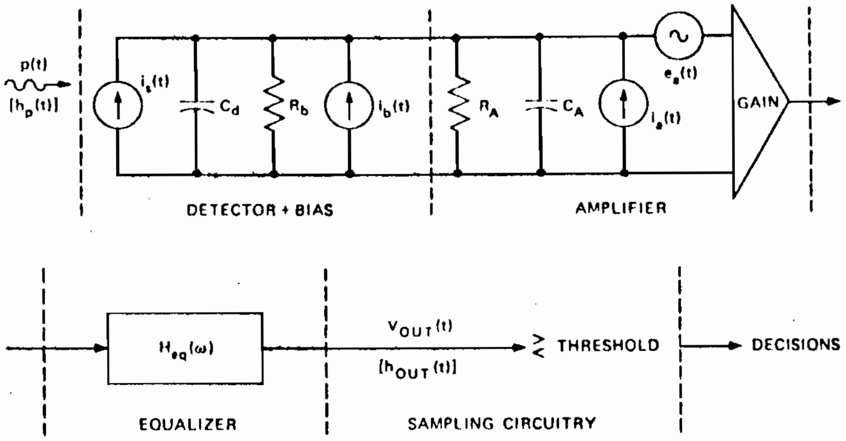

Fig. 22-Receiver. (REF 11)

As has been pointed out in Equation 13, a high value of the biasing resistor, R_b, is required in order to reduce the effect of thermal noise. This is re-iterated by Personick (Ref 11) where he relates the effect of the bias resistor against a 'power penalty'. This power penalty is merely the extra input light power required to overcome the increase in thermal noise caused by a decrease in the diode biasing resistor. This is graphically illustrated in Fig 23, for the case of no diode gain and optimal diode gain. However, as has been pointed out previously, in order to acheive high data rates, the time constant R_TC_T must be kept small. Hence, a trade-off between speed and sensitivity of detection must be made.

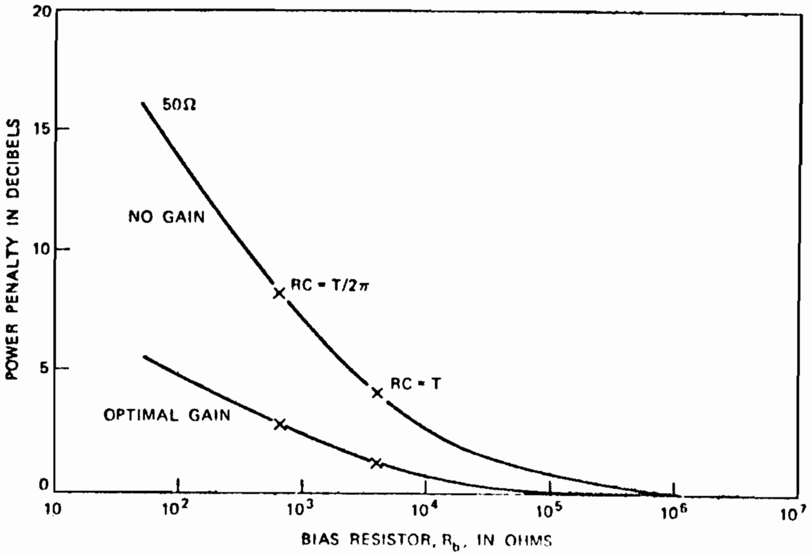

Fig. 23 Required power penalty vs R_b. (REF 11)

Another consideration is the effect of the dark current upon the system performance. A large dark current introduces excessive noise into the detected signal. This effect consequently implies that the light power must be increased to maintain the desired signal-to-noise ratios. This effect is depicted in Fig. 24.

The consequences of the above dicussions indicate that for a wide bandwidth system (as required by systems desiring to measure fibre impulse response), the load resistor must be kept small. Hence, the input optical power must be sufficiently large to provide a reasonabl signal-to-noise ratio.

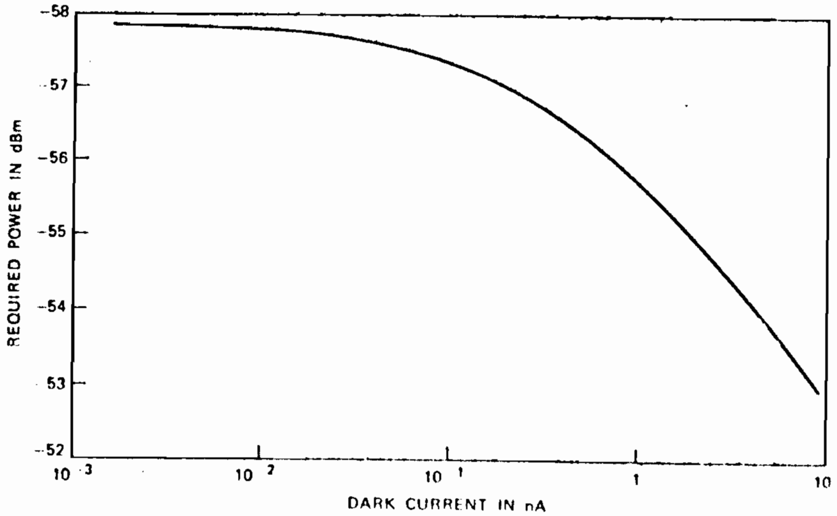

Fig. 24-Required power vs dark current. (REF 11)

4- Ray Optics Theory for Pulse Spreading

(i) Introduction

For optical waveguides, the carrier has a frequency of about 10^{14} Hz. Despite this high frequency, these optical fibres have a limited information capacity which is due to pulse spreading effects. This phenomenon is caused by the following three sources:

(i) pulse broadening due to material dispersion,

(ii) pulse broadening due to intramodal dispersion,

(iii) pulse broadening due to intermodal dispersion (ie. different group velocities for different modes).

The material dispersion is caused by having different group velocities for different wavelengths (ie. chromatic dispersion). Material dispersion is the limiting factor of the information capacity for monomode fibres. Excitation of a monomode fibre with monochromatic sources eliminates this dispersion. It has also been shown by various researchers that this effect can be compensated by a proper choice of refractive index if the operating wavelength is non-optimal. (REF 17)

The intramodal dispersion is also a chromatic dispersion. It appears because the modal structure of a waveguide changes with carrier frequency. Its effect, however, is negligably small compared to the other two dispersions and hence can be ignored.

The intermodal dispersion is the limiting factor for any type of multimode fibre. Since there are many thousands of modes which can exest in the currently available optical fibres, the modal distribution can be considered to be essentially continuous. With this assumption, the analysis of pulse spreading lends itself readily to the ray optics approach developed by Bouillie, Steiner, and Tréheux (Ref 16). The ray optics analysis is desirable to utilize since it is not limited by the very low refractive index change approximation (as is the WKBJ method) and also provides a clearer understanding of the physical processes involved. The basic premise of the ray optics method is that each mode corresponds to a particular ray defined by the angle of incidence. This approximation is, for the purpose of this report, completely adequate and consequently geometric optics becomes a very powerful tool to analyze pulse broadening.

(ii) Step Index Fibres

Fig 25a depicts the ray propagation in a step index fibre. The following analysis is taken from Ref 16. Here the limit angle is defined by Snell's law as:

$$\cos\theta_0 = n_2/n_1 \quad . \tag{16}$$

Consequently, the delay of the axial ray (ie. $\theta = 0$) becomes:

$$T_0 = Ln_1/c \quad , \tag{17}$$

which immediately gives the delay time of the meridional rays as:

$$T = \frac{L}{c} n_1 \frac{1}{\cos\theta} = T_0/\cos\theta \tag{18}$$

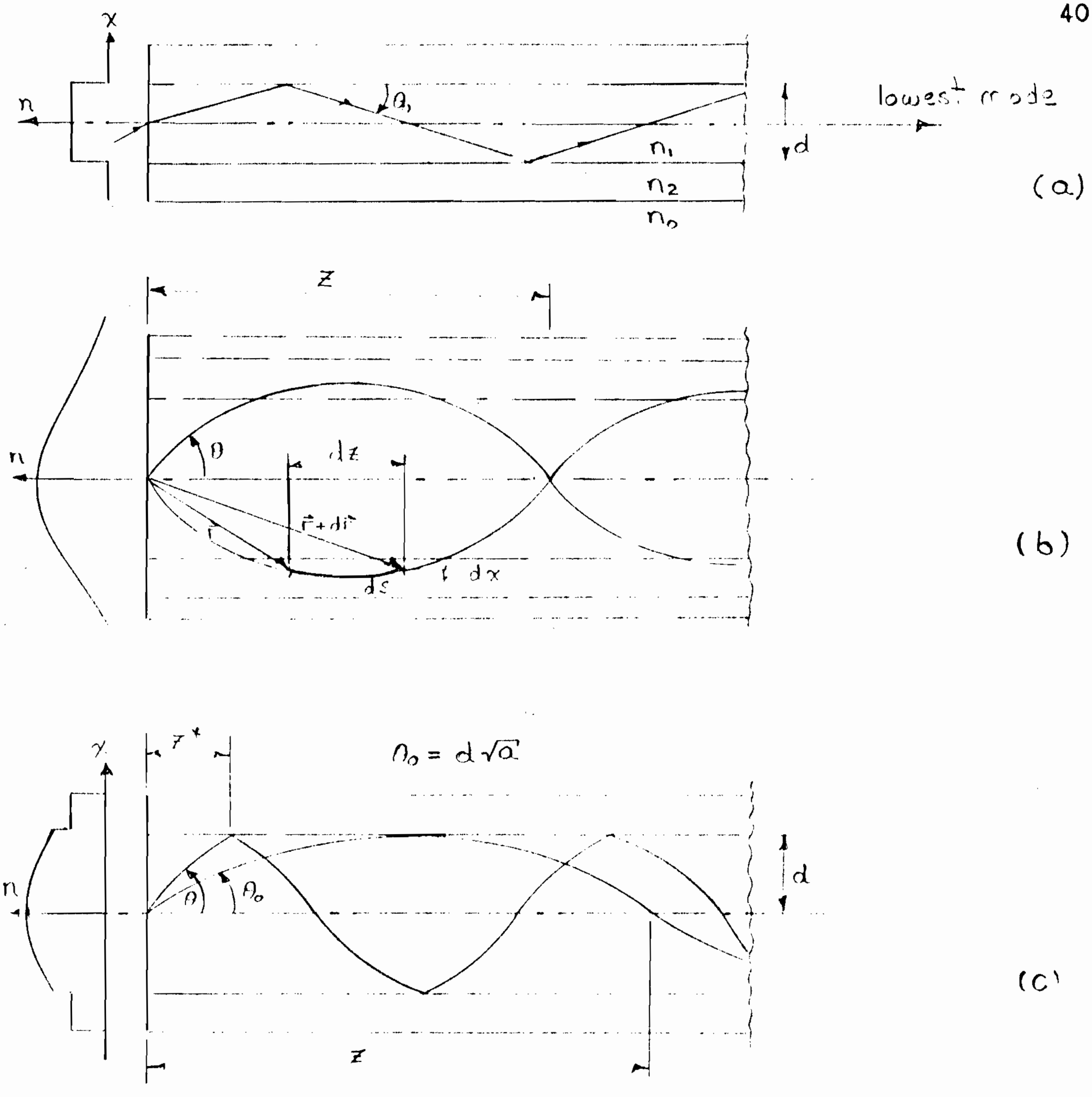

Fig 25. Ray propagation in optical glass fibres;

(a) step index fibre,

(b) ideal graded index fibre,

(c) cladded graded index fibre.

Skew rays can also be excited if the plane of incidence is not meridional. These skew rays usually exceed the critical angle of the total reflection and hence are greatly attenuated. Therefore, skew rays carry very little signal energy and can be ignored in the analysis.

The time delay difference between a general meridional and an axial ray becomes:

$$T = T - T_o = T_o(1/\cos\theta - 1) \; ; \qquad (19)$$

and the number of reflections of the meridional ray is:

$$p = (L/d) \tan\theta \; . \qquad (20)$$

Other terms which require definition are:

$$A(\theta) = \exp(-aL/\cos\theta) \qquad (21)$$

= ray damping by substance losses;

$$B(\theta) = (1 - b)^p \qquad (22)$$

= ray damping by interface losses
(imperfect reflections);

where 'a' and 'b' are phenomenological mean values which may be angle dependent. Consequently, the total energy available at the output of the guide of length 'L' is:

$$\text{Energy} = \frac{E_o}{K_E} \int_{-\infty}^{\infty} F(t, \theta_o) \, dt \; . \qquad (23)$$

where:

$$F(t,\theta_o) = \frac{1}{K(\theta_o)} \int_{\theta}^{\theta_o} f(t-T)h(\theta)A(\theta)B(0)\sin\theta d\theta \qquad (24)$$

$f(t)$ = time function of input pulse,

$H(\theta)$ = energy distribution (angle dependent),

A,B = angle dependent fibre losses,

$K_E, K(\theta_o)$ = normalizations.

Consider first the situation where there are no losses, and the input energy distribution is uniform (ie. $H = A = B = 1$). Consider also the input to be a Dirac delta pulse. Hence:

$$\begin{aligned} F(t,\theta_o) &= \frac{1}{K(\theta_o)} \int_{\theta}^{\theta_o} \delta(t-T)\sin\theta d\theta \\ &= \frac{1}{K(\theta_o)} \int_{T_o}^{T_o/\cos\theta_o} \delta(t-T)(T_o/T^2)dT \\ &= (U(T_o) - U(T_o/\cos\theta_o))(1/T_o)(T_o/t)^2 \end{aligned} \qquad (25)$$

where θ_o is substituted from Equation 18 and 'U' is the Heaviside function.

The pulse broadening is defined as the pulse width at half amplitude and can be immediately deduced from the previous equation as:

$$\Delta t = T_o\ (1/\cos\theta_o - 1) \qquad (26)$$

since for most practical waveguides, $\theta \leq 45^\circ$ and hence the last two terms in Equation 25 do not affect the form of the output pulse.

Ref 16 goes on to show that if the losses are small, then they will not significantly affect the pulse spreading. The conditions that must be met are as follows:

(i) for substance losses:

$$aL/d = \ln 2/\theta_o \qquad (27)$$

(ii) for interface losses:

$$bL = 2\ln 2/\theta_o^2 \ . \qquad (28)$$

Similiarly for the angle dependent energy distribution, if $H(\theta) = \cos^m\theta$ and:

$$m \leq 2\ln 2/\theta_o^2 \qquad (29)$$

(ie. reasonably flat energy input) then the pulse broadening is not significantly affected. If a light source with confined axial energy is utilized (ie. laser diode), it can then be shown that 'm' in the previous equation becomes large and hence the pulse broadening can be derived to be:

$$\triangle t = T_o \left(2^{1/(m+2)} - 1\right) \qquad (30)$$

(iii) Ideal Graded Index Fibre

Depicted in Fig 25b is an uncladded graded index fibre. For this structure, the ray path has to obey the eikonal equation:

$$\frac{d}{ds}\left\{ n \frac{d\vec{r}}{ds} \right\} = \nabla n \tag{31}$$

In the x,z plane for meridional rays one must solve the reduced eikonal equation:

$$\frac{d^2x}{dz^2} = \frac{1}{n}(1 + (dx/dz)^2)(dn/dx) \tag{32}$$

According to Steiner (Ref 18) the refractive index can be expanded in a power series and hence the previous equation can be shown to reduce to:

$$\begin{aligned} x(z) = \frac{\theta}{a^{\frac{1}{2}}}\Big\{ & (1 + \frac{\theta^2}{32}(9b/a^2 - 5/6))\sin za^{\frac{1}{2}} \\ & + \frac{\theta^2}{32}(b/a^2 + 1/2)\sin 3za^{\frac{1}{2}} \\ & - \frac{\theta^2}{8}(3b/a^{\frac{1}{2}} - 5/2)za^{\frac{1}{2}}\cos za^{\frac{1}{2}} + R(\theta^4)\Big\} \end{aligned} \tag{33}$$

where $R(\theta^4)$ is the residue for the higher powers of θ and can be neglected for practical waveguides. The ray delay along the waveguide is:

$$T = 1/c \int_0^L n\, ds = 1/c \int_0^L n(1 + (dx/dz)^2)^{\frac{1}{2}}\, dz \tag{34}$$

hence,

$$\Delta t = (3T_0/32)(5/6 - b/a^2)\,\theta^4 \tag{35}$$

and 'a' and 'b' are co-efficients in a power series of the index profile.

For the graded-index fibre, skew rays propagate along the fibre in the form of helical rays and can transport a great deal of energy. These skew rays are generated if the light is not axially launched into the fibre. For these rays, the broadening can be shown to be (according to Ref 17):

$$\Delta t = (T_0/\cos\theta)(1 - ax^2/2 + bx^4/4 +,- \ldots\ldots) \tag{36}$$

The previous equation is the general form for helical rays and the pulse spreading can be much larger than that for meridional rays.

(iv) Cladded Graded-Index Fibres

Fig 25c shows the ray propagation in a cladded graded-index fibre. As can be seen, for rays which no longer travel smoothly through the fibre (angles greater than θ_0 but less than the critical angle at the interface), they encounter a step interface, and, consequently, one should expect the pulse broadening of this fibre to be much greater than the ideal graded index fibre. For these 'bouncing' rays, the delay time can be calculated as follows:

$$T = \frac{L}{cz^*} \int_0^{z^*} n(1 + (dx/dz)^2)^{\frac{1}{2}}\, dz$$

$$= (Ln_1/c)(1 + (\theta^2 \sin 2(az^*)^{\frac{1}{2}}/(4(az^*)^{\frac{1}{2}})) \tag{37}$$

where $x(z) = (\theta/a^{\frac{1}{2}})\sin za^{\frac{1}{2}}$

$n(x) = n_1\ (1 - ax^2/2)$

Now for small differences $\theta-\theta_0$ (where $\theta=da^{\frac{1}{2}}$):

$$z^* = (\pi/2 - (2-2\theta_0/\theta)^{\frac{1}{2}})/a^{\frac{1}{2}} \tag{38}$$

which implies:

$$\Delta t = T_0(\theta^2/\pi)(2-2\theta_0/\theta)^{\frac{1}{2}} \tag{39}$$

As can be seen, for angles less than θ_0, the fibre acts as an ideal graded-index waveguide. For angles greater than θ_0 and less than the critical angle of the core and cladding, the pulse broadening is as given above.

(v) Validation of Assumptions

In the previous discussions, various assumptions had been made in order to simplify the mathematical analysis which yield the expressions for pulse spreading in optical fibres. At this point, it is prudent to verify the validity of these assumptions. In particular, for the step index fibre it has been assumed that:

(i) losses are negligible;

(ii) the input pulse is a Dirac delta function;

(iii) fibre critical angle $\leq 45^\circ$.

For the graded index fibre, it has been assumed that:

(i) losses are negligible;

(ii) the index of refraction distribution of the core is quadratic;

(iii) the input is a Dirac delta function.

Since any work of this type requires a mathematical model of the real fibres, one usually makes assumptions based upon the real physical situation. In this case, the current state of the art can produce fibres with losses less than 1 dB/Km it is therefore reasonable to assume that pulse spreading due to fibre losses is negligible. For step idex fibres, the core and cladding have indices of refraction which are very similiar and hence the condition that $\theta \leq 45^{\circ}$ is always satisfied. For graded index fibres, the construction techniques are not very accurate and hence the index profile may change with distance. To use a profile of higher order than quadratic is not worthwhile. A quadratic profile can at best give a mean value of the distribution.

The most interesting assumption in both cases is that of an impulse as an input, since real impulses are physically unrealizable! Despite this unfortunate restriction, the previous analysis is still valid since the 'impulse resonse' of the fibre can be calculated through the use of the Fourier transform. This can be seen as follows: assume the input signal to the fibre to be r(t) and the ouput signal from the fibre to be c(t). Both of these signals can be measured. If the signals are measured with the same photodetector, then any measurement non-linearity can be eliminated. From communications theory, the input-output relationship is:

$$c(t) = r(t) * f(t) \tag{40}$$

where f(t) is the fibre <u>impulse response</u>, and '*' denotes convolution. In the frequency domain this becomes:

$$C(f) = R(f)F(f)$$

$$\text{or} \quad F(f) = C(f)/R(f) \tag{41}$$

Hence, taking the inverse Fourier transform of the ratio of the transforms of the output versus the input will yield the fibre impulse response. This procedure is only possible through the use of digital computers. All subsequent experimental work in the report will use this method in conjunction with the program listed in the Appendix.

As can be seen, the assumptions utilized in this report are reasonable within the accuracy limits of the fibre construction and measurement system. The Appendix gives a proof showing that Equation 41 is also valid for discrete systems.

5- Terminal Electronics

(i) Transmitter Terminal Electronics

(a) Double Heterojunction Lasers

Chapter 1 has discussed the advantages of pulse code modulation over other types of modulation techniques. This chapter will present the transmitter terminal electronics required to implement PCM systems. The basic design employs an emitter-coupled transistor pair driving a forward biased double heterojunction laser diode. Fig 26 depicts the current-light output curve of an RCA 30130 DH laser diode measured at about 30°C. This output characteristic corresponds closely to that given in Chapter 2. As has been pointed out, the light intensity output is very temperature sensitive. The diode must therefore be well heatsinked and kept cool (near room temperature), otherwise the current level required for threshold may rise above the level of the bias current with the consequent loss of lasing action. The present design employs a bias current (I_b) of 220 mA and a modulating current (I_{mod}) of 20 mA. This arrangement yields a quiescent power level (P_q) of about 1.5mW and a signal power level (P_{sig}) of about 1.3 mW. The need for biasing slightly above threshold is to improve the high frequency response.

Fig 27 illustrates the laser drive circuit under consideration. This circuit was derived from the work done by M. Chown (Ref 7). The laser is biased by a current source delivering 240 mA through a ferrite bead. The ferrite beads are necessary to reduce stray capacitive coupling and inductive effects of the power supply and its connections to the laser and its drive circuitry. A monitor output BNC connector is

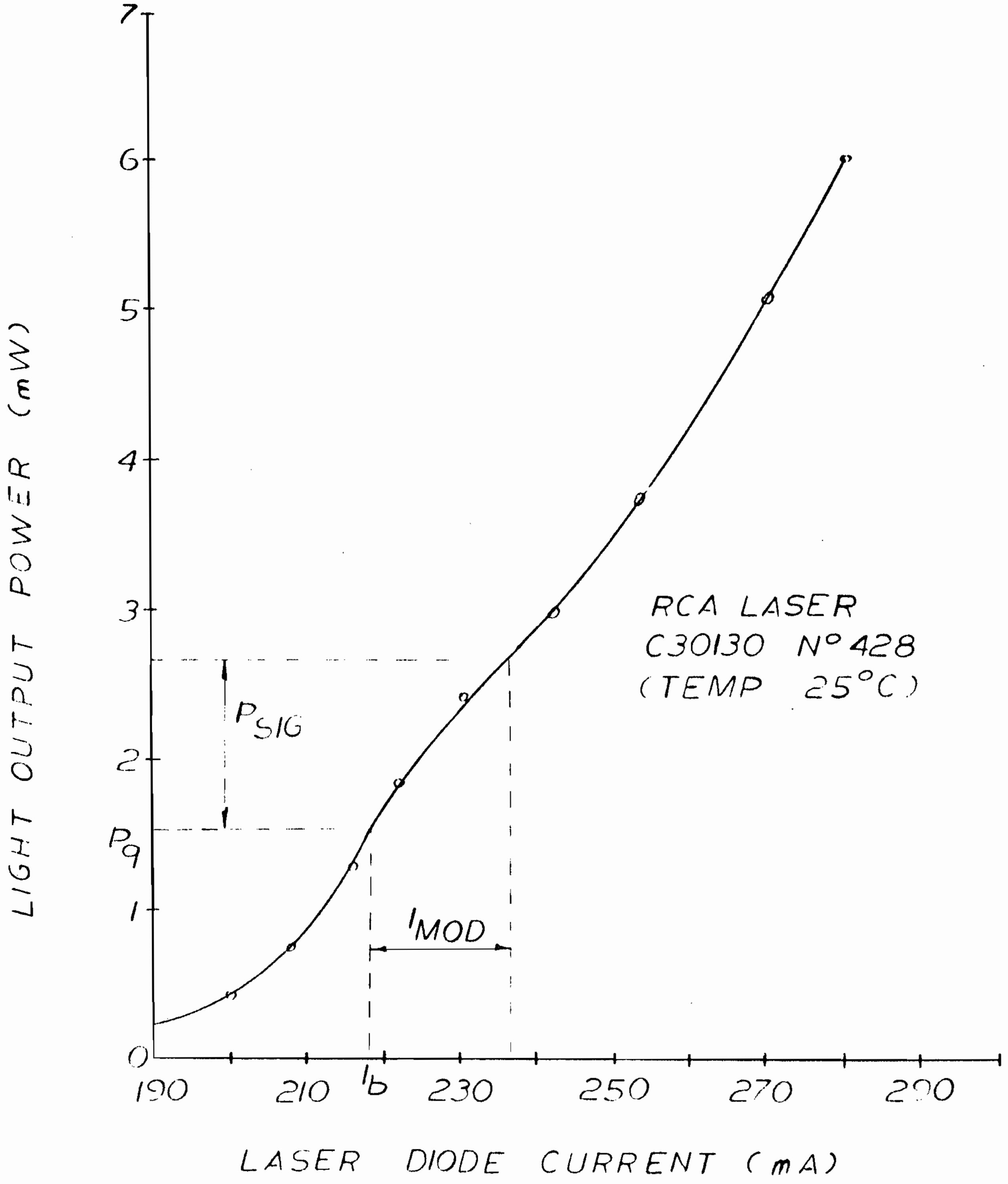

Fig. 26 Laser light output response curve.

provided to facilitate the adjustment of the various current sources and of the input pulse shape so as to generate a narrow, well defined output light pulse.

Modulation of the laser diode is performed by switching a current back and forth between an emitter-coupled transistor pair. This circuit configuration is typical of a differential amplifier. In this mode of operation, both transistors are operating in the linear region of their characteristic curves. Hence, since neither transistor is ever in cut-off or in saturation, minimal charge-storage effects are encountered. The result is that these transistors will be operating at their maximum rates. The gain-bandwidth product of the RCA type SK3019 transistor is 1.6 GHz, which should be sufficient to handle pulses of a few nanoseconds in duration.

The laser modulation process is carried out as follows: under quiescent conditions, $I_1 = I_2$. The transistor bias current (I_{bt}) is always equal to $I_1 + I_2$ and is adjusted to 40 mA. Hence, under quiescent conditions $I_1 = I_2 = 20$mA. Therefore, the laser bias current (I_b) is equal to the laser current source (I_{cs}) minus I_2 (ie. $I_{cs} - I_2 = 240-20 = 220$ mA). Applying an input pulse of up to 0.5 V in height causes Q_1 to switch on and Q_2 to switch off. This results in having $I_2 = 0$ and $I_1 = I_{bt} =$ 40 mA. This causes I_b to increase to I_{cs} (ie. $I_b=I_{cs}-I_2$, but $I_2=0$, therefore $I_b=I_{cs}=240$ mA). Hence, a positive going signal pulse causes an increasing intensity output light pulse. Fig 28 shows how current sources can be constructed through the use of integrated voltage regulators.

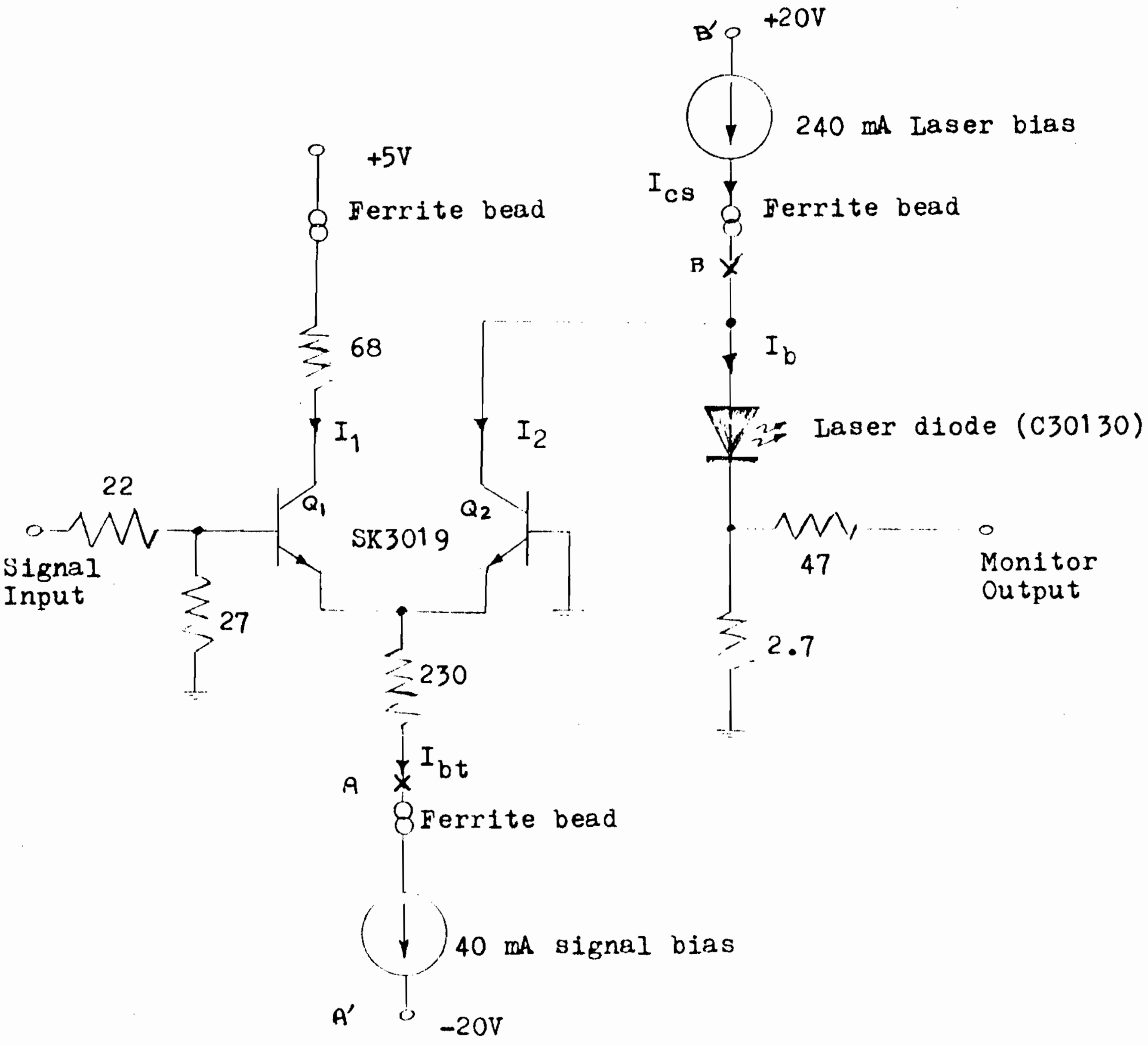

Fig. 27 Double heterojunction biasing and drive circuitry.

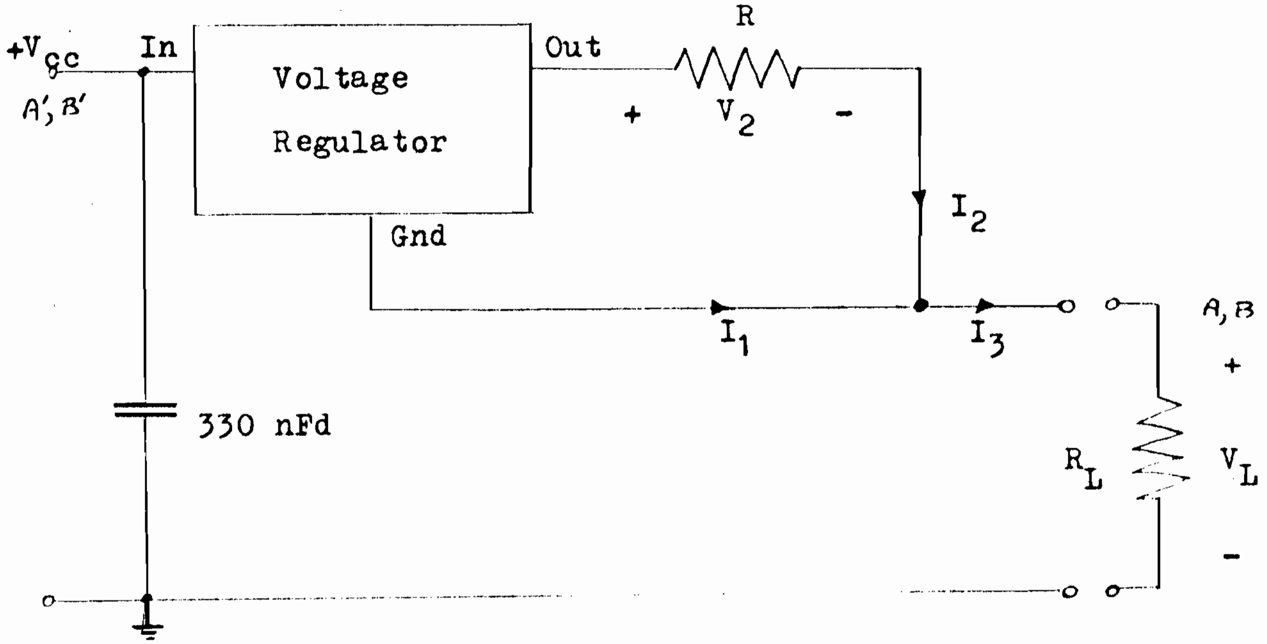

I_1 = Quiescent current $\ll I_2$

$I_2 \approx I_3$ = current through load

V_2 = Regulator output voltage

$(V_{cc} - V_2)_{min}$ = Regulator drop-out voltage (typ. 2V)

$(V_{cc} - V_L)_{max}$ = Maximum voltage rating of the regulator

$\therefore I_L = I_3 \approx V_2/R$

$V_L = I_L R_L \approx V_2(R_L/R)$

Fig. 28 Voltage regulator utilized as a current source.

(b) Single Heterojunction Lasers

One drawback of the DH lasers is that in the cw mode of operation, the peak light intensity is relatively low, hence other means of operating the laser must be found. The most convenient way to achieve large light spikes is through the avalanche characteristics of normal signal transistors. In this type of operation, large current spikes in excess of 15 Amperes can be generated for very brief durations (10's of nanosec). Due to the non-liearity of the avalanche process, the exact value of the peak current cannot be exactly predicted, hence, it is advisable to use single heterojunction lasers for this application since they are cheaper and more rugged. Another advantage of SH lasers is that much more intense light spikes can be produced and, consequently, fibre coupling and attenuation are not as critical as with DH lasers. The advantages that DH lasers do have is that they require smaller currents, and, hence, ringing transients are less of a problem. SH laser drivers must therefore be carefully laid out so as to reduce adverse coupling and ringing.

Fig 29 depicts the avalanche transistor driver circuit. The operation of this scheme is as follows: the normal breakdown voltage of the transistor is about 60V; by applying 150V, the transistor charateristics are similiar to those of the avalanche photodiode-a small trigger signal at the base causes a massive current to flow through the transistor. The magnitude of the current is determined by the RC charging circuit at the transistor collector. The duration of the current spike is determined by the size of the collector capacitor and the effective impedances of the transistor and laser diode. A by-pass resistor across the laser diode is provided to prevent any damage to the diode by reverse currents.

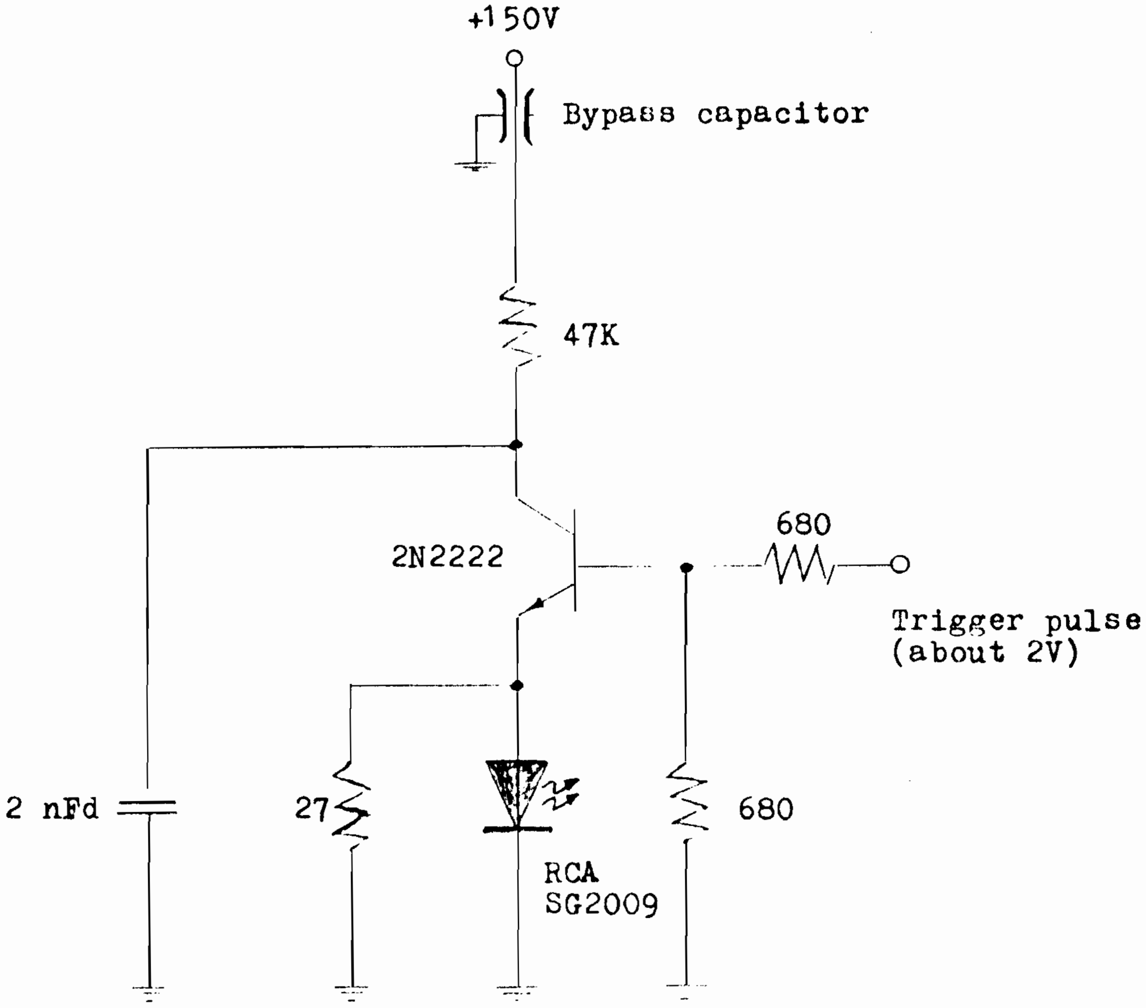

Fig 29 Avalanche transistor driver circuit.

This circuit has been sucessfully employed to generate pulses of about 10 nsec duration. The high threshold conditions of the SH lasers that were employed precluded the generation of narrow pulses. This is caused by a trade-off between current magnitude and current spike width, both of which are dependent upon the capacitor.

(ii) Receiver Electronics

The receiver is depicted in Fig 30. Its construction was kept as simple as possible so as not to introduce any unwanted effects. The avalanche photodetector is an RCA 30902 with rise time of 500 psec. The circuit has been designed with the considerations of Chapter 3 in mind: the 200K resistor is for protection against excessive current which could destroy the diode; and the 50 ohm resistor is the load. It has been chosen so as to provide a large gain-bandwidth product as well as matching impedances with the sampling oscilloscope.

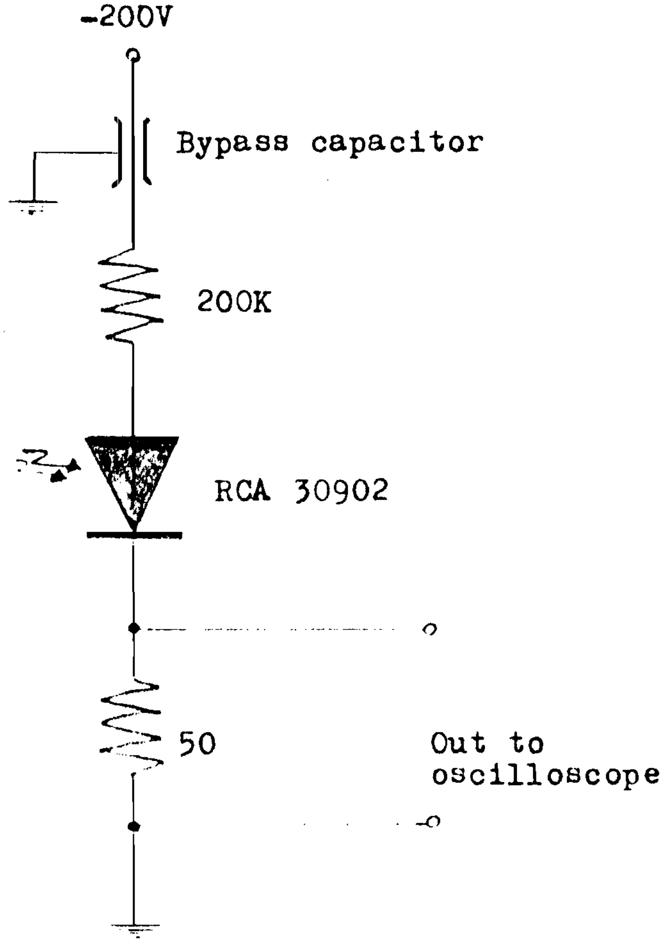

Fig. 30 Receiver electronics.

6- Experimental Apparatus for Impulse Response Measurements

(i) Apparatus

Fig 31 shows the diagramatic layout of the measurement system. The optical fibre under test is wound on a drum and its ends are prepared and then aligned with the laser and photodiode through the use of 6 and 5 degree of freedom micropositioners (3 angles and 3 axes). A signal generator provides the pulse for the transmitter as well as synchronizing the sampling oscilloscope. The receiver output is directly fed into the oscilloscope thus utilizing the 'scope's internal amplifiers for gain.

The photographs in Fig 32 show the actual measurement system. In Fig 32a one can see all of the system's constituents. Note that the receiver and transmitter modules have been mounted on heavy metal stands and that all of the parts have been mounted on a large, heavy gauge aluminum platform which has been isolated from the workbench by a heavy foam pad. This is to ensure that external vibrations will not cause any alignment problems.

Fig 32b shows a close-up of the transmitter. The transmitter that is shown is the DH laser driver. It is within a closed metal box so as not to be influenced by external electro-magnetic fields. The laser is also surrounded by a cooling collar which maintains the laser at a relatively constant temperature and, hence, stabilizes the output light intensity. Fig 32c shows the inside of the DH laser driver. All components are point to point wired to reduce the distances and they are also mounted over a copper ground plane. The bias current is decoupled through a capacitor - inductor arrangement (upper right corner). All

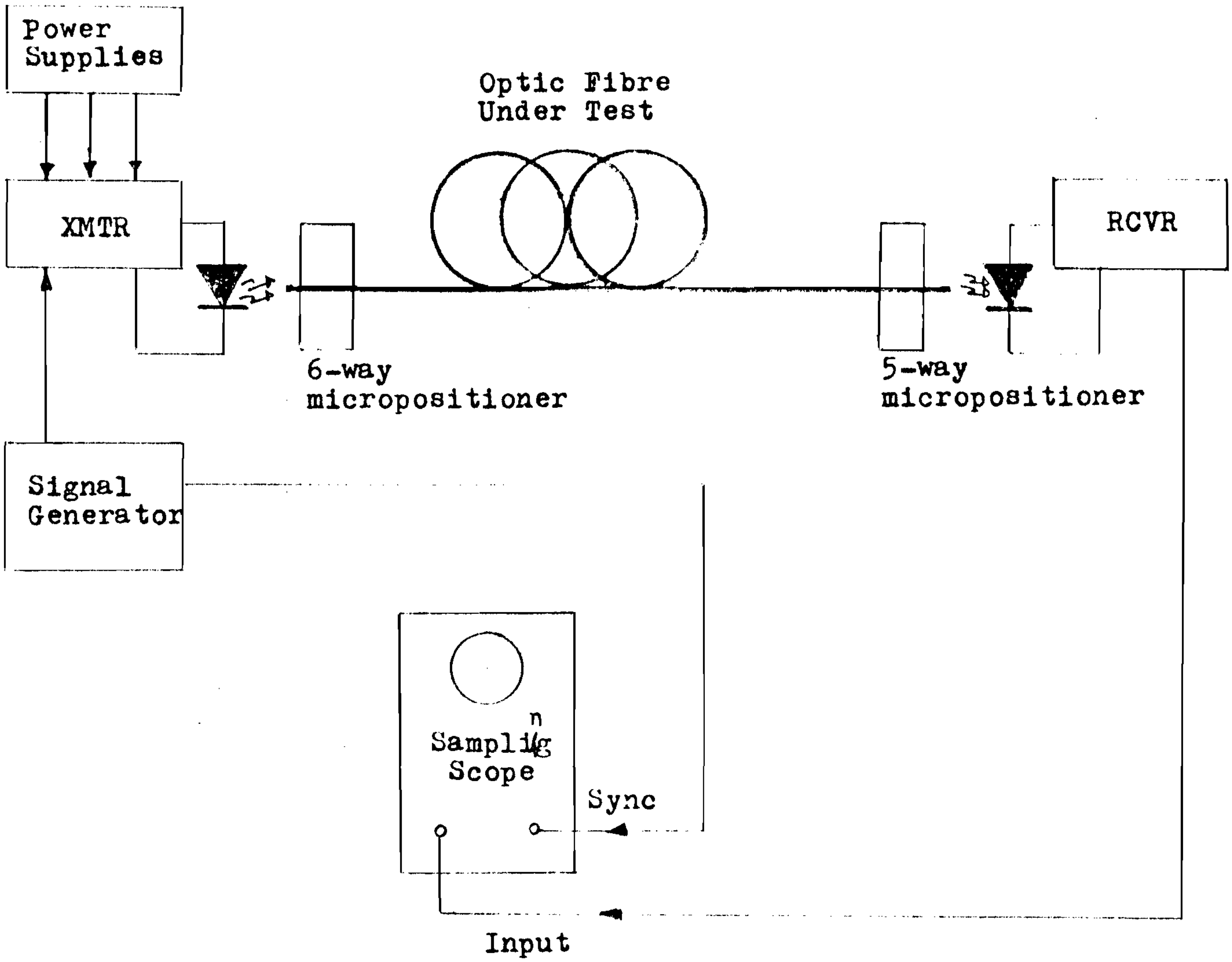

Fig 31 Diagramatic layout of measurement system.

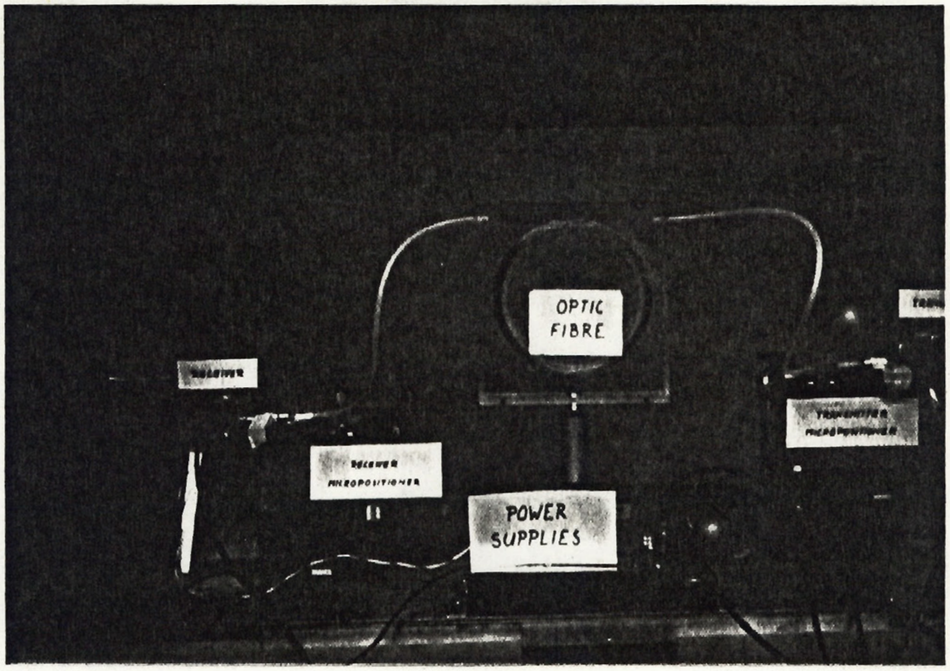

Fig. 32a Arrangement of the measurement system.

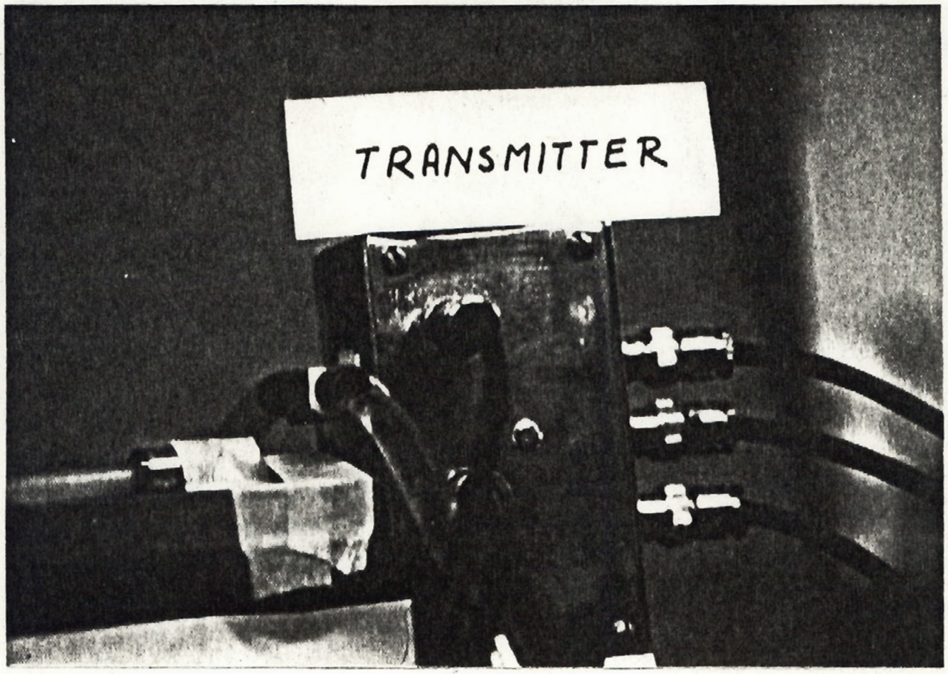

Fig. 32b Close-up of transmitter module.

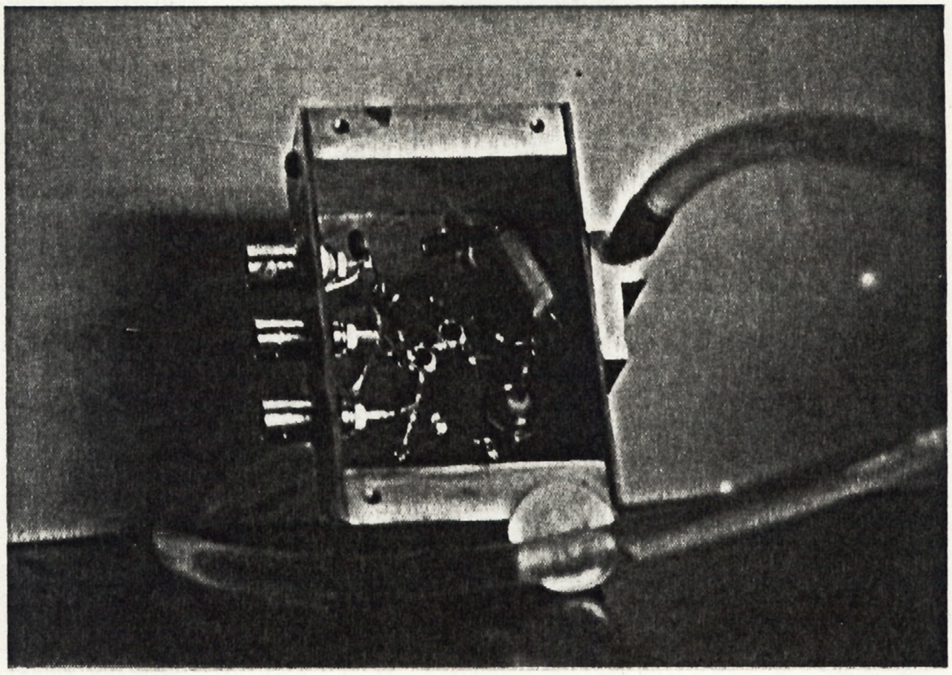

Fig 32c Internal construction of the transmitter module.

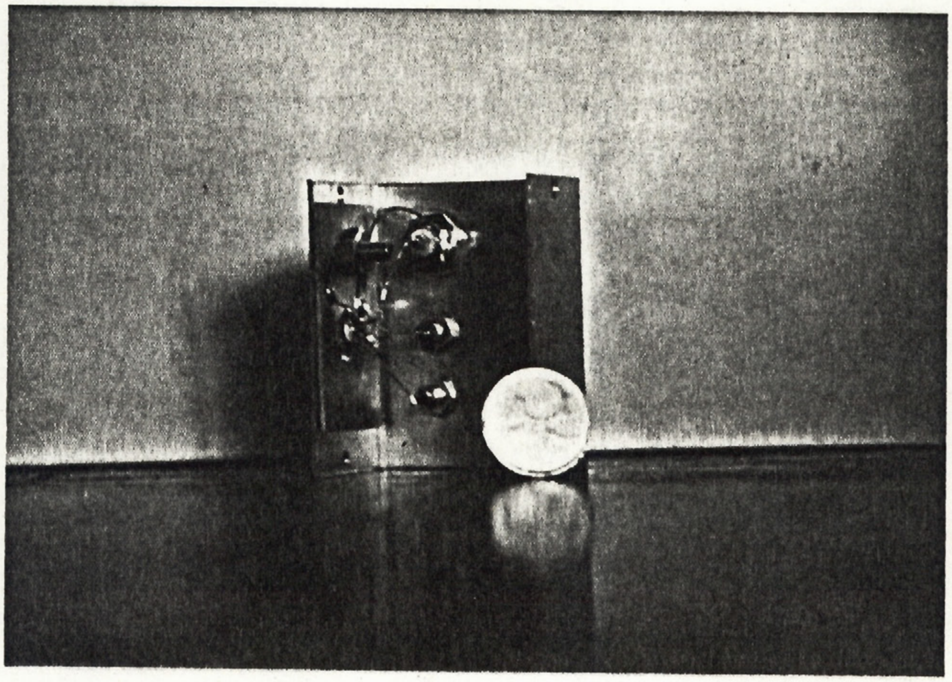

Fig 32d Internal construction of the receiver module.

other supplies are decoupled by capacitors.

A similiar arrangement was used for the SH laser. In this case, however, the component placement was more critical due to the large currents involved. Ideally, one would like to use thick film technology, thereby achieving the shortest possible distances between components and hence producing the least transient switching interference.

Fig 32d shows the construction of the receiver module. As can be seen, the construction is very simple; the major concern being supply decoupling. This is accomplished through the use of feedthrough capacitors.

Three fibres were employed in this measurement which were supplied by ITT. These were (Appendix):

(i) a plastic cladded step index (PCS) fibre (ITT PS-05-xx);
(ii) a step index fibre (ITT GS-02-xx);
(iii) a graded index fibre (ITT GG-02-xx).

(ii) Modulation of Double Heterojunction Lasers

The DH laser system was employed as has been mentioned in the previous section. The results of which are depicted in Fig 33. The upper trace is the current monitored at the laser diode and the lower trace is the inverse light output measured by the photodiode through 1 cm of air. Since the avalanche photodiode is negatively biased,a stronger light input causes a more negative output voltage which consequently shows up on the oscilloscope as a drooping signal. As can be seen, there is no simple linear relationship between the current through the laser diode and light output. As per the discussion in Chapter 3, there is a delay between applied current pulse and light output. In this case, the delay is about 7 nsec. Also, by shutting off the applied current very quickly, light ringing transients are avoided. The half-amplitude width of the light spike was about 5 nsec. The light intensity in the cw mode was too low to overcome the fibre coupling losses, consequently no meaningful measurements were obtained.

Another major problem encountered was that of drifting light intensity, which was due to excessive thermal heating at the laser junction. A cooling jacket helped to alleviate some of the problem, but a proper feedback circuit for the bias current would probably have provided a better alternative.

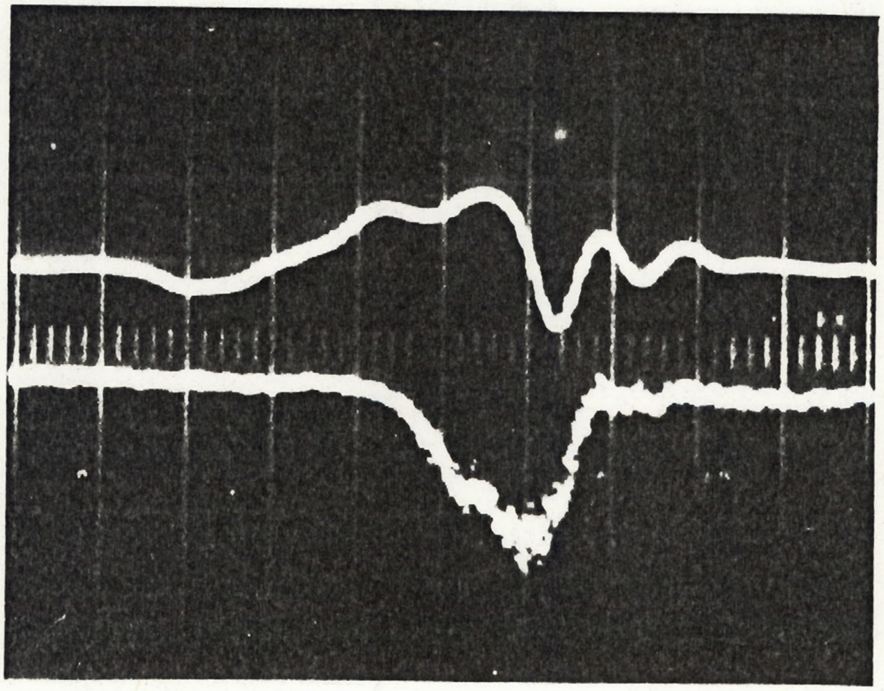

Fig. 33 DH laser light ouput (5 nsec/div);
upper trace: current monitor;
lower trace: inverted light output through
1 cm of air.

(iii) Modulation of Single Heterojunction Lasers

The lack of success with the DH laser prompted the use of SH lasers with their higher light outputs. The result of the circuit of Fig 29 in the system of Fig 31 is depicted in Fig 34a. The lower trace is the resulting light output measured by the photodiode through 3 cm of air. Again, there is no simple relationship between the current through the laser diode and the light output. The delay is about 6 nsec and the current is cut-off sufficiently quickly so as to eliminate any ringing in the light signal.

With the higher light output (about 3 watts) of the SH laser, it was possible to perform pulse spreading measurements. Fig 34b depicts the delay encountered between the applied current pulse (upper trace) and the received light pulse after traversing through the PCS fibre (lower trace). As mentioned previously, a trade-off between light output power and pulse width has to be made. For the SH laser employed (RCA type SG2009), a minimum threshold current of about 15 Ampere must be available before laser action sets in. This sets the size of the charging capacitor (Fig 29) and, hence, the minimum light pulse available is about 9 nsec. The results of the measurements are given in the next chapter.

Note: The question of the effect of mismatch between free space and the fibre has not been considered. As an afterthought, it is recommended that a laser with pigtail be used to launch light into the test fibre.

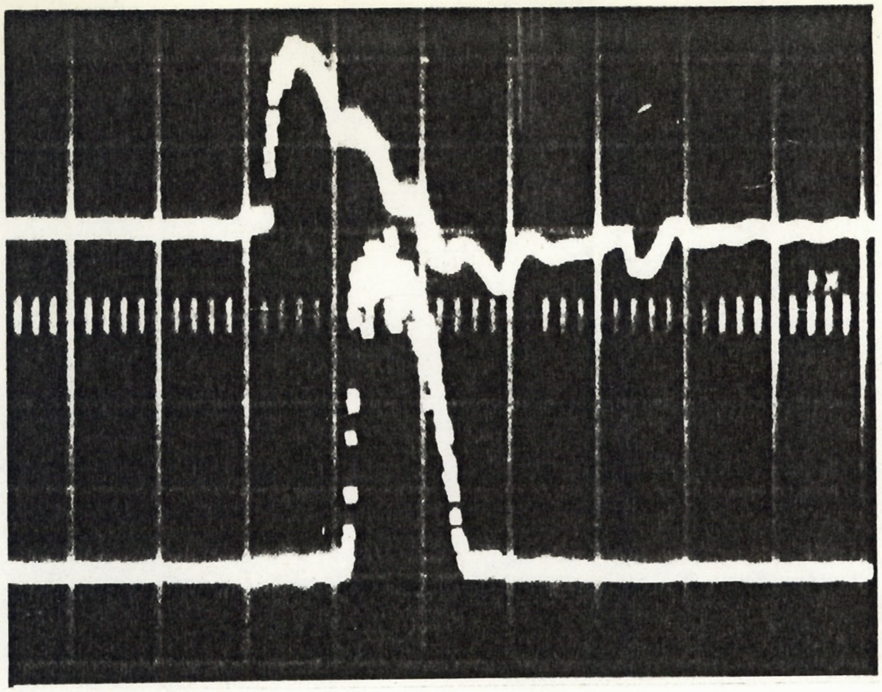

Fig. 34a SH laser output (10 nsec/div);
upper trace: current monitor;
lower trace: light output.

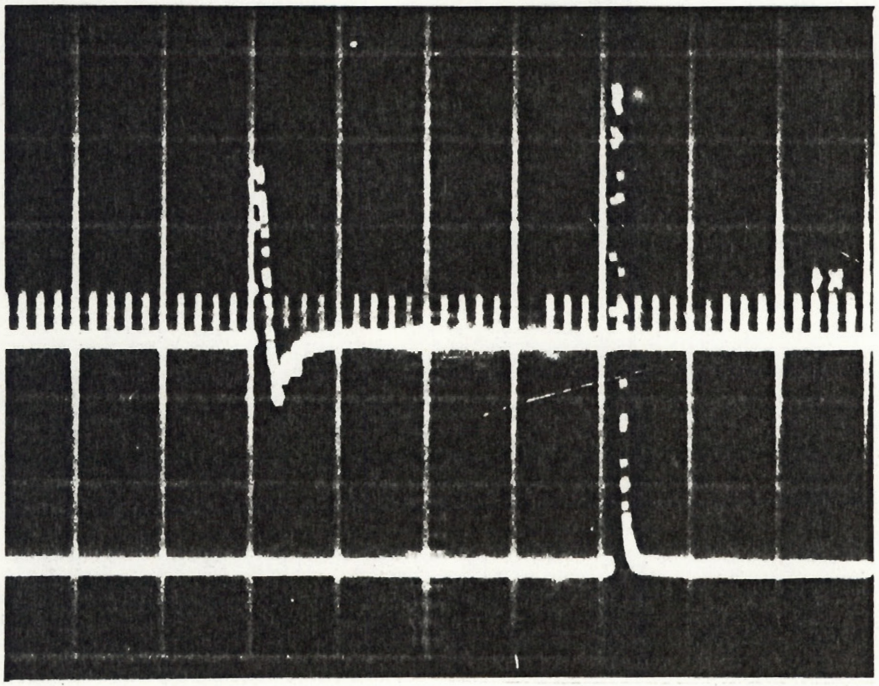

Fig. 34b Transmission through PCS fibre (75 nsec/div);
upper trace: current monitor;
lower trace: fibre output.

7- Discussion of Experimental Results

(i) Experimental Results

Fig 35a shows the applied light pulse. This pulse was generated by the SH laser transmitter discussed previously. Note the excessive ringing transient at the leading edge. This is produced by the large current which is switched through the laser diode. Light transients at the tail of the pulse are absent indicating that proper current cut-off has been acheived.

Fig 35b-d depict the output pulses from the plastic clad step (PCS), step index and graded index fibres respectively. One significant feature to all of the fibre outputs is that transient ringing, seen in the input pulse, does not appear. Since this ringing contains many high frequency components, one can conclude that the optical fibres act as low pass filters. The PCS fibre exhibits the lowest cut-off frequency, with the step index and graded index having respectively higher cut-off points. Fig 36 contains the relevant measured and calculated pulse parameters.

An interesting feature of the graded index fibre output is that its fall time is very long! This is probably due to the excitation of many skew rays. This results because of the method of injecting the light into the fibre: the laser light is directly coupled from the diode into the fibre. The -3 dB intensity half-angle for this particular laser is about 15°; hence, one can expect that the skew rays as well as meridional rays will be excited. This problem can be overcome by utilizing lenses to focus the laser light and, hence, produce a smaller cone angle (Ref 40).

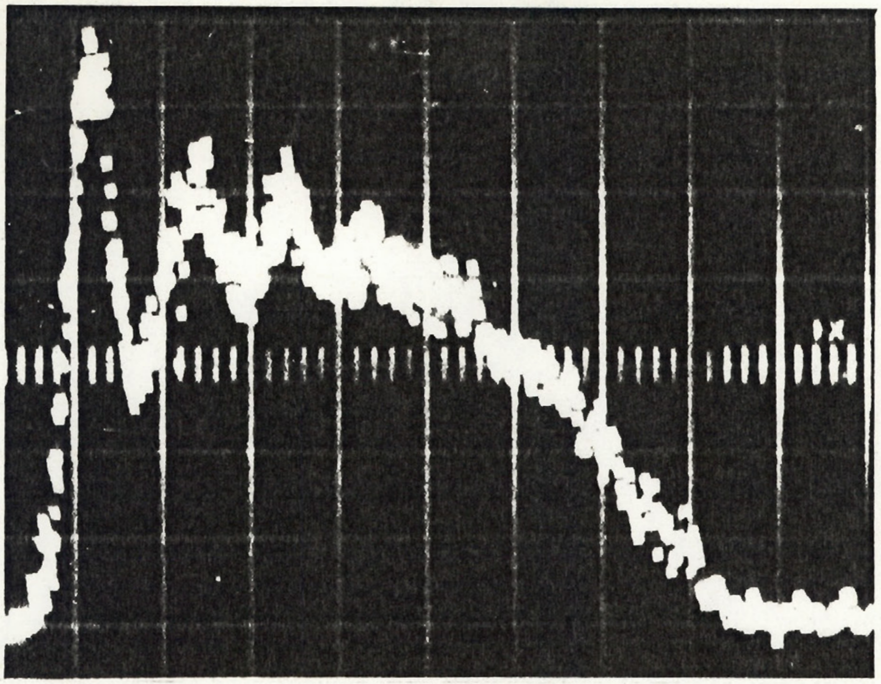

Fig. 35a Input pulse (2 nsec/div).

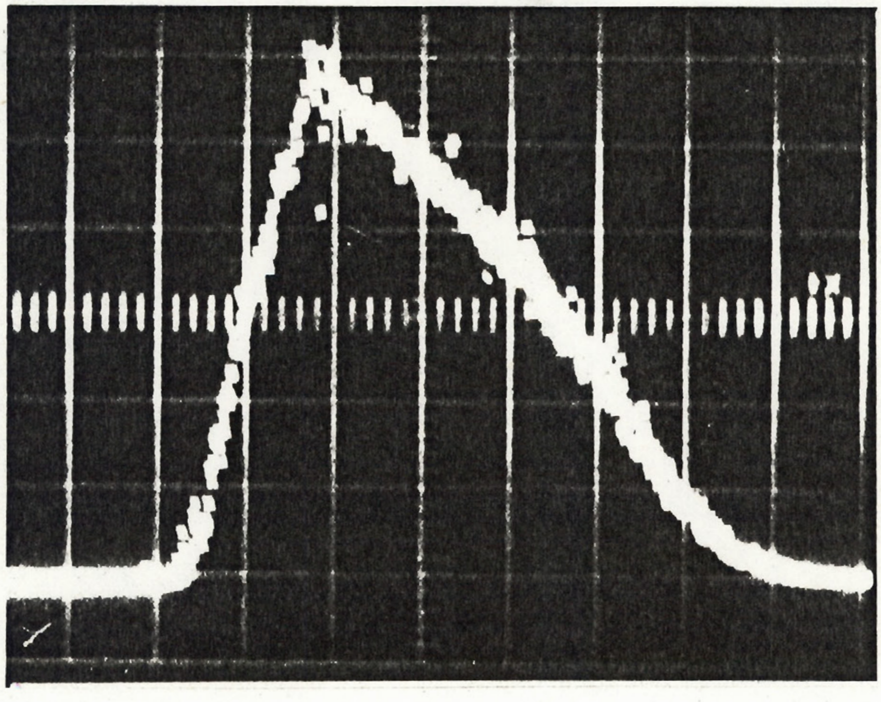

Fig. 35b Output pulse from PCS fibre (2 nsec/div).

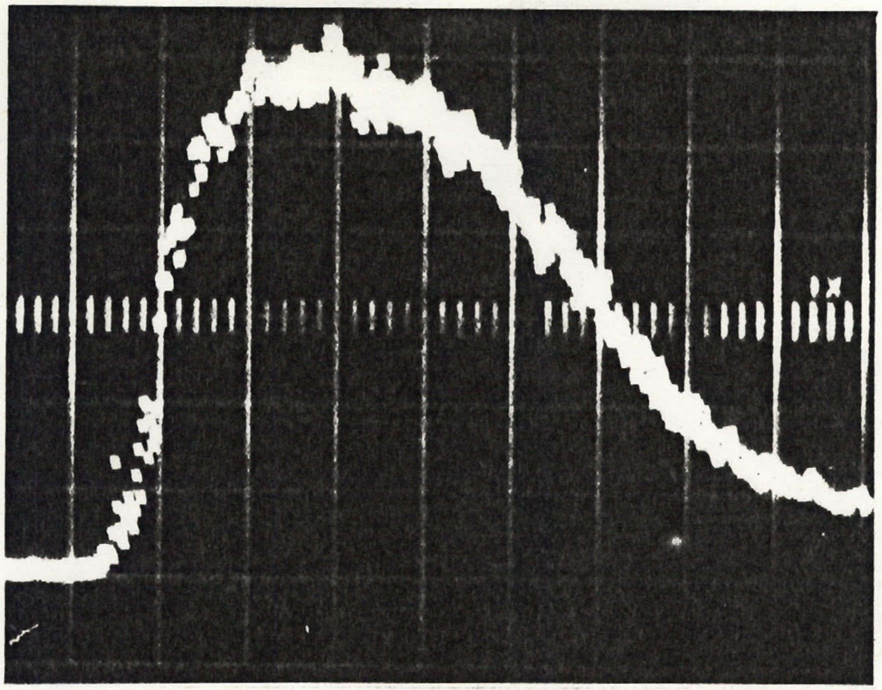

Fig. 35c Output pulse from step index fibre (2 nsec/div).

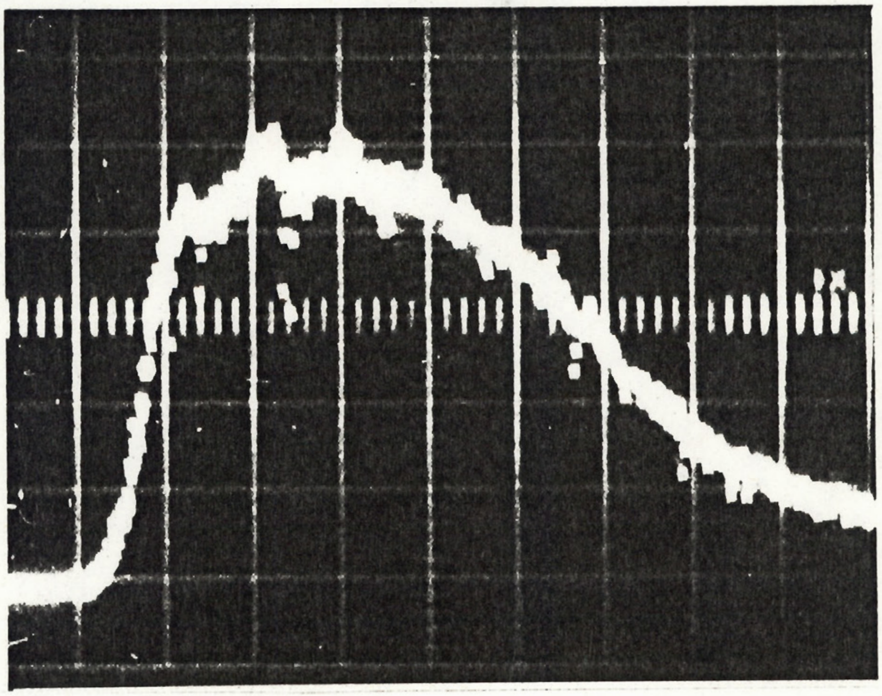

Fig. 35d Output pulse from graded index fibre (2 nsec/div).

	Input pulse	Output pulse from: PCS fibre	Step fibre	Graded fibre
Pulse width (nsec)	9.3	7	10	10.1
Rise time (nsec)	0.7	2	1.6	1
Fall time (nsec)	5	6	5	8
Fibre delay time (nsec)	-	310	280	260
Calculated fibre length (m)	-	63	56	52

Fig. 36 Summary of experimentally measured fibre data.

At this point one can not make any significant measurements pertaining to the pulse spreading (or impulse response) of the glass fibres; except to say that the graded index fibre reproduces the input pulse the best and the PCS fibre is the worst of the lot. By using narrower input light pulses one can produce more significant results. Another alternative is presented in the next section: fibre impulse responses can be calculated through the use of computers and fast Fourier transforms (FFT).

(ii) Refinement by Digital Signal Processing

The refinement of the optical fibre responses was carried out as the method described in Chapter 4. The program that was utilized is given in the Appendix. The fast Fourier transform (FFT) algorithm was adapted from Ref 41. The computation involved forming a 61 point sampled signal by hand (from the photographs) and consequently forming a 256 point Fourier transform. These algorithms require that the input data be symmetric, hence both the real signal and its mirror image must be loaded into the FFT array. Similiarly, the output of the FFT algorithm has the transform and its mirror image. This is to be expected since real waveforms can be represented by a linear superposition of complex waveforms and their complex conjugates.

The effect of truncating a sampled waveform is to introduce ringing into the transform. This is the well known Gibbs phenomenon and can be partially compensated by various weighting functions. Ref 38 discusses the various merits of a few of the more popular functions. As a first approximation (and due to its simplicity), a rectangular filter was employed for the calculations presented here. This filter is necessary since the digital implementation of Equation 41 has difficulty in handling singularities. These singularities arise due to the zeros in the transforms of the input function. In the continuous case, the output function will have zeros at the same place as the input function and in the limit these will cancel. The FFT algorithm, on the other hand, will never produce a transform which is exactly zero at any point - there will always be a residue at any point. Although both output and input transforms will have residues at the same point, the magnitudes of these residues can be radically different. The result will be that a large singularity will be produced in the transform of the fibre impulse response function. The use of a weighting function will eliminate these singularities, but will introduce a slight distortion into the impulse response.

Figs 37a,c,f and i are the sampled input and output waveforms with Figs 37e,h and k being the respective fibre impulse response functions. The significant features of these impulse responses include the ringing due to truncation and a delay between the applied input and the consequent output should have an impulse response which has a rise time of zero and a parabolic fall time for the case where only meridional rays have been excited. For the responses shown here, it can be concluded that other types of rays are propagating in the fibre.

Figs 38a,b and e have been obtained due to the generosity of Mr. Andrej Puc (Ref 40). He has used a DH laser in Q-switching mode to obtain light pulses of about 550 psec duration. Figs 38d and g are the calculated impulse responses and Figs 38c and f are the magnitudes of the Fourier transforms of the fibre impulse responses. These indicate that the optical fibres are essentially low pass filters. As can be seen, the graded index fibre has a higher cut-off frequency as compared to the step index fibre.

The significant differences between the measurements of Fig 37 and 38 are:

(i) the input pulse width of Fig 38 is about 20 times narrower;

(ii) the light pulse of Fig 38 was focused by a lens and consequently its -3 dB power point was about 9° as compared to 30° for Fig 37.

It will be shown in the next section that these two conditions produce radically different results.

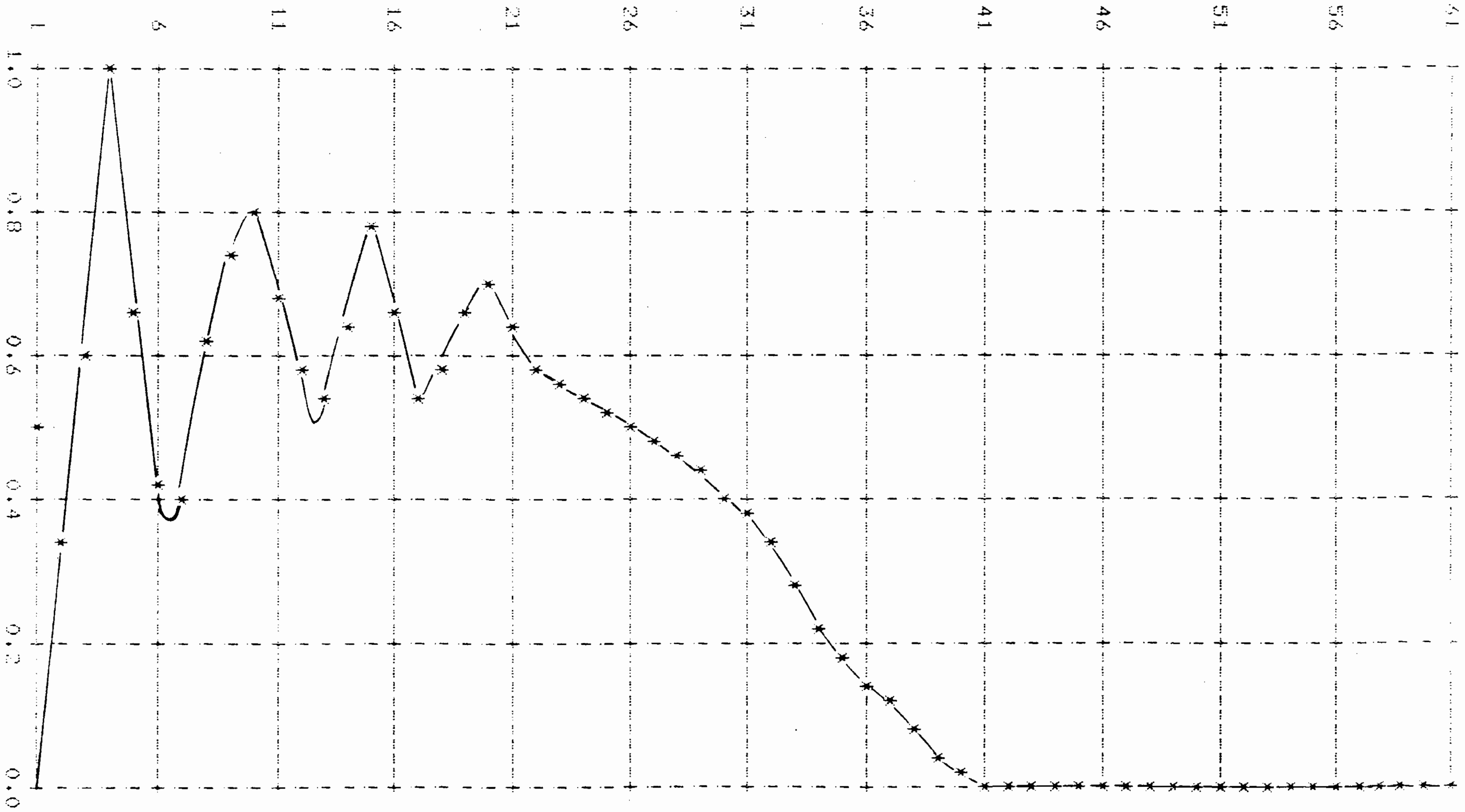

Fig 37a. Input signal (T = 400 psec).

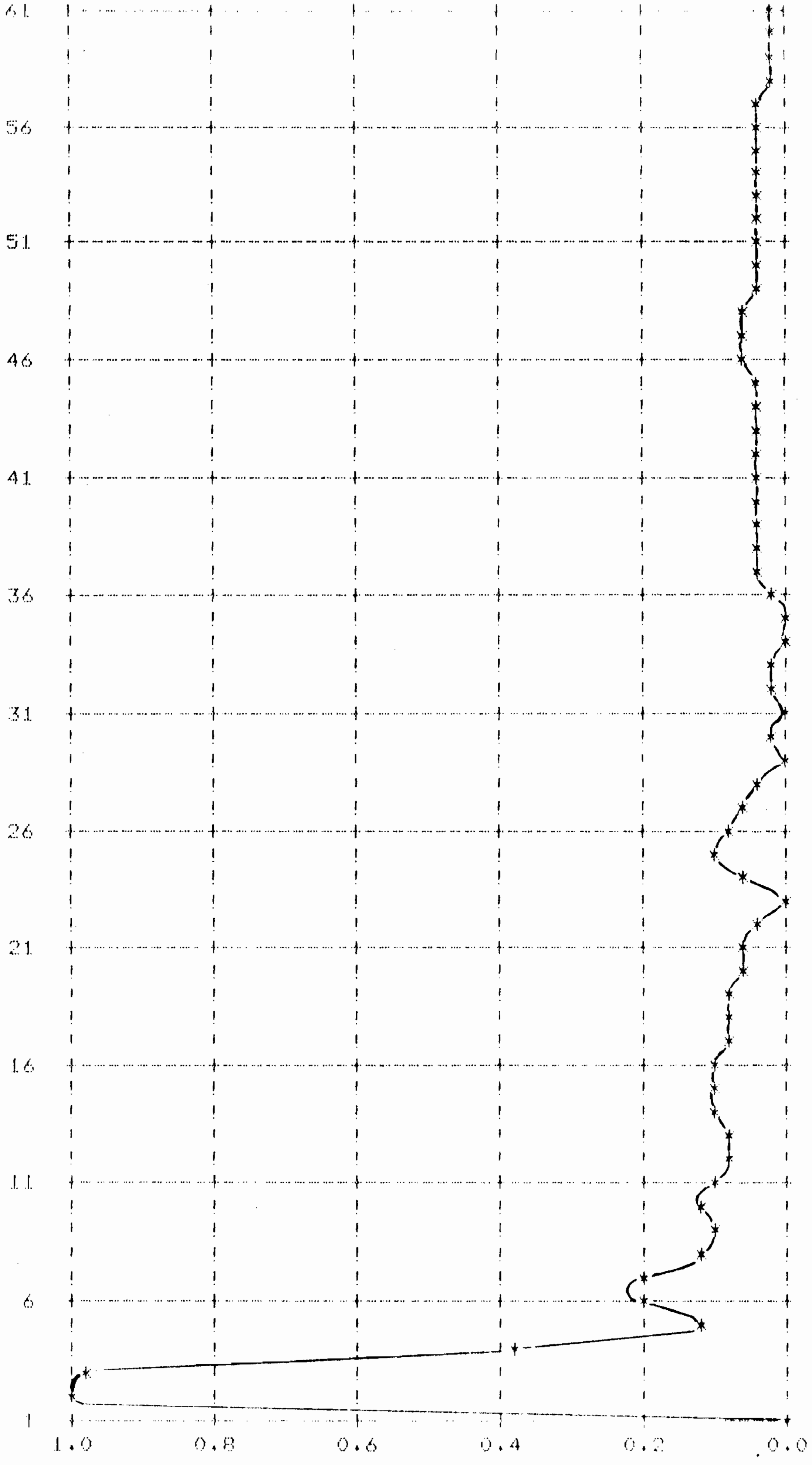

Fig 37b. Fourier transform of input signal.

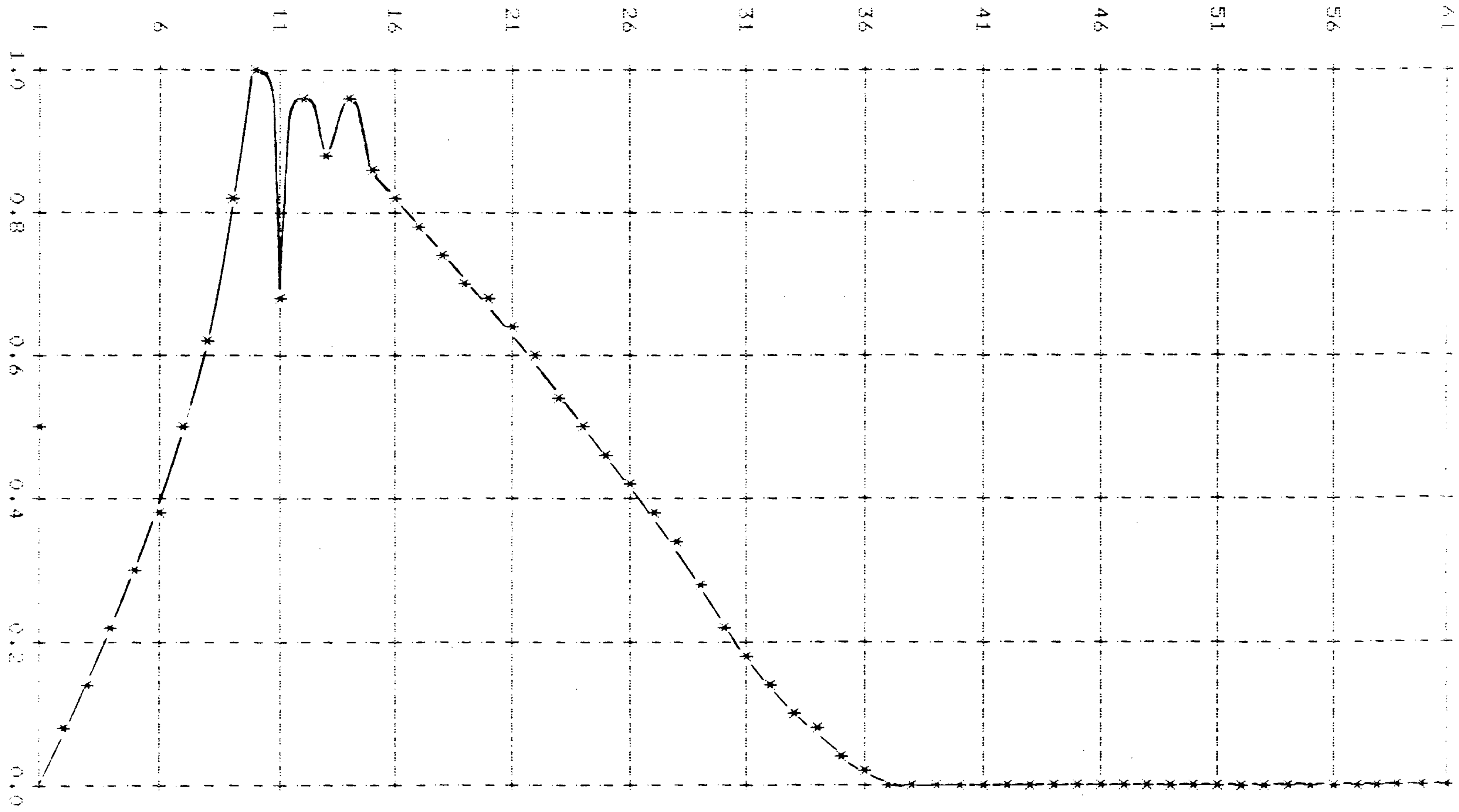

Fig 37c. Output pulse from PCS fibre (T = 400 psec).

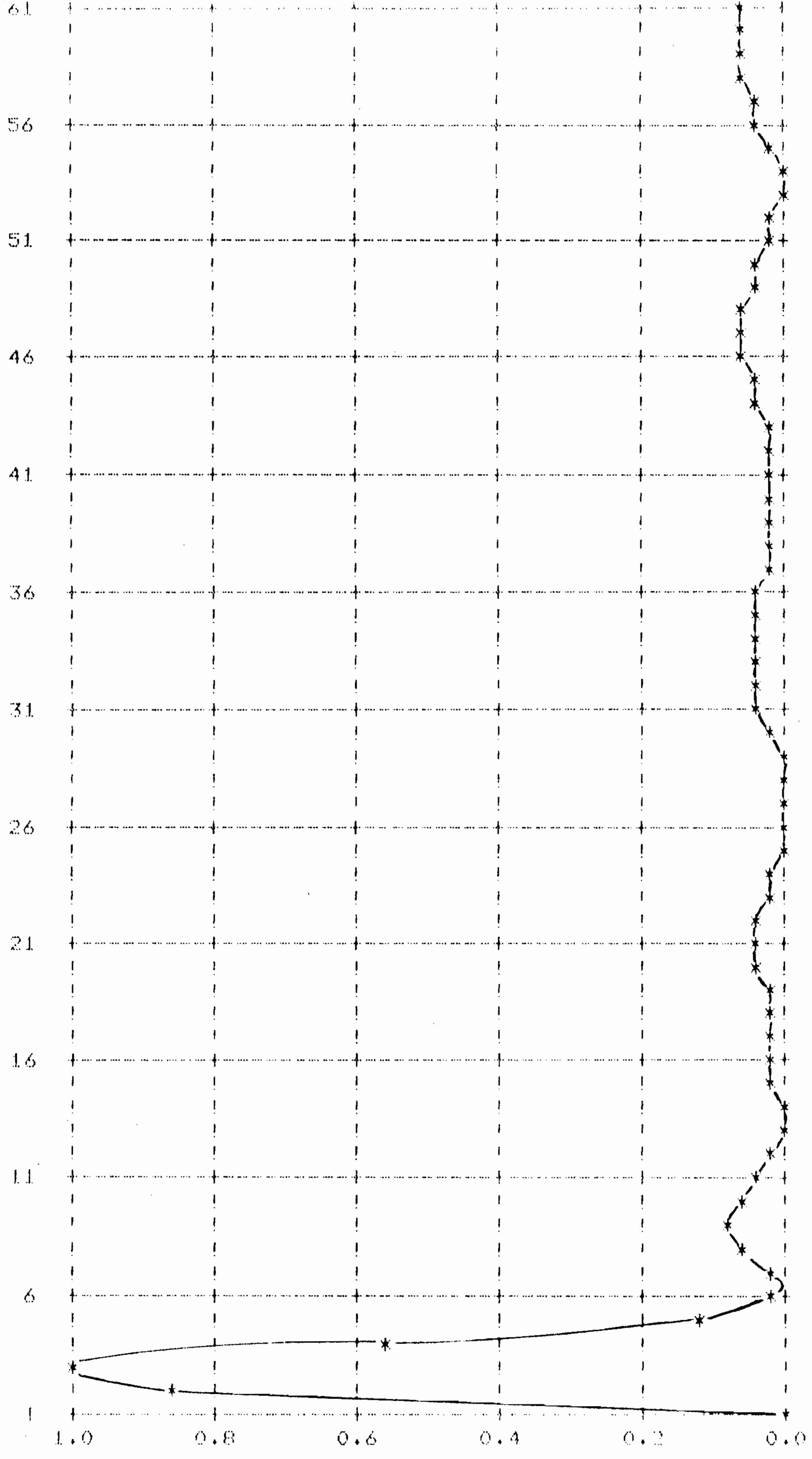

Fig 37d. Fourier transform of the output pulse of the PCS fibre.

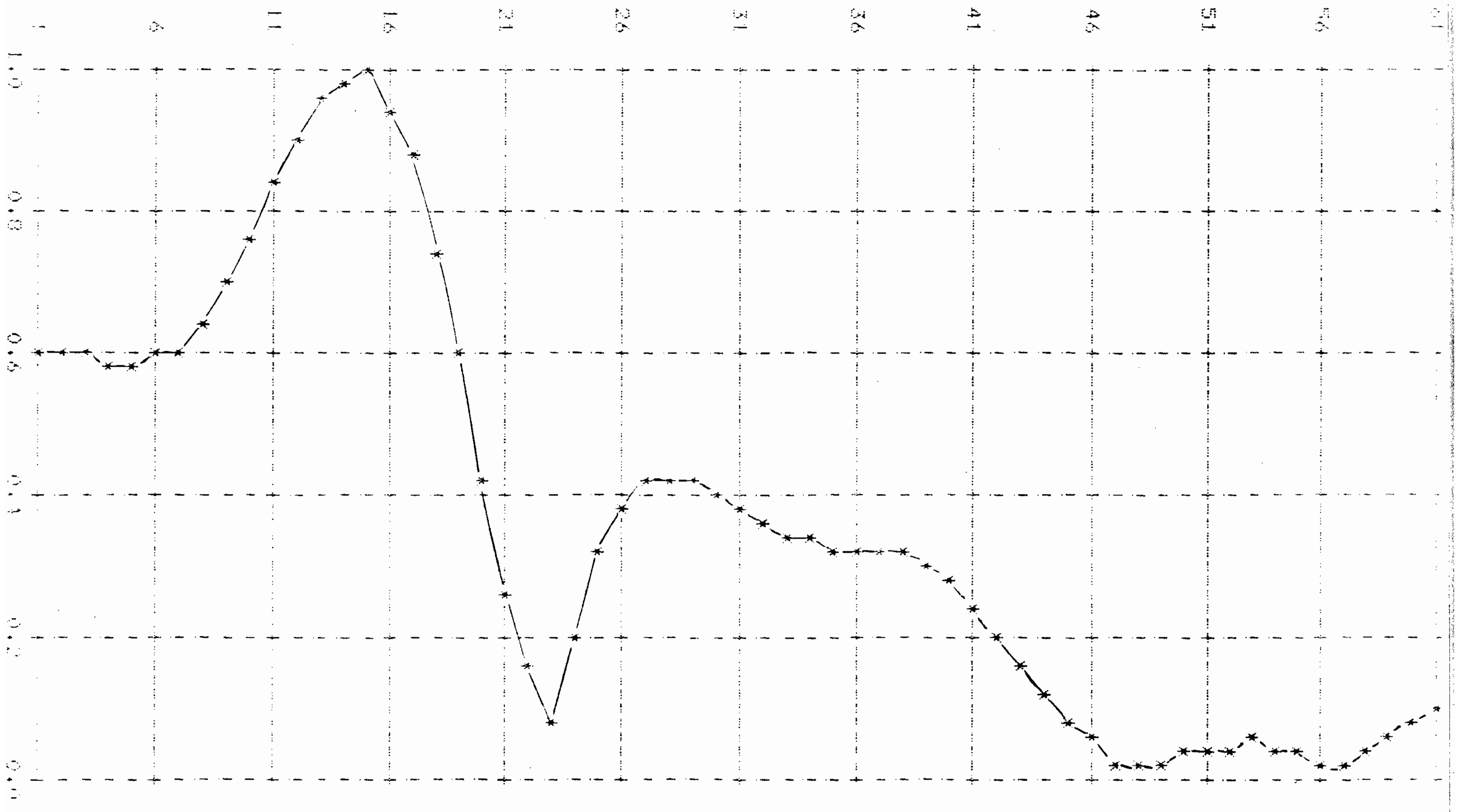

Fig 37e. Impulse response of the PCS fibre (T = 200 psec).

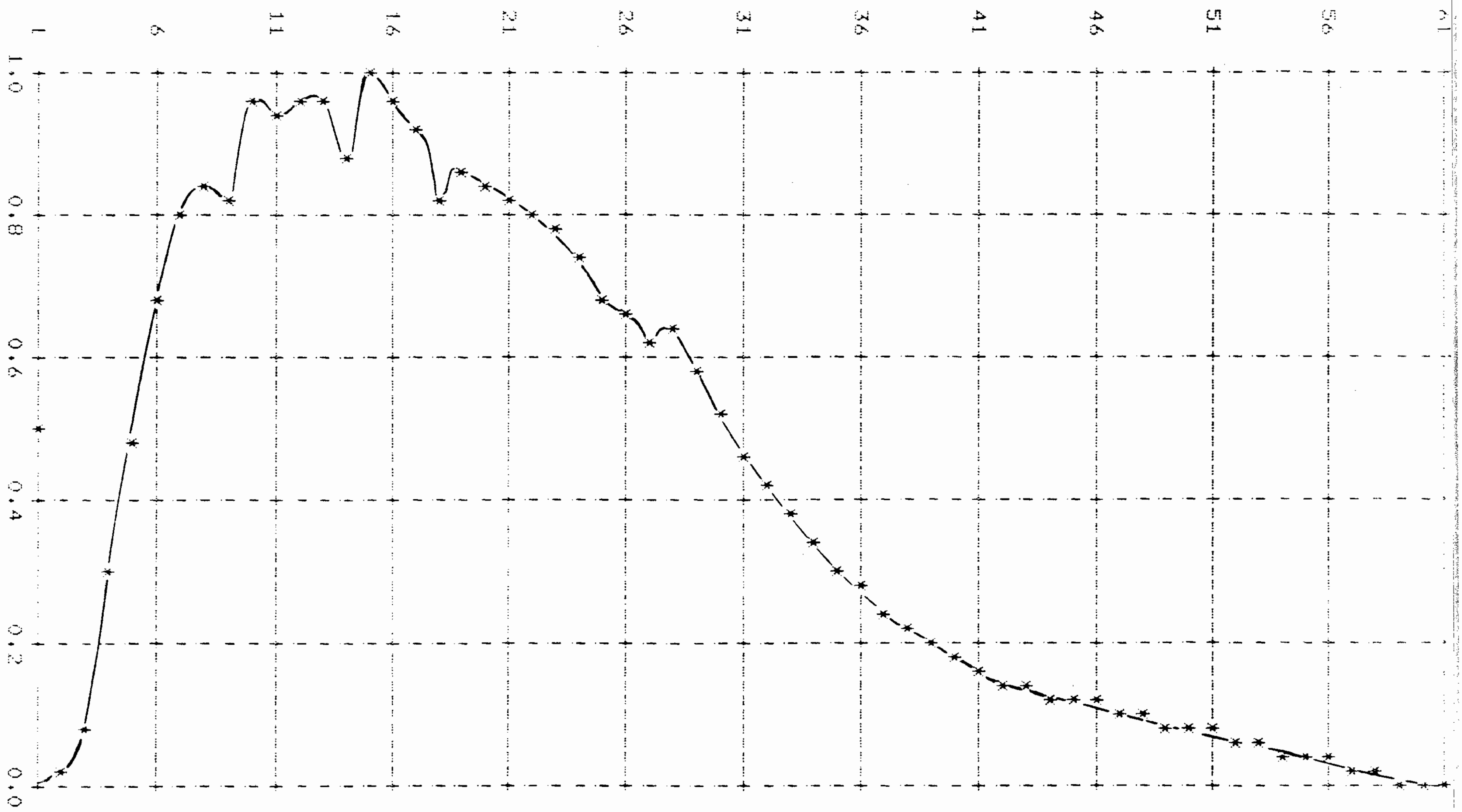

Fig 37f. Output pulse from the step index fibre (T = 400 psec).

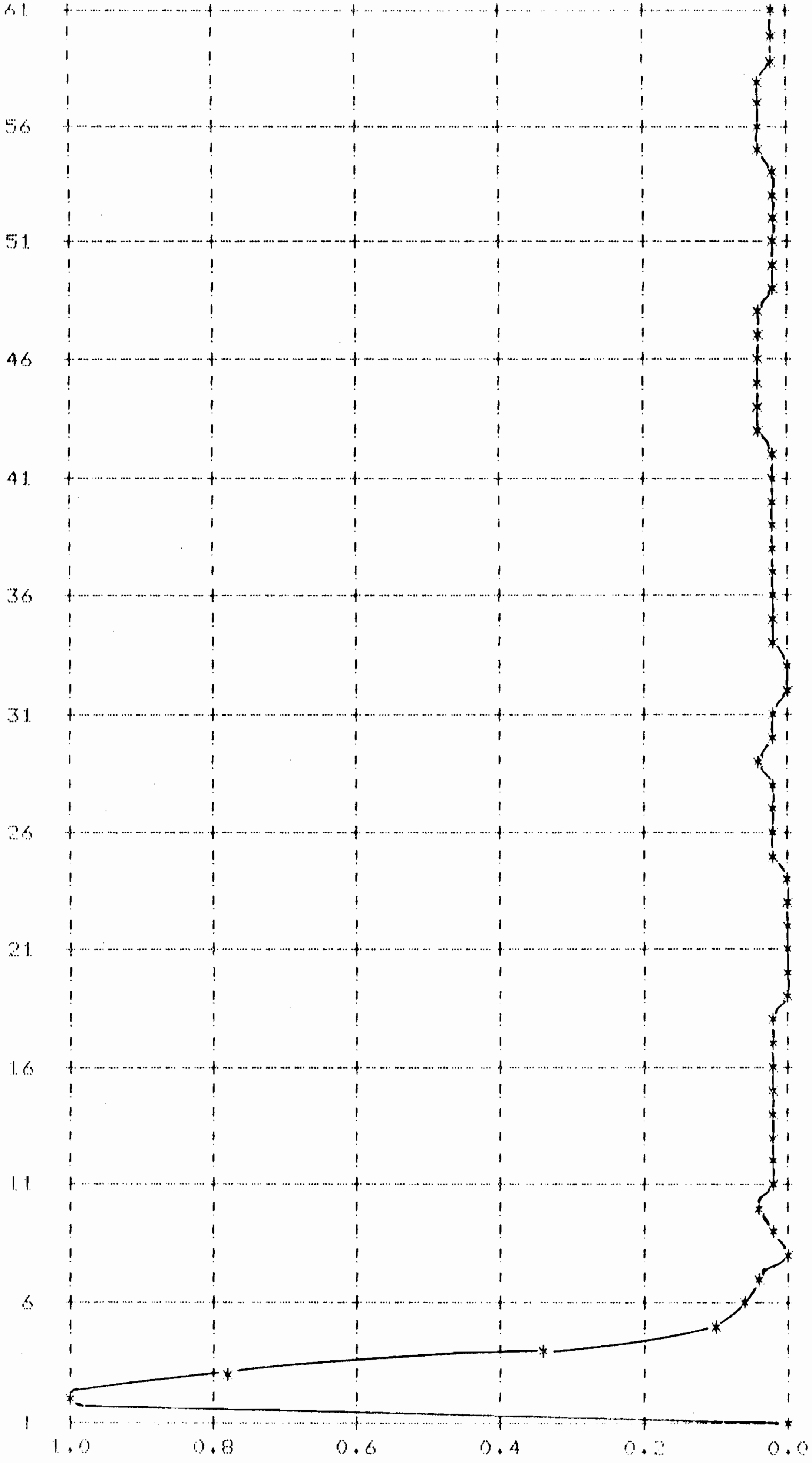

Fig 37a. Fourier transform of the output pulse from the step index fibre.

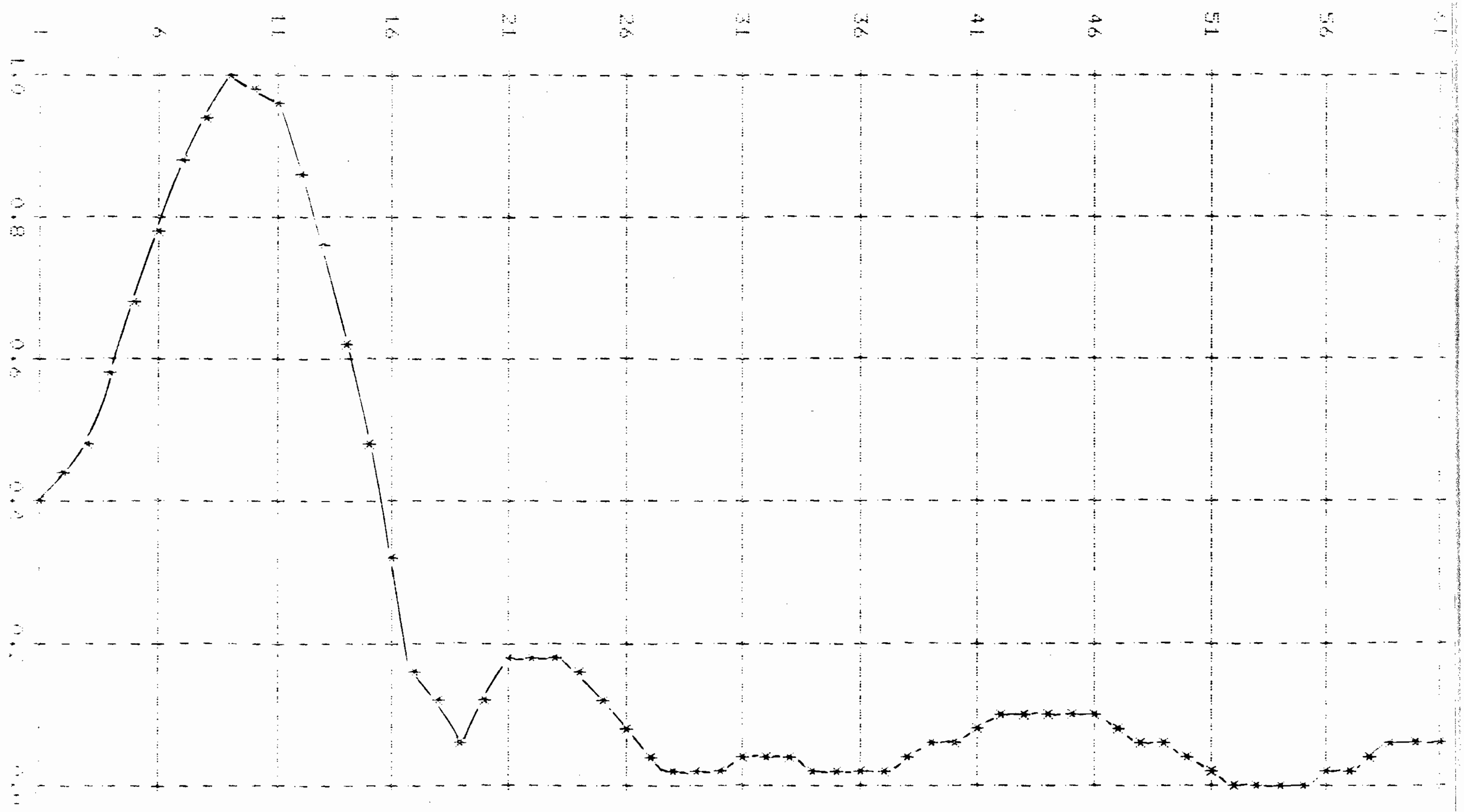

Fic 37h. Impulse response of the step index fibre (T =200 psec).

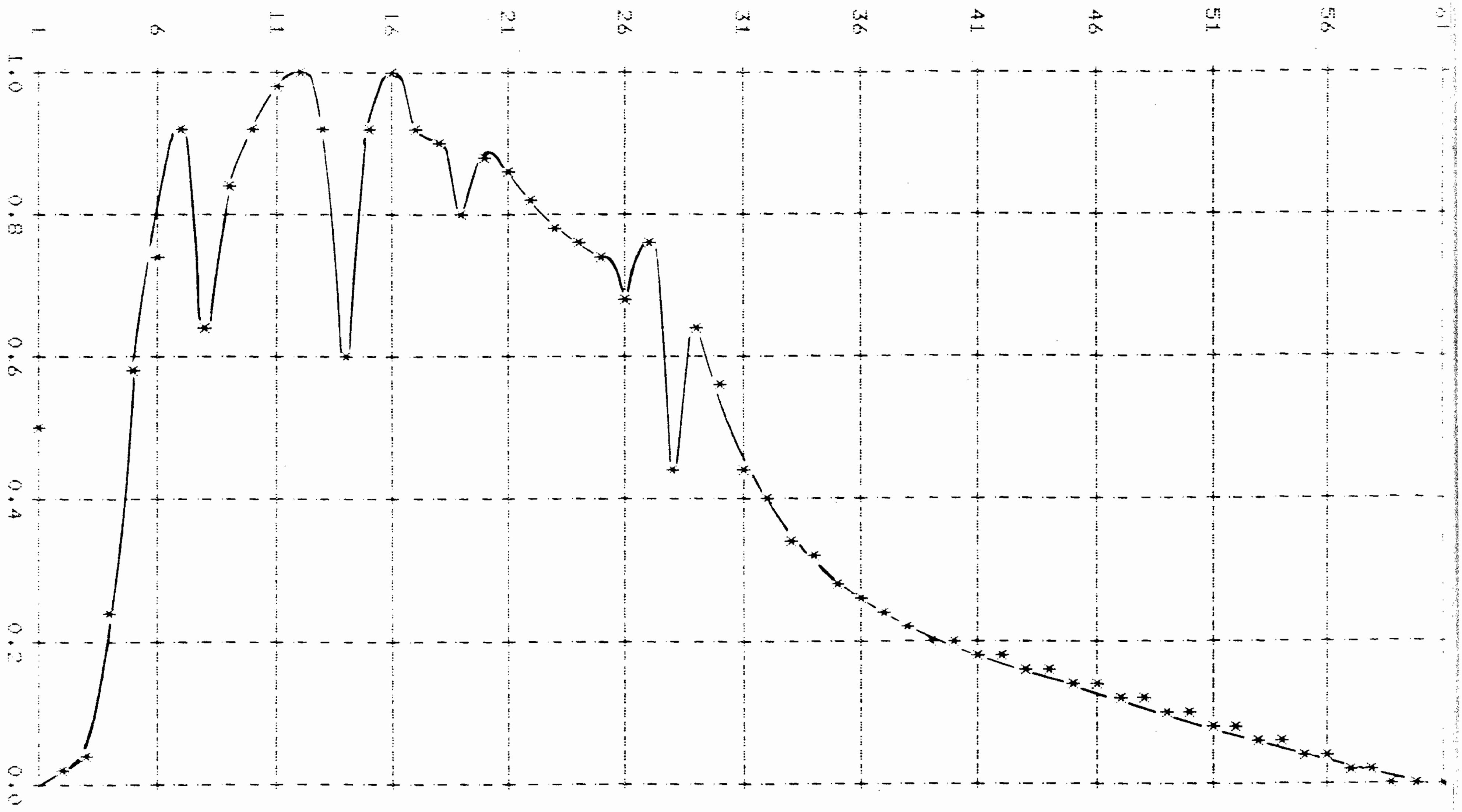

Fig 37i. Output pulse from the graded index fibre (T = 400 psec).

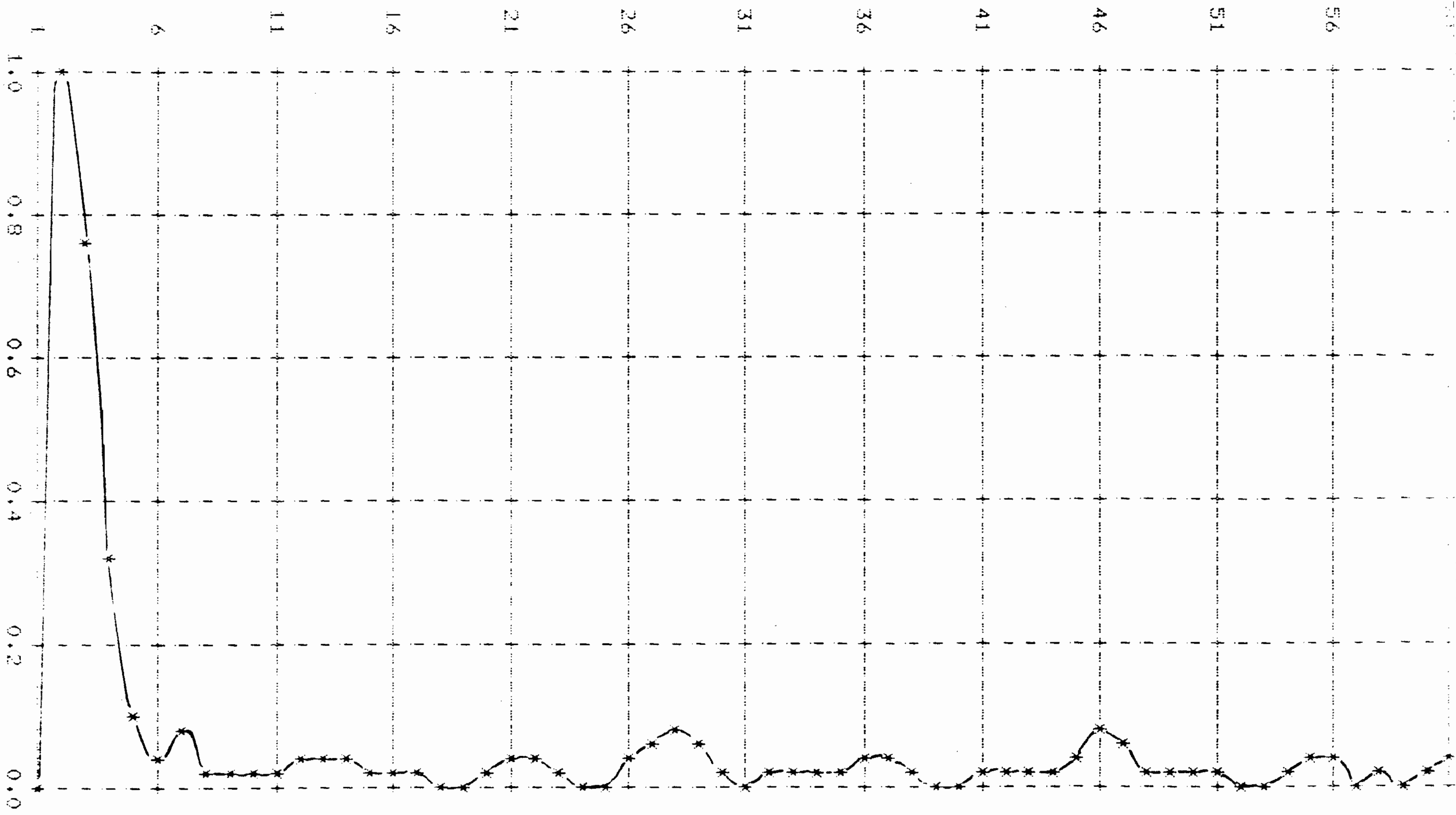

Fig 37j. Fourier transform of the output of the graded index fibre.

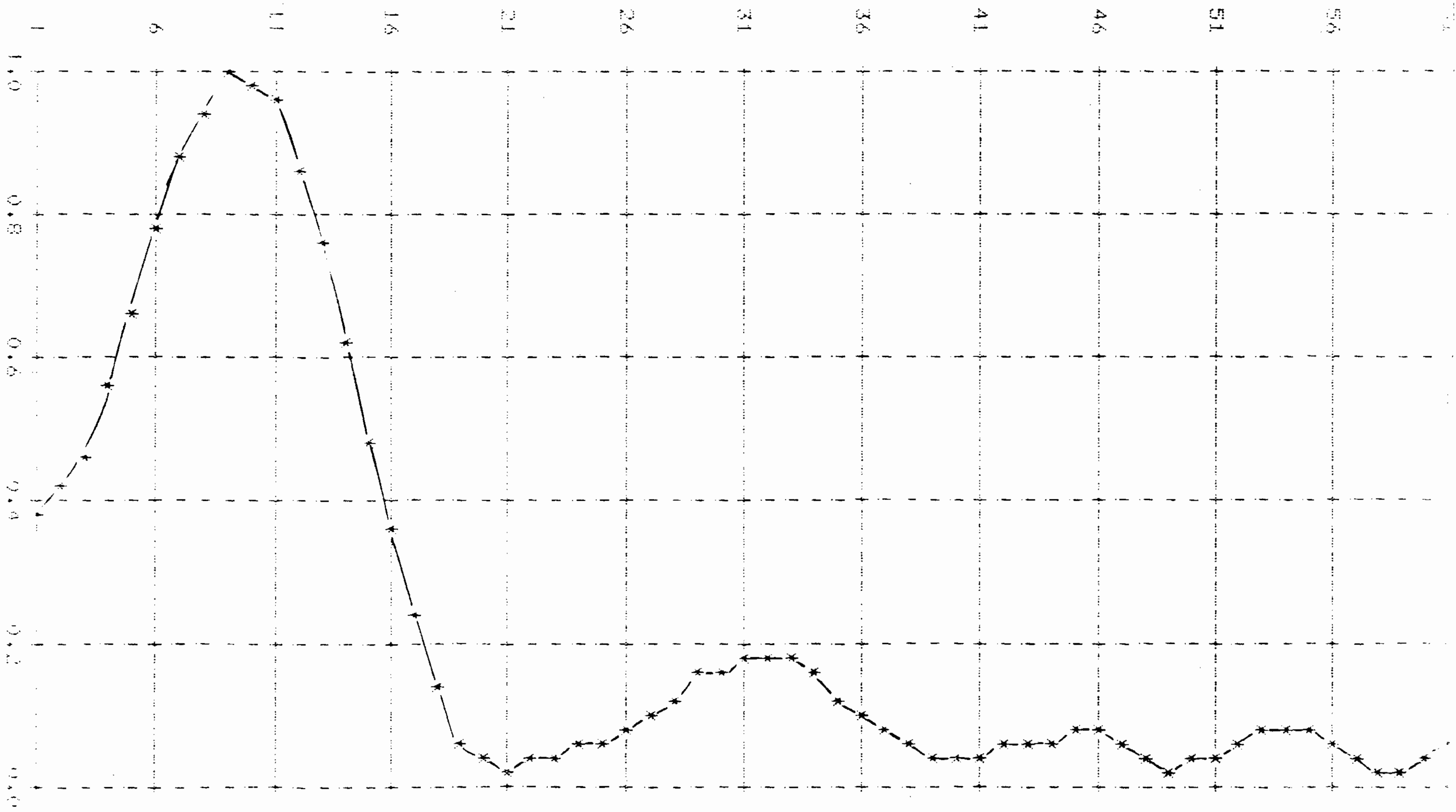

Fig 37k. Impulse response of the graded index fibre (T = 200 psec).

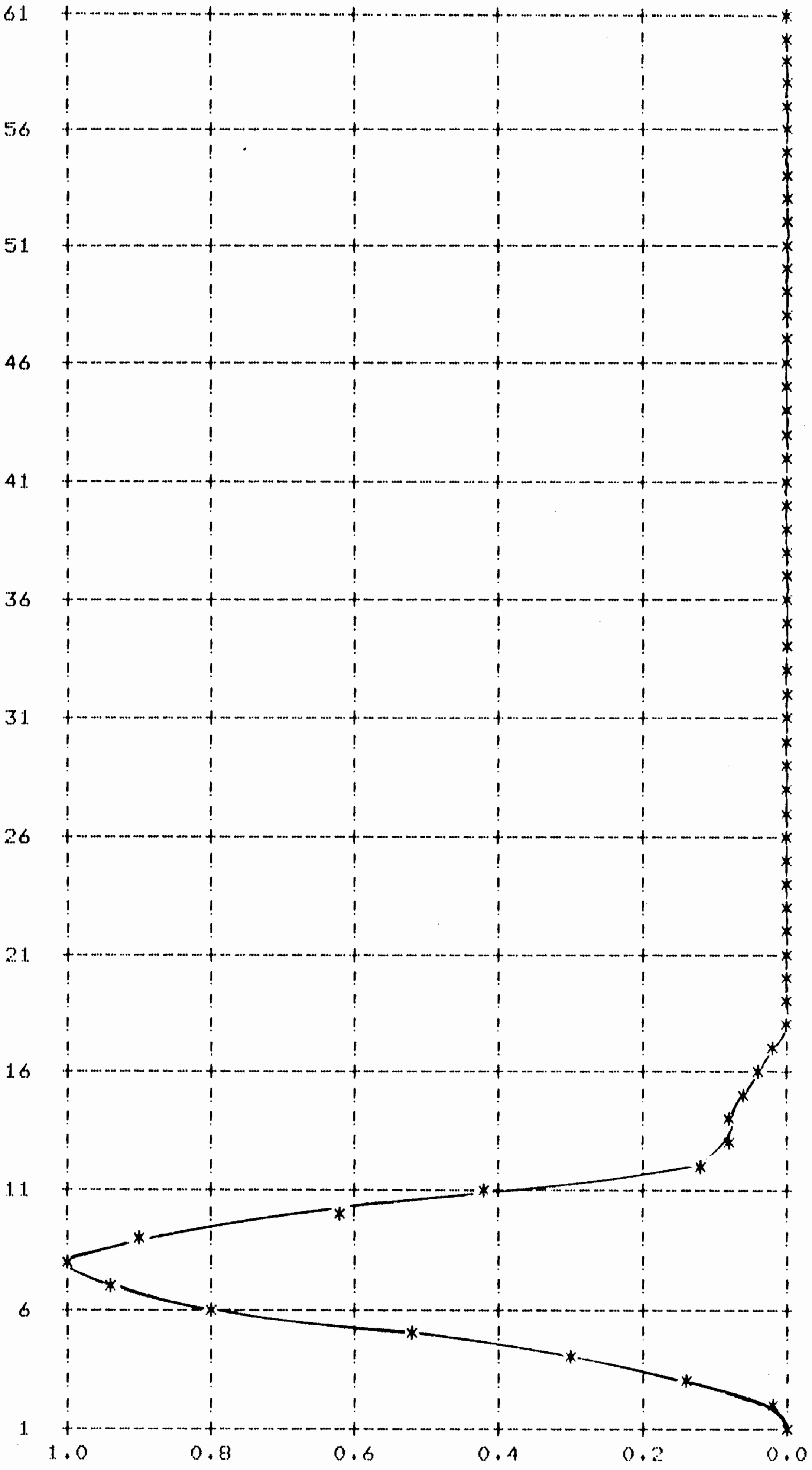

Fig 38a. Input pulse (T = 100 psec). [Ref 40]

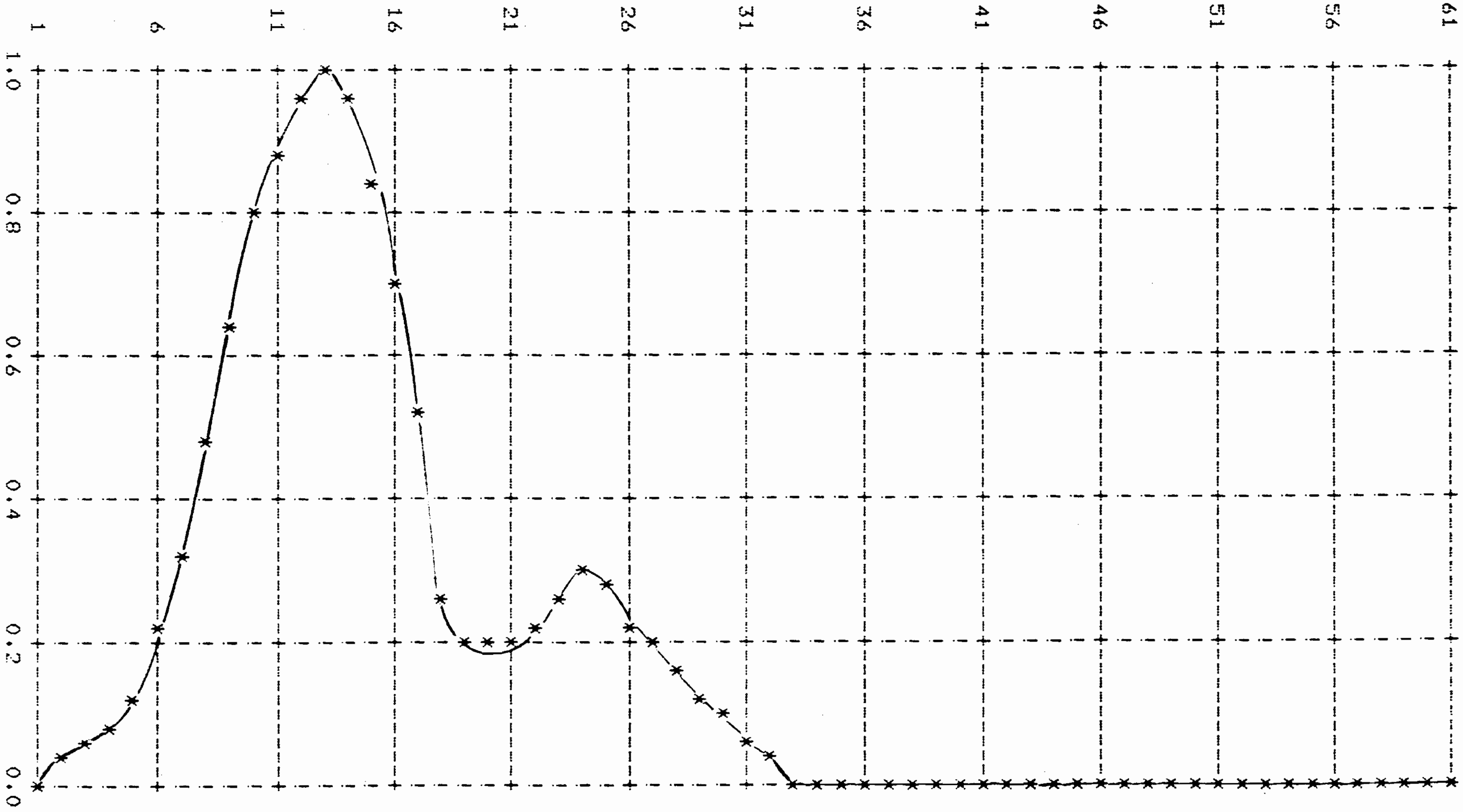

Fig 38b. Output pulse from the graded index fibre (T = 100 psec). [Ref 40]

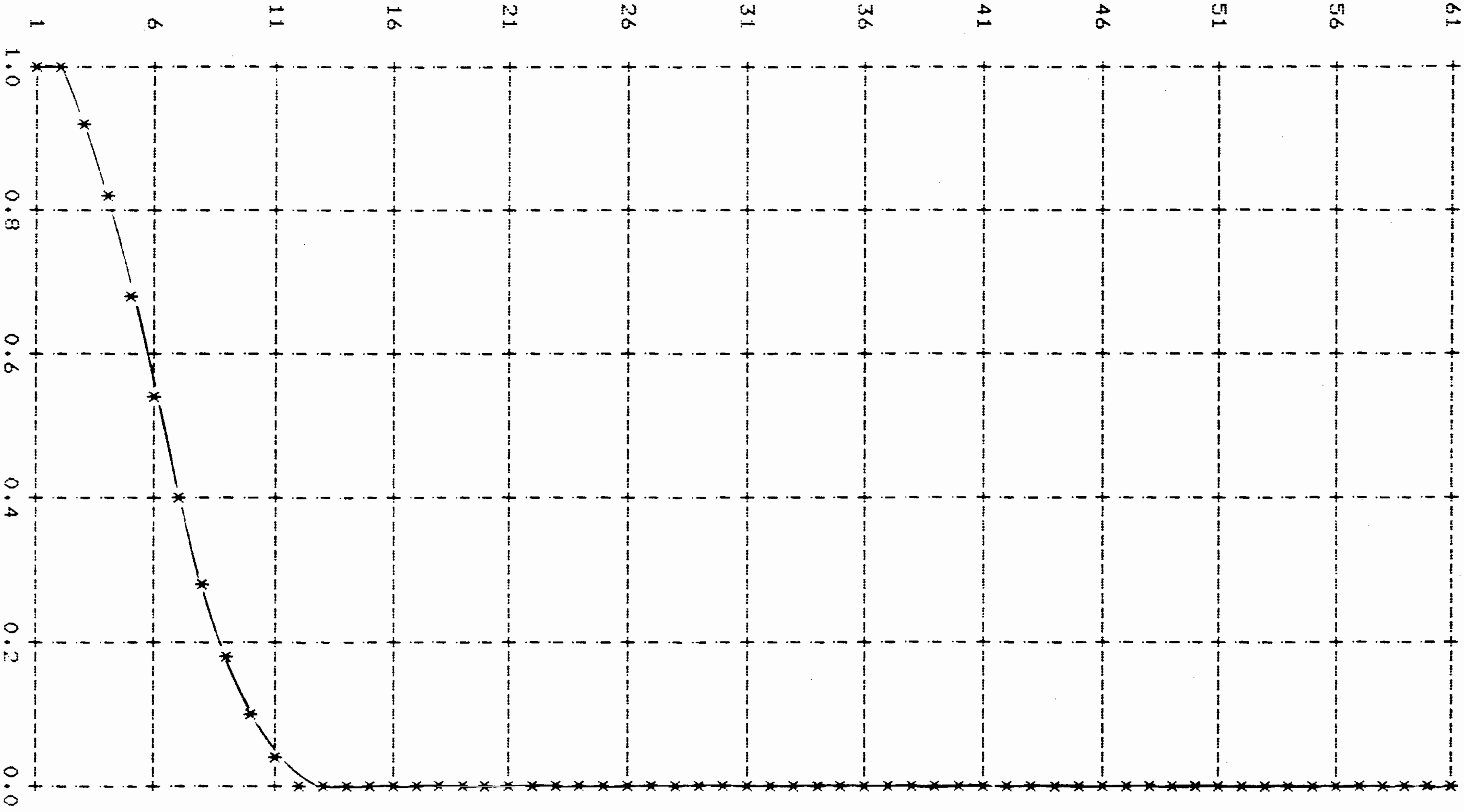

Fig 38c. Fourier transform of the impulse response of the graded index fibre.

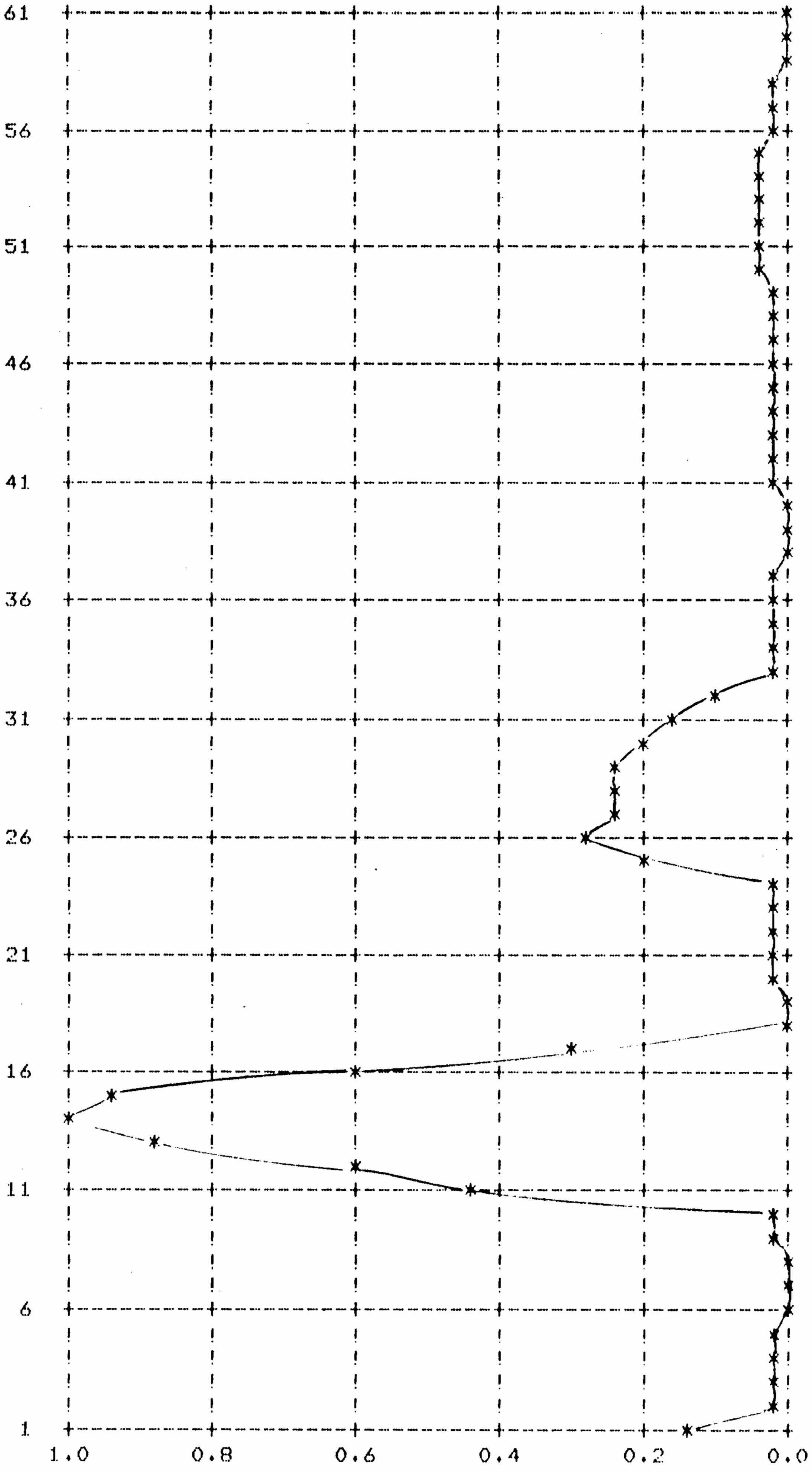

Fig 38d. Impulse response of the graded impulse response (T = 100 psec).

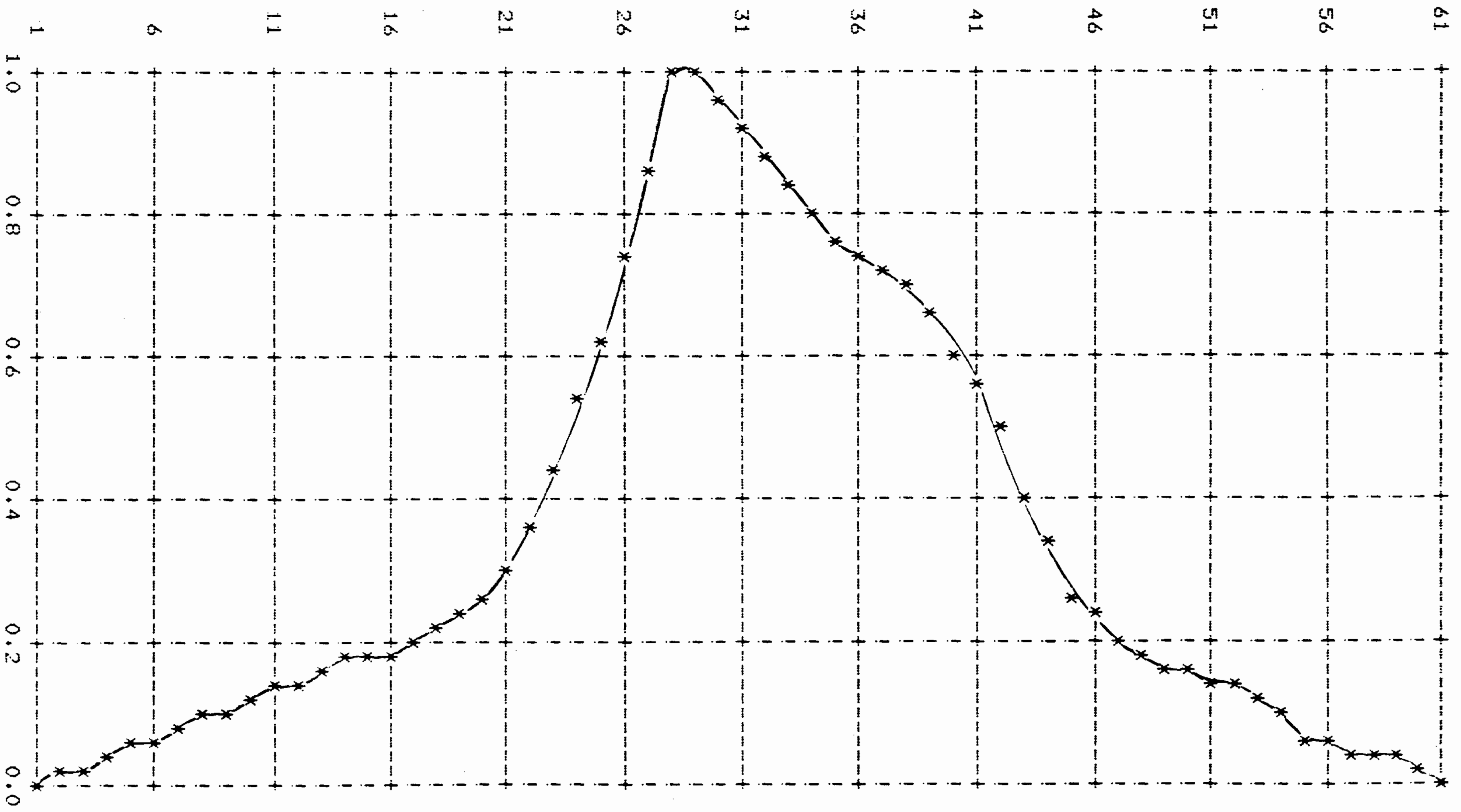

Fig 38e. Output pulse from the step index fibre (T = 100 psec). [Ref 40]

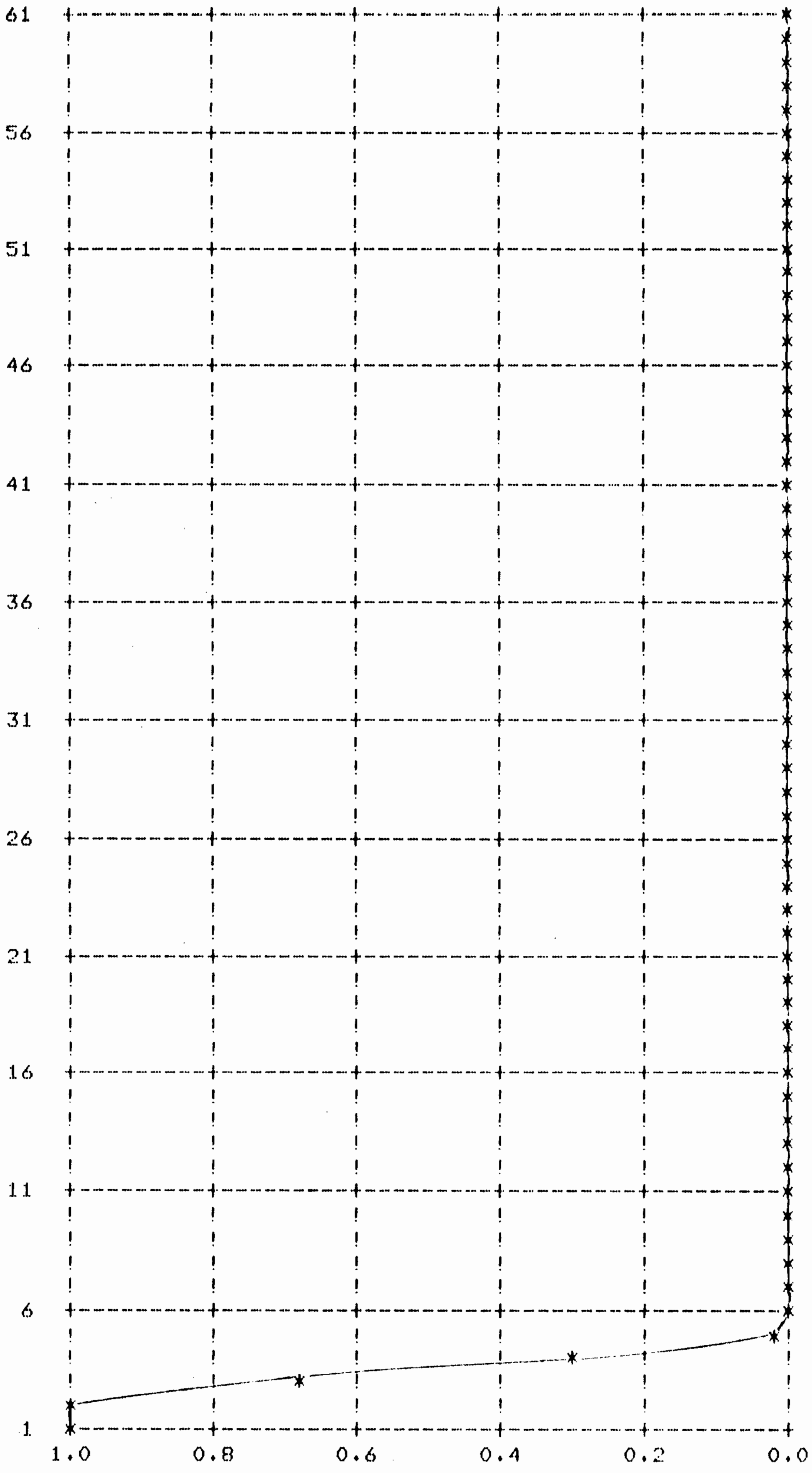

Fig 38f. Fourier transform of the impulse response of the step index fibre.

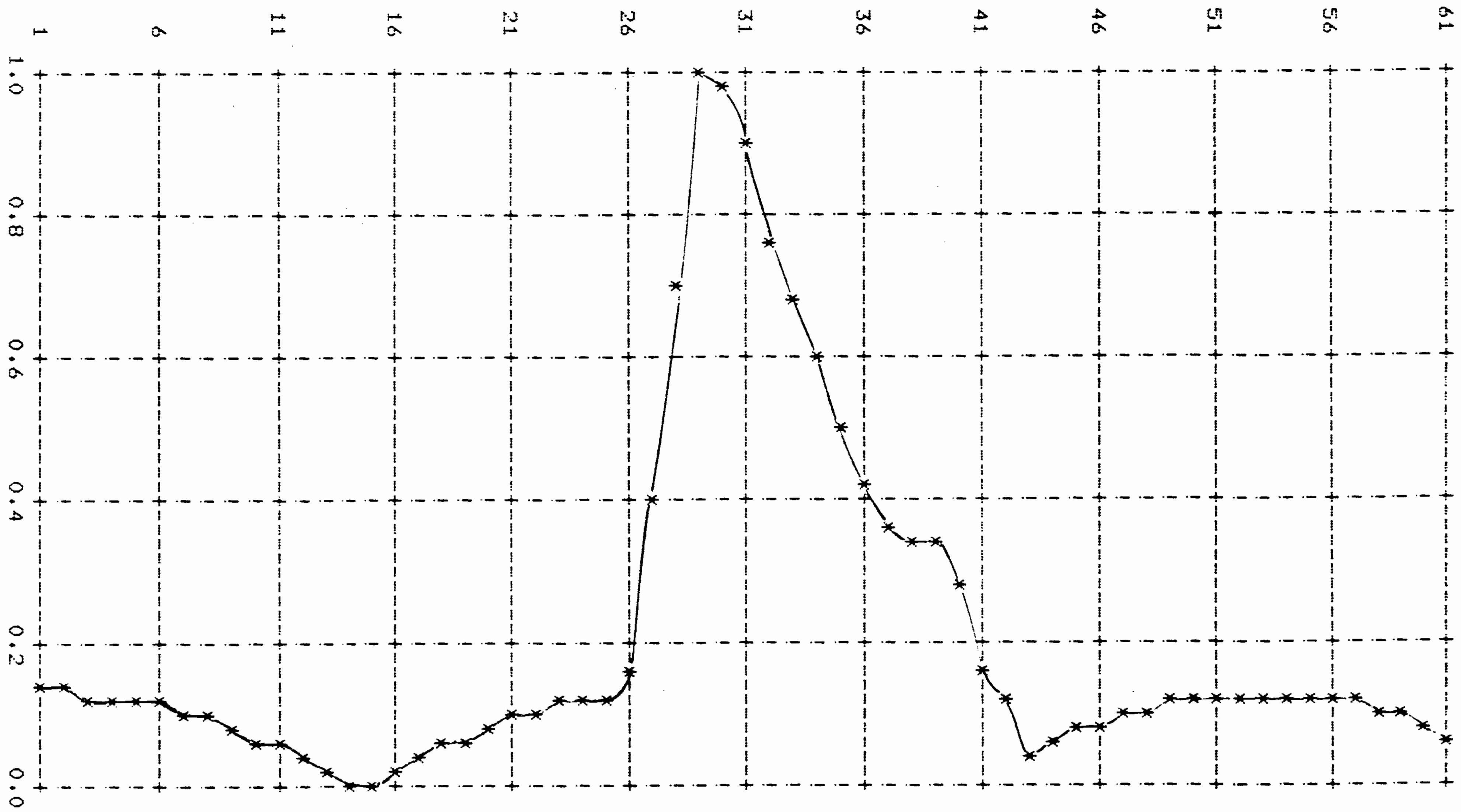

Fig 38a. **Impulse response of the step index fibre (T = 100 psec).**

(iii) Comparision of Experimental Results with Manufacturer's Data

Fig 39 outlines the published, measured and calculated data. In the case of the published data, one must accept these numbers, but one <u>not</u> treat them as the absolute reference with which to judge the following results. The reason for this will become obvious in the ensuing discussion. An interesting point to note is the radical difference between the results obtained by the author and those obtained by Mr. Puc (Ref 40). These large discrepancies occur purely due to the form of the injected light pulse. Although the actual width of the light pulse probably has some effect upon the pulse spreading, the major factor involved is the light launching conditions. It is evident that the more confined the input light is, then fewer modes are excited and hence the light is more axially confined. This will result in less pulse spreading!

The calculated pulse spreading verifies the above statement. For the PCS and step index fibres, Equations 18, 26 and 30 are used to calculate the spreading. For the case of wide beam angle, the pulse broadening is determined by Equation 26. It can be seen that the broadening is totally dependent upon the fibre characteristics. In particular, defining the numerical aperature (NA) of the fibre as:

$$NA = n_2 (2 (n_1 - n_2))^{1/2} \qquad (42)$$

where n_1 is the index of refraction of the core and n_2 is the index of refraction of the cladding ($n_2 \cong n_1$). Hence it can be shown that:

$$\Delta t \cong T_0 \, NA^2 / (2n_1^3) \qquad (43)$$

Description	PCS fibre	Step fibre	Graded fibre
(i) ITT published data			
Numerical Aperature	0.3	0.25	0.25
-3dB pulse spread (nsec/Km)	30	15	2.5
Core index of refraction	1.46	1.48	1.48
Fibre core diameter (microns)	125	50	50
(ii) Measured -3dB pulse spread			
Fig 37a as input (nsec/Km)	59	41	43
Fig 38a as input (nsec/Km)	-	13	9
(iii) Calculated -3dB pulse spread			
NA=.25, beam angle=30° (nsec/Km)	-	44	-
NA=.25, beam angle=9° (nsec/Km)	-	15	-
NA=.25, beam angle=8.4° (nsec/Km)	-	13.1	-
NA=.3, beam angle=30° (nsec/Km)	70	-	-
NA=.28, beam angle=30° (nsec/Km)	61	-	-

Fig. 39 Tabulation of published, measured and calculated results.

This indicates that the pulse broadening is highly dependent upon the relative difference between the indices of refraction of the cladding and the core. This can be seen from the calculated pulse spreading for the PCS fibre: a 7% change in NA produces a 14% change in pulse spread! Similiarly for the launching beam angle (step index fibre); for a 7% change in beam angle, a 15% change in pulse spreading occurs.

To re-iterate, since the ITT publications did not include a description of the test conditions, no meaningful comparisons can be made. The most that one can say at this point is that the published data and both Mr. Puc's and my measurements are of comparable magnitude and hence seem reasonable.

The case of the graded index fibre is difficult to analyze: in order to be accurate, a description of the index profile is mandatory! Since this description was not given by the manufacturer, it is therefore impossible at this time to calculate the pulse spreading using the theory developed in Chapter 4. For those equations, one requires two co-efficients of the power series describing the distribution of the refractive index. However, looking at the measured values, one can see quite strikingly the effect of different launching conditions upon the impulse response. It is obvious that with the input of Fig 37a, a great deal of skew rays are excited which consequently produces excessive pulse broadening. An interesting point to note is that the measurements performed by Mr. Puc show a pulse spread 3.6 times greater than that published by ITT. This is probably due to the excitation of modes which may be attenuated over long distances, but show up here simply because the fibre was too short. Also, excessive mode mixing might have produced this result. This mode mixing would have occurred since the fibre was wound upon a small drum. This constant curvature of the fibre could also have produced the excessive pulse spreading.

8- Conclusions and Recommendations

It is hoped that this report has satisfactorily shown that a complete and carefully defined set of test conditions are mandatory when presenting a description of the pulse broadening in an optical glass fibre. This description is vital,considering the wide range of uses that these fibres will have. A user who is not aware of the restrictions upon launch conditions can be sorely disappointed when the fibre he is using does not perform as specified by the manufacturer. This description of the launch conditions must include information concerning the input light beam's shape (ie. beam angle and pulse width) and also must consider the orientation of the fibre end. For example, if a fibre end is not flat and perpendicular to the longitudinal axis, then excessive skew rays can be produced in the graded index fibre. These will, of course, produce the greatest pulse broadening and hence will limit the information rate.

It is also concluded that either narrower light pulses or longer fibres should be used in ensuing experiments. For a fixed pulse broadening, it is obvious that shorter light pulses will produce the greatest effect and consequently will yield more accurate descriptions of the impulse response.

It is evident that the ray optics theory produces reasonably accurate descriptions of the impulse response of optical glass fibres. In order to use this theory effectively, however, one requires an accurate description of refractive index profiles. This description can be obtained through various index profile measurement schemes, however, one must keep in mind that manufacturing techniques of optical glass fibres cannot produce absolutely uniform index profiles. Hence, at best one can obtain only an average profile. It must be kept in mind that this variation in profile can have a very marked effect upon the impulse response.

It is recommended that any future attempts to measure the impulse response of optical glass fibres take the following course. One should establish an experimental set-up to measure refractive index profiles. The pulse spreading of the desired fibre can consequently be quite easily measured upon the test bench designed by Mr. Puc. Subsequent tests should include the effect of varying beam angle and launch.

It is also recommended that narrower input light pulses be utilized. This can be accomplished using an SH laser where the applied current for lasing is set upon a pedestal current pulse. This pedestal current will have an amplitude equal to the laser threshold current and a width of between 20 to 50 nsec. The actual lasing current will be superimposed upon this pedestal and will be delayed by about 10 to 15 nsec and will be narrow enough to produce the desired light pulse width. This scheme will then result in light pulses which are sufficiently narrow for impulse response measurement and yet will have enough intensity to overcome the fibre and coupling losses.

Appendix

(i) Proof of Formula for Impulse Response Calculation for Truncated Sampled Signals.

For truncated signals of the form:

$$\hat{h}(t) = \sum_{n=0}^{N-1} h(nT)\,\delta(t - nT) \qquad (A\text{-}1)$$

and for systems with input/output signals r(t), c(t) respectively and system responses f(t) of the form:

$$c(t) = r(t) * f(t) \qquad (A\text{-}2)$$

where '$*$' represents a convolution; one can define the sampled signals in terms of their Fourier transform inverse as follows:

$$h(k) = (1/N) \sum_{n=0}^{N-1} H(n)\exp(j2\pi nk/N) \qquad (A\text{-}3)$$

The discrete convolution is defined as (Ref 41):

$$c(k) = \sum_{i=0}^{N-1} r(i)\ f(k-i) \quad , \qquad (A\text{-}4)$$

now substituting Equation A-3 into Equation A-4 yields:

$$\frac{1}{N} \sum_{n=0}^{N-1} C(n)\exp(j2\pi nk/N) = \sum_{i=0}^{N-1} \frac{1}{N} \sum_{m=0}^{N-1} R(m)\exp(j2\pi mi/N)$$

$$\times \frac{1}{N} \sum_{n=0}^{N-1} F(n)\ \exp(j2\pi n(k-i)/N) \qquad (A\text{-}5)$$

or,

$$\frac{1}{N}\sum_{n=0}^{N-1} C(n)\exp(j2\pi nk/N) = \frac{1}{N}\sum_{m=0}^{N-1} R(m) \sum_{n=0}^{N-1} F(n)\exp(j2\pi nk/N)$$

$$\times \frac{1}{N}\sum_{i=0}^{N-1} \exp(j2\pi mi/N)\exp(-j2\pi ni/N) \tag{A-6}$$

where the last summation defines the orthogonality relationship if <u>m=n</u> and is zero otherwise, hence:

$$\sum_{n=0}^{N-1} C(n)\exp(j2\pi nk/N) = \sum_{n=0}^{N-1} R(n)\ F(n)\ \exp(j2\pi nk/N) \tag{A-7}$$

therefore:

$$C(n) = R(n)\ F(n) \tag{A-8}$$

or F(n) =fibre impulse response

$$= C(n)\ /\ R(n) \tag{A-9}$$

QED.

(ii) Fortran Program

```
C
C MAIN.FT
C
C THIS PROGRAM SOLVES FOR THE IMPULSE RESPONSE
C OF OPTICAL GLASS FIBRE.
C
          REAL REA(256),IMA(256),REST(256),IMST(256)
          REAL ARRAY(256),ST(256),NF(4)
          DEFINE FILE 1 (4,61,U,IPNT)
C
          WRITE(4,1000)
    1000  FORMAT('ENTER FILTER CUTOFF (4I3)')
          READ(4,1001)(NF(I),I=1,4)
    1001  FORMAT(4I3)
          DO 1 I=1,4
          IPNT=I
          DO 2 J=1,256
          ARRAY(J)=0.0
          REA(J)=0.0
    2     IMA(J)=0.0
C
          READ(1'IPNT)(REA(K),K=1,61)
          DO 8 M=195,256
    8     REA(M)=-REA(257-M)
          CALL GRAPH(REA)
          CALL FFT(REA,IMA)
C
          IF(I.NE.1)GO TO 100
          DO 4 J=1,256
          REST(J)=REA(J)
    4     IMST(J)=IMA(J)
C
    100   IF(I.EQ.1)GO TO 1
C
          DO 5 J=2,NF(I)
          DENOM=REST(J)**2+IMST(J)**2
          T1=REA(J)*REST(J)+IMA(J)*IMST(J)
          T2=IMA(J)*REST(J)-REA(J)*IMST(J)
          REA(J)=T1/DENOM
          IMA(J)=T2/DENOM
C
          REA(257-J)=REA(J)
          IMA(257-J)=-IMA(J)
          ARRAY(J)=SQRT(REA(J)**2+IMA(J)**2)
    5     CONTINUE
          REA(1)=REA(2)
          REA(256)=REA(2)
          IMA(1)=IMA(2)
          IMA(256)=-IMA(2)
          ARRAY(1)=ARRAY(2)
          CALL GRAPH(ARRAY)
          CALL FFT(REA,IMA)
C
          DO 6 J=1,64
          IF(REA(J).GT.0.0)REA(J)=0.0
```

```
0054         IF(REA(J).GT.0.0)IMA(J)=0.0
00556        REA(J)=SQRT(REA(J)**2+IMA(J)**2)
0056         CALL GRAPH(REA)
00571        CONTINUE
0060         CALL EXIT
0061         END
```

```
      SUBROUTINE GRAPH(ARRAY)
C
C
C GRAPH.FT
C
C THIS ROUTINE OUTPUTS A GRAPH OF THE POINTS CONTAINED
C WITHIN THE ARRAY.
C
      DIMENSION ARRAY(256)
      REAL MAX
      INTEGER PLOT(51),HORZ,VERT,PLUS,SPACE,POS,POINT
      DATA HORZ/'-'/,VERT/'!'/,PLUS/'+'/,SPACE/' '/,POS/'*'/
C
      MAX=ARRAY(1)
      DO 1 I=1,61
      IF(MAX.LT.ARRAY(I))MAX=ARRAY(I)
      IF(ARRAY(I).LT.0.0)ARRAY(I)=0.0
1     CONTINUE
C
      DO 3 I=1,61
      DO 2 I1=1,51
      II1=I1-1
      PLOT(I1)=SPACE
      IF(MOD(II1,10).EQ.0)PLOT(I1)=VERT
2     CONTINUE
C
      II=I-1
      POINT=IFIX(51.5-50.0*ARRAY(62-I)/MAX)
      IF(MOD(II,5).NE.0)GO TO 100
       DO 4 J=1,51
       PLOT(J)=HORZ
       JJ=J-1
       IF(MOD(JJ,10).EQ.0)PLOT(J)=PLUS
4     CONTINUE
C
      PLOT(POINT)=POS
      IM=62-I
      WRITE(6,1000)IM,PLOT
1000  FORMAT(10X,I2,2X,51A1)
      GO TO 101
100   PLOT(POINT)=POS
      WRITE(6,1001)PLOT
1001  FORMAT(14X,51A1)
101   CONTINUE
3     CONTINUE
      WRITE(6,1002)
1002  FORMAT(13X,'1.0',7X,'0.8',7X,'0.6',7X,'0.4',
     *7X,'0.2',7X,'0.0')
      WRITE(6,1003)
1003  FORMAT('1')
      RETURN
      END
```

```
C
C FFT2.FT
C
C SUBROUTINE TO CALCULATE FAST FOURIER TRANSFORM
C OF THE INPUT ARRAYS: XREAL AND XIMAG.
C
0002          SUBROUTINE FFT(XREAL,XIMAG)
0003          DIMENSION XREAL(256),XIMAG(256)
0004          N=256
0005          N2=N/2
0006          NU1=7
0007          NU=8
0010          K=0
C
0011          DO 100 L=1,NU
0012102       DO 101 I=1,N2
0013          P=FLOAT(IBITR(K/2**NU1,NU))
0014          ARG=6.283185*P/256.0
0015          C=COS(ARG)
0016          S=SIN(ARG)
0017          K1=K+1
0020          K1N2=K1+N2
0021          TREAL=XREAL(K1N2)*C+XIMAG(K1N2)*S
0022          TIMAG=XIMAG(K1N2)*C-XREAL(K1N2)*S
0023          XREAL(K1N2)=XREAL(K1)-TREAL
0024          XIMAG(K1N2)=XIMAG(K1)-TIMAG
0025          XREAL(K1)=XREAL(K1)+TREAL
0026          XIMAG(K1)=XIMAG(K1)+TIMAG
0027101       K=K+1
0030          K=K+N2
0031          IF(K.LT.N)GO TO 102
0032          K=0
0033          NU1=NU1-1
0034100       N2=N2/2
0035          DO 103 K=1,N
0036          I=IBITR(K-1,NU)+1
0037          IF(I.LE.K) GO TO 103
0040          TREAL=XREAL(K)
0041          TIMAG=XIMAG(K)
0042          XREAL(K)=XREAL(I)
0043          XIMAG(K)=XIMAG(I)
0044          XREAL(I)=TREAL
0045          XIMAG(I)=TIMAG
0046103       CONTINUE
0047          RETURN
0050          END
C
        FORTRAN IV   4AAAA     9-JAN-79                    PAGE   ONE

0002          FUNCTION IBITR(J,NU)
0003          J1=J
0004          IBITR=0
0005          DO 200 I=1,NU
0006          J2=J1/2
0007          IBITR=IBITR*2+(J1-2*J2)
0010200       J1=J2
0011          RETURN
0012          END
```

PLASTIC CLAD
SILICA FIBERS

TYPES PS-05-35, PS-05-20
PS-05-10

Plastic Clad Silica Fiber, Type PS-05, is designed for use in economical, medium bandwidth, medium distance single fiber data transmission systems. The fiber consists of a homogeneous pure silica core surrounded by a plastic optical cladding and a plastic protective coating. The plastic cladding and coating provide the fiber with mechanical and environmental protection. This fiber may be used singly or incorporated into multichannel fiber optic cables.

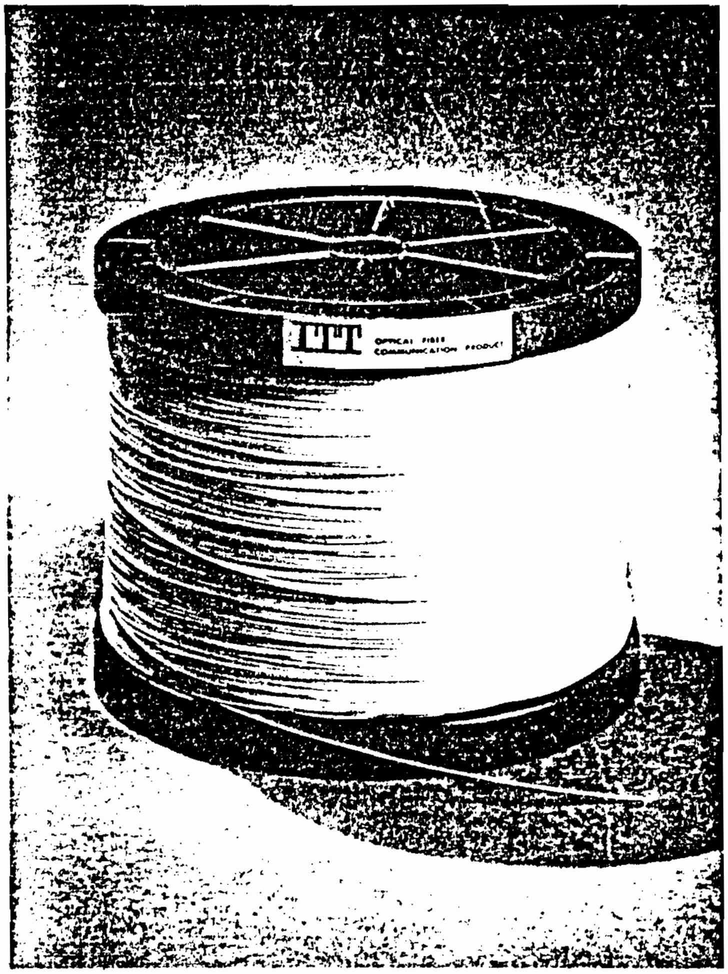

SPECIFICATIONS	NOMINAL
Attenuation @ .79μm	
PS-05-35	35 dB/km
PS-05-20	20 dB/km
PS-05-10	10 dB/km
Numerical Aperture	.3
Dispersion	
10 dB width	60 ns/km
3 dB width	30 ns/km
Core Index of Refraction	1.46
Fiber Core Diameter	125 μm
Jacket Outer Diameter	500 μm
Tensile Strength (½ m gauge length)	500,000 psi
Minimum Bending Radius	0.5 cm

This specification is for a developmental product, subject to change without notice.

ITT

TYPES GS-02-12, GS-02-8, GS-02-5

Glass Step Index Fiber, Type GS-02, is designed for use in medium to high bandwidth single fiber data transmission systems. The fiber consists of a doped silica core and a borosilicate cladding with a step index profile. A plastic jacket is extruded onto the fiber to provide mechanical and environmental protection. This fiber is suitable for incorporation into a multi-channel cable or may be used singly.

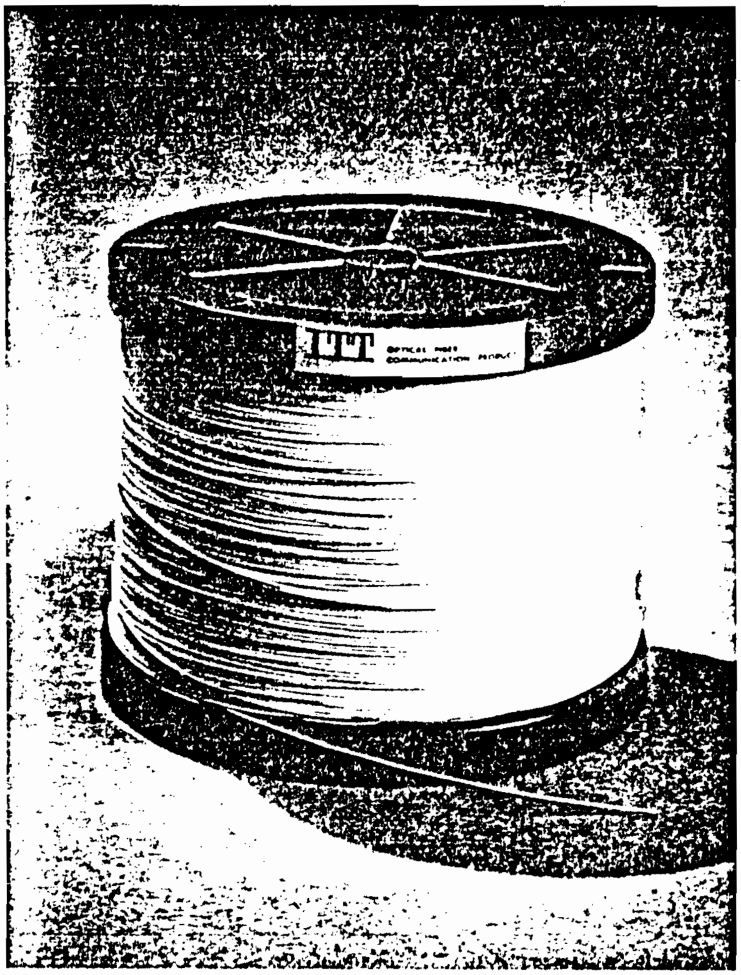

[illegible]	NOMINAL
Attenuation	
GS-02-12	
@ 0.85μm	12 dB/km
@ 1.06μm	8 dB/km
GS-02-8	
@ 0.85μm	8 dB/km
@ 1.06μm	5 dB/km
GS-02-5	
@ 0.85μm	5 dB/km
@ 1.06μm	3 dB/km
Numerical Aperture	.25
Dispersion	
10 dB width	30 ns/km
3 dB width	15 ns/km
Core Index of Refraction	1.48
Fiber Core Diameter	50 μm
Fiber Outer Diameter	125 μm
Jacket Outer Diameter	500 μm
Tensile Strength (½m gauge length)	500.000 psi
Minimum Bending Radius	0.5 cm

This specification is for a developmental product, subject to change without notice.

TYPES GG-02-12, GG-02-8, GG-02-5

Glass Graded Index Fiber, Type GG-02, is designed for use in high bandwidth single fiber data transmission systems. The fiber consists of a doped silica core with a graded index of refraction profile and a borosilicate cladding. The graded index profile significantly reduces dispersion thus permitting larger bandwidth signals to be transmitted. A plastic jacket is applied to the fiber to provide mechanical and environmental protection. The fiber may be used singly or incorporated into multichannel fiber optic cables.

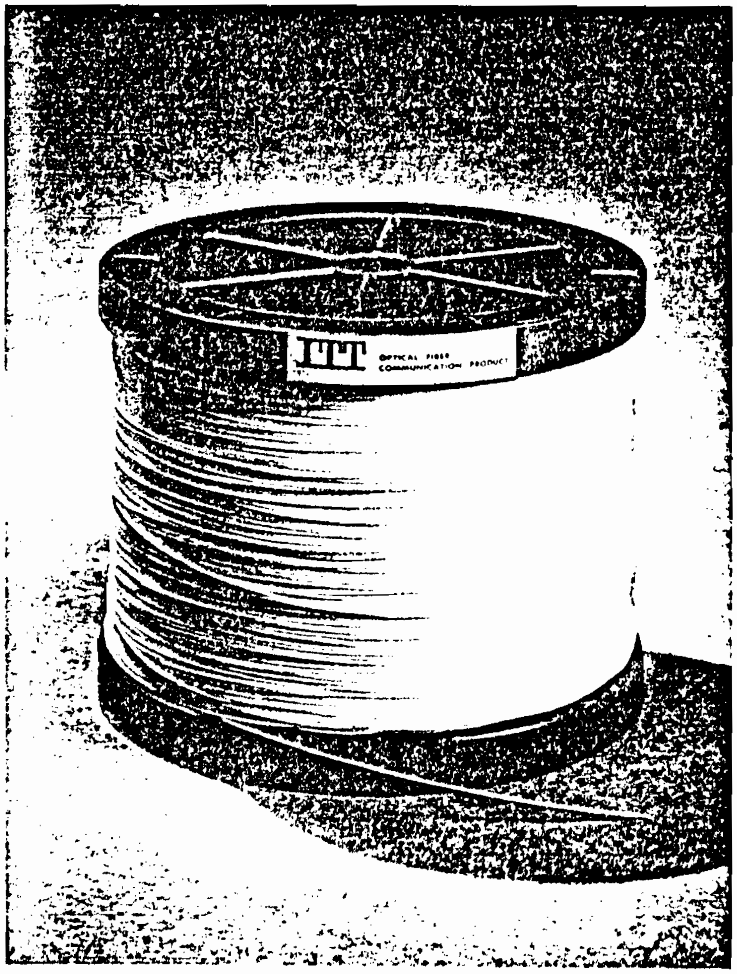

SPECIFICATION	NOMINAL
Attenuation	
GG-02-12	
@ 0.85μm	12 dB/km
@ 1.06μm	8 dB/km
GG-02-8	
@ 0.85μm	8 dB/km
@ 1.06μm	5 dB/km
GG-02-5	
@ 0.85μm	5 dB/km
@ 1.06μm	3 dB/km
Numerical Aperture	.25
Dispersion	
10 dB width	5.0 ns/km
3 dB width	2.5 ns/km
Core Index of Refraction (on axis)	1.48
Fiber Core Diameter	50 μm
Fiber Outer Diameter	125 μm
Jacket Outer Diameter	500 μm
Tensile Strength (½m gauge length)	500,000 psi
Minimum Bending Radius	0.5 cm

This specification is for a developmental product, subject to change without notice.

ITT

BIBLIOGRAPHY

(1) Taub & Schilling, "Principles of Communication Systems," McGraw-Hill, 1971.

(2) Lucky, Salz & Weldon, "Principles of Data Communication," McGraw-Hill, 1968.

(3) Steele, "Optical Lasers in Electronics." Wiley, 1968.

(4) Moss, Burrell & Ellis, "Semiconductor Opto-Electronics." Wiley, 1973

(5) Arecchi & Schulz-Dubois, "Laser Handbook," Vol 1.
NORTH-HOLLAND PUBLISHING COMPANY - 1972.

(6) Panish, "Heterostructure Injection Lasers," Proc. IEEE, Vol 64, No 10, Oct 1976.

(7) Chown et al, "Direct Modulation of Double Heterostructure Lasers at Rates up to 1 Gbit/sec," Electron. Lett, Vol 9, Jan 1973.

(8) Danielsen, "A Theoritical Analysis for Gigabit/Second Pulse Code Modulation of Semiconductor Lasers," IEEE J Quan Elect, Vol QE-12, No 11, Nov 1976.

(9) Gooch, "Injection Electroluminescent Devices." Wiley, 1973.

(10) McIntyre et al, "Properties of Avalanche Photodiodes," RCA Review, Vol 35, June 1974.

(11) Personick, "Receiver Design for Digital Fiber Optic Communication Systems, I & II," BSTJ Vol 52, No 6, Jul/Aug 1973.

(12) Melchoir et al, "Photodetectors for Optical Communication Systems," Proc. IEEE, Vol 58, No 10, Oct 1970.

(13) Millman & Halkias, "Integrated Electronics," McGraw-Hill, 1972.

(14) Lee & Derosier, "Charge Storage in Injection Lasers and Its Effect on High-Speed Pulse Modulation of Laser Diodes," Proc. IEEE, Aug 1974.

(15) Danielsen et al, "Dynamic Behaviour of Semiconductor Lasers," Elect. Lett., Vol 11, No 10, May 1975.

(16) Bouillie, Steiner & Tréheux, "On the Pulse Broadening in Dielectric Multimode Waveguides," Opto- Electronics, Vol 5, 1973.

(17) Bouillie, Cozannet, Steiner & Tréheux, "Ray Delay in Gradient Waveguides with Arbitrary Symmetric Refractive Profiles,"
Applied Optics, Vol 13 No 5, May 1974.

(18) Steiner, "Multimode Waveguides,"
NTZ, Vol 10, 1973.

(19) Puc, "Pulse Broadening in Multimode Optical Fibres and Ray Optics Analysis,"
Seminar Report, May 1978.

(20) Gloge et al, "Optical Fibre End Preparation for Low Loss Splices,"
BSTJ, Vol 52, No 9, Nov 1973.

(21) Cohen & Personick, "Length Dependence of Pulse Dispersion in a Long Multimode Optical Fibres,"
Applied Optics, Vol 14, No 6, June 1975.

(22) Henderson, "Dispersion and Equalization in Fibre Optic Communicatio Systems,"
BSTJ, Vol 52, No 10, Dec 1973.

(23) Personick, "Baseband Linearity and Equalization in Fibre Optic Digital Communication Systems,"
BSTJ, Vol 52, No 7, Sept 1973.

(24) Cook, Mammel & Grow, "Effect of Misalignment on Coupling Efficiency of Single-Mode Optical Fibre Butt Joints,"
BSTJ, Vol 52, No 8, Oct 1973.

(25) Gloge, "Impulse Response of Clad Optical Multimode Fibres,"
BSTJ, Vol 52, No 6, Jul/Aug 1973.

(26) Midwinter, "Pulse Propagation in Multimode Fibres,"
Opt. & Quan. Elect., Vol 8, 1976.

(27) Arnaud, "Pulse Broadening in Multimode Optical Fibres,"
BSTJ, Vol 54, No 7, Sept 1975.

(28) Sammut, "Pulse Dispersion in Partially-Excited Graded-Index Fibres"
Opt. & Quan. Elect., Vol 9, 1977.

(29) Gloge & Marcatili, "Impulse Response of Fibres With Ring-Shaped Parabolic Index Distribution,"
BSTJ, Vol 52, No 7, Sept 1973.

(30) Marcuse, "The Impulse Response of an Optical Fibre With Parabolic Index Profile,"
BSTJ, Vol 52, No 7, Sept 1973.

(31) Marcuse, "Losses and Impulse Response of a Parabolic Index Fibre With Random Bends,"
BSTJ, Vol 52, No 8, Oct 1973.

(32) Gloge & Marcatili, "Multimode Theory of Graded-Core Fibres," BSTJ, Vol 52, No 9, 1973.

(33) Dawson, "Pulse Widening in a Multimode Optical Fibre Excited by a Pulsed GaAs LED," Applied Optics, Vol 13, No 2, Feb 1974.

(34) Kapron & Keck, "Pulse Transmission Through a Dielectric Optical Waveguide," Applied Optics, Vol 10, No 7, July 1971.

(35) Bouillie & Andrews, "Measurements of Broadening of Pulses in Glass Fibres," Elect. Lett., Vol 8, No 12, June 1972.

(36) Gambling et al, " Propagation Model for a Multimode Optical Fibre Waveguide," Elect. Lett., 1972.

(37) Gambling, Payne & Sunak, "Pulse Dispersion in Glass Fibres," Elect. Lett., 1971.

(38) Rabiner & Gold, "Theory and Application of Digital Signal Processing Prentice-Hall, 1975.

(39) Andrews, "Inexpensive Laser Diode Pulse Generator for Optical Waveguide Studies," Rev. Sci. Instrum., Vol 45, No 1, Jan 1974.

(40) Puc, "Pulse Broadening Measurements," Report to Dr. G. L. Yip, McGill University, Dec 1978.

(41) Brigham, "The Fast Fourier Transform," Prentice-Hall, 1974. Appendix.